No matter how hard or impossible it is,
never lose sight of your goal.

Monkey D. Luffy

CONTENTS

LIST OF FIGURES

INTRODUCTION

In the past twenty years, experiments with solar, atmospheric, accelerator and reactor neutrinos have established a consistent paradigm consisting of three neutrino flavours resulting from the mixing of three mass eigenstates. However, many open questions in the field of neutrino mixing and oscillations are outlined. In particular, in recent years, a number of anomalies were observed, which indicate the possibility of non-standard oscillations models, implying the existence of at least a fourth neutrino state, called *sterile neutrino* because it does not interact via any of the fundamental interactions of the Standard Model. In this Ph.D. thesis, a specific work on the light detection system of a Liquid Argon (LAr) detector for sterile neutrino search is illustrated.

In Chapter 1, a review of the present state-of-art of neutrino oscillation theory and of experimental suggestion for the existence of sterile neutrino state is described. The first hint of the presence of sterile neutrinos came from some anomalies observed by the Liquid Scintillator Neutrino Detector (LSND) experiment at Los Alamos. After that, further neutrino experiments with different sources exhibit a series of experimental anomalies, which are uncorrelated with each other but all attributable at the same oscillation phenomena. For this reason, a new generation of neutrino experiment is going to start, with the specific purpose to solve this puzzle.

In Chapter 2, the new Short Baseline Neutrino (SBN) physics program, emerging from an European - US collaboration, is illustrated. The program goal is to perform sensitive searches for sterile neutrinos at the eV mass-scale through both appearance and disappearance oscillation channels. The SBN program includes three Liquid Argon Time Projection Chamber (LAr-TPC) detectors namely the Short-Baseline Near Detector (SBND), Micro Booster Neutrino Experiment (MicroBooNE), and Imaging Cosmic And Rare Underground Signals (ICARUS) experiments, located on-axis along the Booster Neutrino Beam (BNB) at Fermilab. The size and position of the three detectors allow to characterize the beam before oscillations in the near detector and to measure simultaneously ν_e appearance and ν_μ disappearance in the MicroBooNE and ICARUS detectors.

This thesis is focused on the far detector of the SBN program, ICARUS T600. This cryogenic detector is the biggest LAr-TPC ever realized. It consists of a large cryostat split into two identical modules and filled with about 760 *tons* of ultra-pure LAr. The ICARUS experiment successfully operated at Gran Sasso National Laboratories (LNGS) with a remarkable detection efficiency and it completed a three years physics program being exposed to the CERN Neutrino to Gran Sasso (CNGS) muon neutrino beam from October 2010 to December 2012. After the CNGS beam shut down, the detector continued taking data with cosmic rays until the middle 2013. In 2014, the T600 was de-commissioned and transported to CERN, where a refurbishment program was performed before moving to FNAL. Various renovations were indeed necessary due to the experimental conditions at FNAL, where the detector will be at shallow depth rather than at deep underground as in LNGS.

In particular, in the last part of Chapter 2, the refurbishment operated on the T600 light collection system is illustrated. The improvement of the light collection system is needed due to the higher cosmic muons rate background at shallow depth, in order to detect with full efficiency the prompt scintillation light from events with energy depositions down to $\sim 100\ MeV$. The T600 light collection system consists of an array of cryogenic photomultiplier tubes (PMT) installed behind the wire planes of each TPC in a dedicated sustaining structure. However, the PMT photocathode is only sensitive to visible light, whereas the scintillation light produced in LAr by a ionizing event is emitted at VUV wavelength. The most efficient way to detect the scintillation light is to shift photons to a longer wavelengths where the PMT photocatode is sensitive.

Tetra-Phenyl-Butadiene (TPB) is the most common wavelength shifter used in LAr experiments, due to its extremely high efficiency to convert VUV photons into visible ones. In Chapter 3, the development of a new technique to obtain uniform coating of TPB on the PMT sensitive windows surface is described. It consists in evaporating TPB by means of a special type of crucible, a *Knudsen cell*, which allows to strictly control the process. The cell was placed inside a thermal evaporator, where a specific PMT rotating support was also installed. In the last part of this Chapter, a series of tests performed to verify the efficiency of the overall evaporation system, are illustrated. These type of tests were carried out by using two types of PMT mock-up in order to verify the density uniformity of the TPB coated layer as a function of the position on the PMT window.

The later step was to verify the quality of the evaporation device and process also in terms of light yield conversion. In Chapter 4, a new set of tests on samples previously obtained is illustrated. Tests were performed by using an optical device which allow to measure the overall Quantum Efficiency of a system consisting of a TPB coated photomultiplier. Further tests were also carried out by measuring the light yield conversion directly on some T600 photomultipliers in order to verify the success of the whole evaporation process.

CHAPTER 1

NEUTRINO OSCILLATION AND STERILE NEUTRINO

The Neutrino history starts in 1930, when a problem arose in the study of nuclear beta decay. In beta decay, a radioactive nucleus A is transformed into a lighter nucleus B with an electron emission:

$$A \to B + e^-$$

It was know that in a two-body decays, the energies of the outgoing particles are kinematically determined in the frame of the mass center. If the nucleus A is at rest, B and e^- resulting from the decay come out back-to-back with equal and opposite momenta. Then, based on the conservation of energy law, electron energy is given by the equation:

$$E = (\frac{m_A^2 - m_B^2 + m_e^2}{2m_A})c^2$$

It is essential to note that E is fixed once the three masses are specified. On the other hand, experiments showed a considerable variation of the emitted electron energy between zero and the prediction of the previous equation.

In 1930, W. Pauli suggested that another neutral particle was emitted with the electron, which carried off the missing energy. In the following 20 years, the existence of neutrinos was successfully accepted as explanation of the missing energy in beta decay and pion/muon decays, but there was still no direct experimental verification.

In 1956, Clyde Cowan and Frederick Reines observed neutrinos for the first time in the experiment now known as *Cowan Reines neutrino experiment.*

In this experiment, antineutrinos created in a nuclear reactor by beta decay, interacted with protons to produce neutrons and positrons:

$$\overline{\nu}_e + p \to n + e^+$$

The positron quickly finds an electron, and they annihilate each other. The two resulting gamma rays are detectable. The neutron can be detected by its capture on an appropriate nucleus after thermalisation, releasing delayed gamma rays. The delayed coincidence of both events, positron annihilation and neutron capture, gives a unique signature of an antineutrino interaction. In 1962, L.M. Lederman, M. Schwartz and J. Steinberger showed that more than one type of neutrino exists, by first detecting *muon* neutrino interactions. The discovery of the so-called *muon neutrino* strongly suggested a connection between neutrinos and lepton generations . When the third type of lepton, the tau lepton, was discovered in 1975 at the Stanford Linear Accelerator Center, it was expected the existence of an associated neutrino. The first direct detection of *tau neutrino* was announced in 2000 by the DONUT collaboration at Fermilab.

1.1 Neutrino interaction in the Standard Model

The Standard Model (SM) describes the strong, electromagnetic and weak interactions of elementary particles in the framework of quantum gauge field theory. In this model neutrinos are massless fermions, described by left-handed Weyl spinors and are subject neither to strong nor to electromagnetic interactions [1].
In the SM, three generations of neutrino are included as part of the left-handed lepton doublet:

$$L_l = \begin{pmatrix} \nu_{lL} \\ l_L \end{pmatrix} \qquad l = e, \mu, \tau$$

that obeys to the weak isospin SU(2) gauge symmetry. Standard neutrino interaction are described by the leptonic Charged Current (CC):

$$j^{\rho}_{W,L} = 2 \sum_{\alpha=e,\mu,\tau} \overline{\nu}_{\alpha,L} \gamma^{\rho} l_{\alpha,L} = \sum_{\alpha=e,\mu,\tau} \overline{\nu}_{\alpha,L} \gamma^{\rho} (1-\gamma^5) l_{\alpha} \tag{1.1}$$

and the neutrino part of the leptonic Neutral Current (NC):

$$j^{\rho}_{Z,\nu} = 2 \cdot \sum_{\alpha=e,\mu,\tau} \overline{\nu}_{\alpha,L} \gamma^{\rho} \nu_{\alpha,L} = \frac{1}{2} \sum_{\alpha=e,\mu,\tau} \overline{\nu}_{\alpha,L} \gamma^{\rho} (1-\gamma^5) \nu_{\alpha} \tag{1.2}$$

which enter, respectively, into the leptonic CC weak interaction Lagrangian

$$\mathcal{L}^{(CC)}_{I,L} = -\frac{g}{2\sqrt{2}} (j^{\rho}_{W,L} W_{\rho} + j^{\rho \mathrm{T}}_{W,L} W^{\mathrm{T}}_{\rho}) \tag{1.3}$$

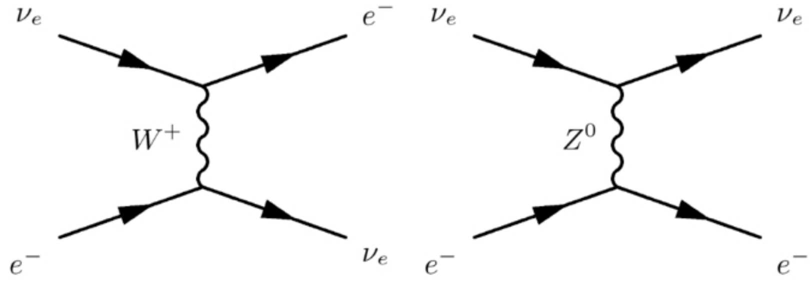

Figure 1.1: Charged Current and Neutral Current neutrino interaction Feynman diagram.

and the neutrino part of the leptonic NC weak interaction Lagrangian

$$\mathcal{L}_{I,\nu}^{(NC)} = -\frac{g}{2cos\vartheta_W} j_{Z,\nu}^{\rho} Z_{\rho} \tag{1.4}$$

where g is the SU(2) gauge coupling constant, ϑ_W is the Weinberg angle, W_ρ and Z_ρ are the fields of charged $W^{\pm}$ and neutral Z^0 vector bosons.
The Feynman diagrams for both NC and CC neutrino interaction are shown in Fig. 1.1.
This theoretical structure describes, with impressive accuracy, neutrino interactions. However, an intense experimental investigation performed with a wide variety of energies, sources, baseline lengths and detectors has led to the establishment of a scenario in which neutrinos change their flavour from the source to the detector. This characteristic can be explained with the mechanism of neutrino oscillations, first proposed by Pontecorvo in 1958 [2], as periodical transitions among different flavour neutrinos, which also implies massive neutrinos.

1.2 Neutrino oscillations

Experiments with solar, atmospheric, reactor and accelerator neutrinos have provided compelling evidences for the existence of *neutrino oscillations*, namely transitions in flight between the different flavour neutrinos ν_l.
Neutrino oscillations are a direct consequence of the presence of flavour neutrino mixing, or leptonic mixing, in vacuum and imply a neutrino mass greater than zero.
Consider a flavour neutrino state ν_l. If lepton mixing takes place and the masses m_j of all neutrinos ν_j are sufficiently small, the leptonic flavour state of the neutrino $|\nu_l\rangle$ will be a coherent superposition of the massive states $|\nu_j\rangle$:

$$|\nu_l\rangle = \sum_j U_{lj}^* |\nu_j\rangle \qquad l = e, \mu, \tau \qquad j = m_1, m_2, m_3 \tag{1.5}$$

where $U_{l,j}^*$ is an unitary matrix often called the Pontecorvo-Maki-Nakagawa-Sakata (PMNS) neutrino mixing matrix. The massive neutrino states $|\nu_j\rangle$ are eigenstates of the Hamiltonian:

$$\mathcal{H}\left|j\right\rangle = E_j \left|\nu_j\right\rangle$$

with energy eigenvalues:

$$E_j = \sqrt{\mathbf{p^2} + m_j^2}$$

The Schrödinger equation

$$i\frac{d}{dt}\left|\nu_j(t)\right\rangle = \mathcal{H}\left|\nu_j\right\rangle$$

implies that the massive neutrino states evolve in time as plane waves:

$$\left|\nu_j(t)\right\rangle = e^{-iE_jt}\left|\nu_j\right\rangle \tag{1.6}$$

Let us consider now a flavour state $\left|\nu_\alpha(t)\right\rangle$ which describes a neutrino created with a definite flavour α at time $t = 0$. From the equations (1.5) and (1.6), the time evolution of this state is given by:

$$\left|\nu_\alpha(t)\right\rangle = \sum_j U_{\alpha j}^* e^{-iE_jt}\left|\nu_j\right\rangle \tag{1.7}$$

For simplicity, we consider a finite normalization volume V in order to have orthonormal massive neutrino states:

$$\left\langle\nu_\alpha|\nu_\beta\right\rangle = \delta_{\alpha\beta}$$

Then, using the unitarity relation:

$$U^T U = 1 \Leftrightarrow \sum_\alpha U_{\alpha j}^* U_{\alpha l} = \delta_{lj}$$

the massive states can be expressed in terms of flavour states inverting the equation (1.5):

$$\left|\nu_j\right\rangle = \sum_l U_{lj}\left|\nu_l\right\rangle \tag{1.8}$$

Substituting the equation (1.8) into equation (1.7), we obtain:

$$\left|\nu_\alpha(t)\right\rangle = \sum_{\beta=e,\mu,\tau}\left(\sum_j U_{\alpha j}^* e^{-iE_jt} U_{\beta j}\right)\left|\nu_\beta\right\rangle \tag{1.9}$$

Hence, the superposition of the massive neutrino states $\left|\nu_\alpha(t)\right\rangle$, which turns out in a pure flavour state at $t = 0$, becomes a superposition of different flavour states at $t > 0$ if the mixing matrix U is not diagonal, namely if neutrinos are mixed.

The coefficient of $\left|\nu_\beta\right\rangle$:

$$A_{\nu_\alpha \to \nu_\beta}(t) \equiv \langle \nu_\alpha | \nu_\beta \rangle = \sum_j U^*_{\alpha j} U_{\beta j} e^{-iE_j t} \tag{1.10}$$

is the $\nu_\alpha \to \nu_\beta$ transition amplitude as a function of time.
Then, the transition probability $P_{\nu_\alpha \to \nu_\beta}(t)$ is given by:

$$P_{\nu_\alpha \to \nu_\beta}(t) = |A_{\nu_\alpha \to \nu_\beta}(t)|^2 = \sum_{j,k} U^*_{\alpha j} U_{\beta j} U_{\alpha k} U^*_{\beta j} e^{-i(E_j - E_k)t} \tag{1.11}$$

Neutrinos are highly relativistic, so the energy-momentum relation can be approximated by:

$$E_j \simeq E + \frac{m_j^2}{2E}$$

where E is the kinematic energy of the neutrino.
In this approximation:

$$E_j - E_k \simeq \frac{\Delta m^2_{jk}}{2E}$$

where

$$\Delta m^2_{jk} = m_j^2 - m_k^2$$

Therefore, the transition probability in equation (1.11) can be approximated by:

$$P_{\nu_\alpha \to \nu_\beta}(t) = |A_{\nu_\alpha \to \nu_\beta}(t)|^2 = \sum_{j,k} U^*_{\alpha j} U_{\beta j} U_{\alpha k} U^*_{\beta j} \ exp \left(-i \frac{\Delta m^2_{jk} t}{2E} \right) \tag{1.12}$$

The final step in the standard derivation of the neutrino oscillation probability concerns the propagation time t which is unknown in neutrino oscillation experiments. What is known is the distance L between the source and the detector. Since ultrarelativistic neutrinos propagate almost at the speed of light, it is possible to approximate $t = L$, leading to the final equation:

$$P_{\nu_\alpha \to \nu_\beta}(LE) = |A_{\nu_\alpha \to \nu_\beta}(t)|^2 = \sum_{j,k} U^*_{\alpha j} U_{\beta j} U_{\alpha k} U^*_{\beta j} \ exp \left(-i \frac{\Delta m^2_{jk} L}{2E} \right) \tag{1.13}$$

This expression shows that the phases of neutrino oscillations

$$\Phi_{jk} = -\frac{\Delta m^2_{jk} L}{2E}$$

is determined by the source–detector distance L and the neutrino energy E which are quantities depending on the experiment.
Of course, the phases are determined also by the squared-mass differences

Δm^2_{jk} which are physical constants. It is clear that transitions among different neutrino flavours manifest only for $L > 0$, because the unitarity relation implies that:

$$P_{\nu_\alpha \to \nu_\beta}(L = 0, E) = \delta_{\alpha\beta}$$

It is then possible to define the *oscillation length* as the distance at which the phase generated by Δm_{jk} becomes equal to 2π:

$$L_{jk} = \frac{4\pi E}{\Delta m^2_{jk}} \tag{1.14}$$

Let us consider the simple case of an oscillation between two neutrino flavour states only. In this case, the mixing matrix U can be written as:

$$\begin{pmatrix} cos\vartheta & sin\vartheta \\ -sin\vartheta & cos\vartheta \end{pmatrix}$$

Then, the transition probability is:

$$P_{\nu_\alpha \to \nu_\beta} = sin^2(2\vartheta) sin^2\left(\frac{\Delta m^2_{\alpha\beta} L}{4E}\right) \tag{1.15}$$

The transition probability is here expressed in natural unit ($c = 1, \hbar = 1$). Converting in practical units (valid for most the experimental setup):

$$P_{\nu_\alpha \to \nu_\beta} = sin^2(2\vartheta) sin^2\left(1.27\frac{\Delta m^2_{\alpha\beta} L}{E}\right) \tag{1.16}$$

where L is measured in km, E in GeV and m in eV. The angle ϑ is the so-called *mixing angle*. It defines how different the flavour states are from the mass states. If $\vartheta = 0$, the flavour states are identical to the mass states and ν_j will propagate from source to detector with a definite momentum. Clearly in this case, oscillations cannot happen.

In the case of three neutrinos, the mixing matrix becomes more complex, with three mixing angle $\vartheta_{12}, \vartheta_{23}, \vartheta_{13}$ and a single phase δ related to charge-parity violations. Its most common parametrization is written as:

$$\begin{pmatrix} 1 & 0 & 0 \\ 0 & c_{23} & s_{23} \\ 0 & -s_{23} & c_{23} \end{pmatrix} \begin{pmatrix} c_{13} & 0 & s_{13}e^{-i\delta} \\ 0 & 1 & 0 \\ -s_{13}e^{i\delta} & 0 & c_{13} \end{pmatrix} \begin{pmatrix} c_{12} & s_{12} & 0 \\ -s_{12} & c_{12} & 0 \\ 0 & 0 & 1 \end{pmatrix} \tag{1.17}$$

where s_{ij} and c_{ij} are used to denote $sin\vartheta_{ij}$ and $cos\vartheta_{ij}$ respectively. It is also clear from eq.(1.16) that in order to have neutrino oscillations, at least one of the mass states must be non-zero. This simple statement has huge implications for oscillations to happen, namely the neutrino must have mass. Further the masses of the mass states must be different.

From an experimental point of view, L/E is the variable parameter of a neutrino oscillation experiment. For a given Δm^2, the probability of oscillation

Mixing element	Best fit ($\pm 1\sigma$)
$sin^2(\vartheta_{12})$	0.304 ± 0.014
Δm^2_{21}	$(7.53 \pm 0.18) \times 10^{-5} eV^2$
$sin^2(\vartheta_{23})$	0.510 ± 0.005 (normal mass hierarchy)
$sin^2(\vartheta_{23})$	0.500 ± 0.005 (inverted mass hierarchy)
Δm^2_{32}	$(2.44 \pm 0.06) \times 10^{-3} eV^2$ (normal mass hierarchy)
Δm^2_{32}	$(2.51 \pm 0.06) \times 10^{-3} eV^2$ (inverted mass hierarchy)
$sin^2(\vartheta_{13})$	$(2.19 \pm 0.12) \times 10^{-2}$

Table 1.1: Values obtained through data analysis based on the 3-neutrino mixing scheme described in [3] by K.Nakamura and S.T.Petcov.

will change as one moves away from the source, or scans over different neutrino energies.

1.2.1 Neutrino oscillations experiments

In the last decades, numerous neutrino experiments were realised in order to verify the reliability of the neutrino oscillations theoretical model and to determinate the mixing matrix elements. Combining the data produced by the experiments with solar, atmospheric, reactor and accelerator neutrinos have provided all the mixing angles ϑ_{ij} of the mixing matrix U as well as the difference of the squared masses Δm^2_{ij}. The global fit values of all experimental results are reported in Tab. 1.1 [3] and plotted in Fig. 1.2.

After the incredible experimental progress made in the studies of neutrino oscillation, further understanding of the pattern of neutrino masses and neutrinos mixing, of their origin and of the status of CP symmetry in lepton interaction are now possible. In particular, the main goals for the new generation of neutrino experiments include the determination of the neutrino Dirac or Majorana nature (see [1] for details) and the status of CP symmetry in the lepton sector. Even the neutrino mass hierarchy and the absolute scale of neutrino masses are subject of study.

Another key point concerns a series of experimental anomalies, which are uncorrelated with each other but all hinting at oscillation phenomena driven by Δm^2 and $sin^2 2\vartheta$ parameters not compatible with the values in Tab. 1.1.

1.3 Sterile Neutrino

Even though the mixing of the 3 flavour neutrino states has been experimentally well established, there are possible hints for the presence in the mixing of at least one additional neutrino state with mass of the order of eV. If this state exists, it must be related to the existence a non interacting neutrino flavour, called *sterile neutrino* which mix with the other neutrino flavours (*active neutrinos*).

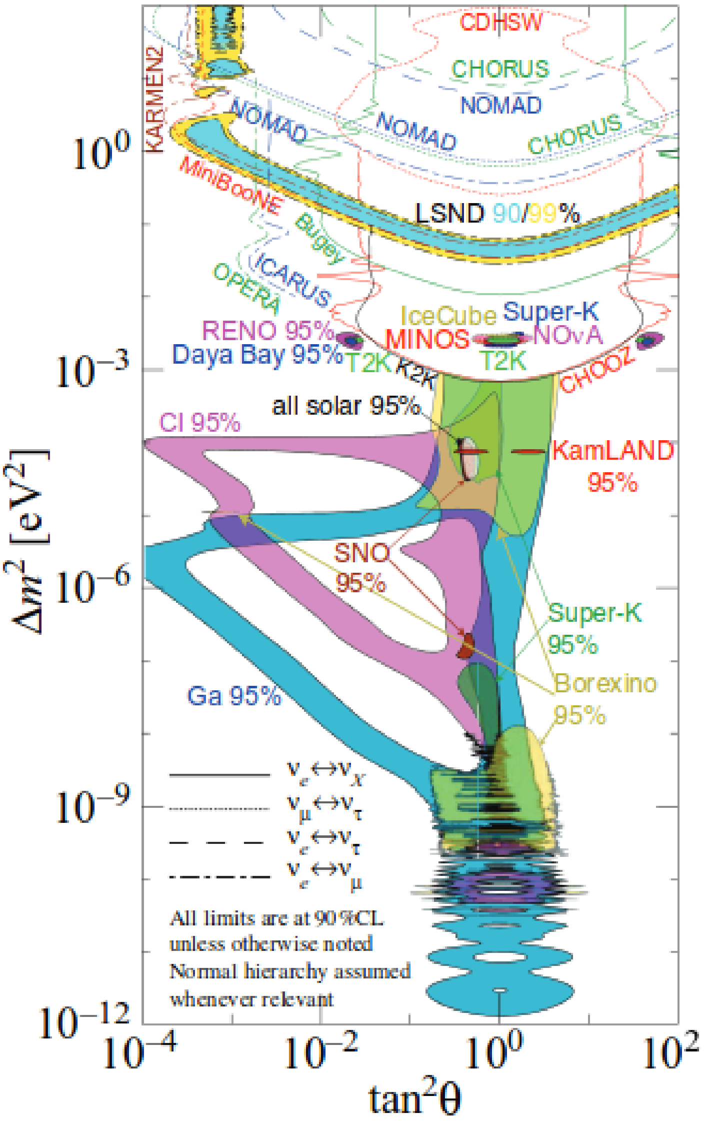

Figure 1.2: The regions of squared-mass splitting and mixing angle favoured or excluded by various neutrino oscillation experiments

The main hints under discussion have been obtained: in the LSND $\overline{\nu}_\mu \to \overline{\nu}_e$ appearance experiment [4], in which a significant excess of event over the background has been observed; from the analysis of the $\overline{\nu}_\mu \to \overline{\nu}_e$ [5] and $\nu_\mu \to \nu_e$ [6] appearance data of MiniBooNE experiment; from the reanalysis of the short baseline (SBL) reactor neutrino oscillation data [7] and from the data of the radioactive source calibration of GALLEX [8] and SAGE [9] solar neutrino experiments.

1.3.1 Short baseline experiments

The first evidence of anomalies in the 3-flavour neutrino mixing scenario came from the Liquid Scintillator Neutrino Detector (LSND) experiment at Los Alamos [10]. It was a scintillation and Cherenkov light detector designed to search with high sensitivity for $\overline{\nu}_\mu \to \overline{\nu}_e$ oscillations from μ^+ decay at rest. The detector consisted of a tank filled with 167 *tons* of mineral oil and 6.4 *kg* of organic scintillator material. Cherenkov light emitted by particle interactions was detected by an array of 1220 photomultiplier tubes. The experiment collected data from 1993 to 1998. The final result from the LSND experiment was the evidence of a $\overline{\nu}_\mu \to \overline{\nu}_e$ oscillation signal due to events with positrons with energy between 20 and 200 MeV spatially and temporarily correlated with γ rays of 2.2 MeV. An excess of ν_e over the expected from background and standard oscillation was found, with an oscillation probability of $(0.264 \pm 0.067 \pm 0.045)\%$, leading to a $> 3\sigma$ evidence for $\overline{\nu}_\mu \to \overline{\nu}_e$ oscillation with $\Delta m^2 > 0.2\ eV^2$, much higher than the standard value reported above in Table 1.1.

The short baseline neutrino oscillation experiment MiniBooNE at Fermilab investigated ν_e appearance and $\overline{\nu}_e$ appearance in ν_μ and $\overline{\nu}_\mu$ beams respectively. The detector consists of a spherical vessel containing 807 *tons* of mineral oil. Cherenkov light and isotropic scintillation light were detected by 1280 photomultiplier tubes in an optically insulated region while an outer region equipped with 240 photomultiplier tubes acted as veto in anti-coincidence. In antineutrino running mode a 2.8 σ excess of events over background was observed in the energy range of $200 < E_\nu < 1250$ MeV in the CC quasi-elastic scattering interaction. An excess of corresponding events was observed in particular in the range of energies $200 < E_\nu < 475$ MeV, corresponding to L/E regions outside that probed in LSND experiment. This result, interpreted in terms of $\nu_\mu \to \nu_e$ oscillations corresponds to an allowed region in the $sin^2(2\vartheta - \Delta m^2)$ plane which overlaps the allowed region obtained from the LSND experiment (Fig. 1.3).

1.3.2 Reactor anomaly

Reactor experiments [11] have played an important role in the understanding of neutrino oscillation pattern. Nuclear reactors are very intense sources of

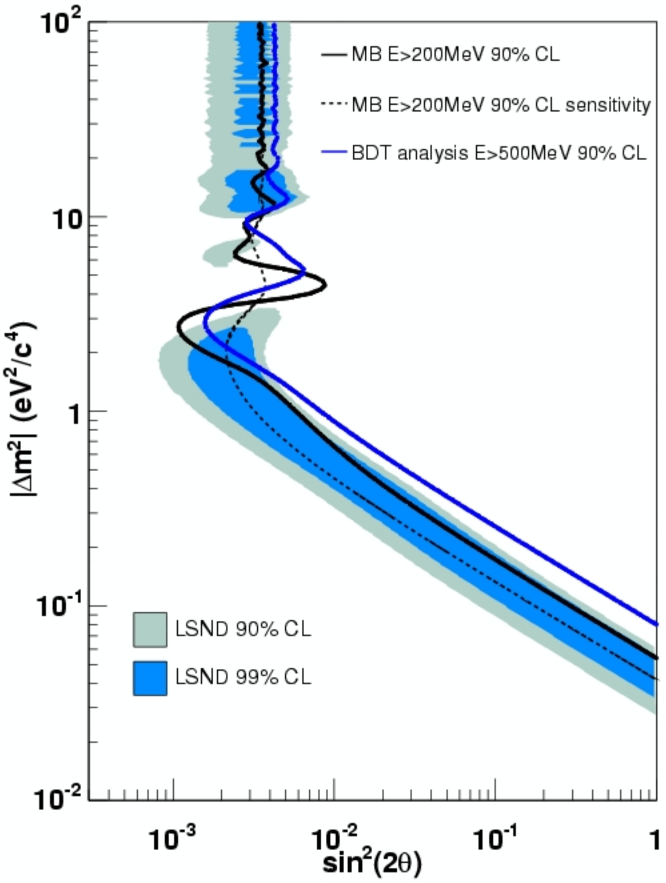

Figure 1.3: Sensitivity (dashed black line) and limit (solid black line) from a fit of the MiniBooNE antineutrino data to a two-neutrino mixing hypothesis and comparison with LSND-allowed regions.

electron anti-neutrinos, which are produced through β^- decay chains of the fission products. The neutrino oscillation search at a reactor is usually based on a disappearance measurements. The observed neutrino rate and possibly spectrum at a distance L from the reactor is compared to the expected spectrum. If a deficit is found it can be explained in terms of disappearance probability. The basic set-up of modern reactor experiments typically consists of identical near and far detectors. The near detector is typically at an average distance of $200 - 300$ m from the nuclear reactor cores and the far detector is at 1000 m. The nuclear reactors used by the reactor experiments are pressurized water reactors (PWR) and their number and distances with respect to the near detectors varies between experiments.
The reactor neutrino anomaly is related to the result of a new calculation of the reactor $\overline{\nu}_e$ fluxes, which was done in preparation for the Double Chooz reactor experiment [12]. The method relies on detailed knowledge of the decays of thousands of fission products, while the previous conversion procedure used a phenomenological model based on 30 effective β-decay branches. In the new calculation, the actual neutrino fluxes result approximately 3.5% larger than the previous calculation used in the past in the interpretation of the data of the SBL reactor $\overline{\nu}_e$ oscillation experiment. Although this increase has no significant effect on KamLAND solar parameter results, when combined with the previously reported small deficits at nearer distances, it results in a larger average deficit of 5.7%, at $R = 0.943 \pm 0.024$ (Fig. 1.4) where R is the expected-to-calculated ratio. If this deficit is due to neutrino mixing, it could be explained by an energy-independent suppression of the ν_e flux at distances ≥ 15 meters. This requires a neutrino with a new $\Delta m^2 \geq 1$ eV^2. If the neutrino mixing hypothesis is the correct explanation, this suggests the existence of a fourth neutrino state. However, it is important to note that other explanations are also possible, such as a correlated variable in the experiments, or an erroneous prediction of the antineutrino flux from nuclear reactor cores.

1.3.3 Gallium experiments

SAGE (Soviet American Gallium Experiment) and GALLEX (GALLium EXperiment) were two radiochemical solar neutrino detection experiment based on the ν_e capture reaction of gallium:

$$\nu_e +^{71} Ga \to e^- +^{71} Ge$$

The SAGE detector consisted of 60 *tons* of metallic gallium stored deep underground at the Baksan Neutrino Observatory in the Caucasus mountains in Russia. The experiment began to measure the solar neutrino capture rate with the target of gallium metal in December 1989 and it ran up to 2003.
The GALLEX detector consisted of a 54 m^3 detector tank filled with 101 *tons* of gallium trichloride-hydrochloric acid solution, which contained 30.3 *tons* of gallium. The experiment ran from 1991 to 1997 at the LNGS (Laboratori

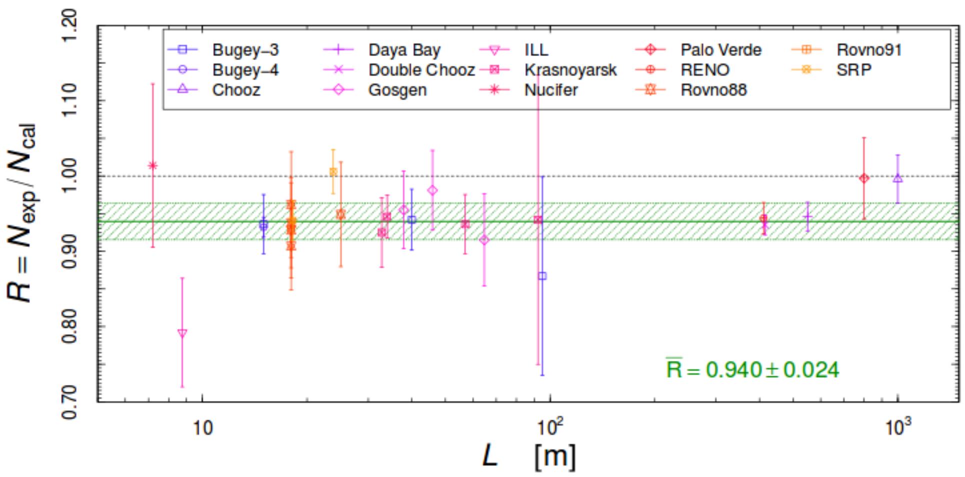

Figure 1.4: Ratios of the reactor experiments considered in the new analysis as functions of the reactor-detector distance L. The horizontal band shows the average ratio R and its uncertainty. The error bars show the experimental uncertainties [14].

Nazionali del Gran Sasso).
During their calibration procedures, they also showed a deficit of the measured ν_e fluxes compared to the expected fluxes which might be interpreted as ν_e disappearance. This calibration procedure consisted in introducing intense ^{51}Cr and ^{37}Ar radioactive sources inside the detectors and counting the number of ^{71}Ge contaminating the ^{71}Ga as a consequence of the reaction shown above. The results of these gallium radioactive source experiments [13] indicated a ratio R of measured and predicted ^{71}Ge event rates which was smaller than unity:

$$R^B_{G1} = 0.953 \pm 0.11$$

$$R^B_{G2} = 0.812^{+0.10}_{-0.11}$$

$$R^B_{S1} = 0.95 \pm 0.12$$

$$R^B_{S2} = 0.791^{+0.084}_{-0.078}$$

where G1 and G2 denote the two GALLEX calibrations with ^{51}Cr sources, S1 denotes the SAGE experiment with a ^{51}Cr source and S2 denotes the SAGE calibration with a ^{37}Ar source. The value of the ratio averaged between the two experiment is then:

$$R = 0.86 \pm 0.50$$

Thus, the number of measured events is $\sim 2.8\sigma$ smaller than the prediction. This is the so called *gallium anomaly*. The analysis of the data in terms of neutrino oscillations indicates values of the oscillation amplitude $sin^2 2\vartheta \geq 0.07$ and squared-mass difference $\Delta m^2 \geq 0.35\ eV^2$ at 99% C.L. (Fig. 1.5).

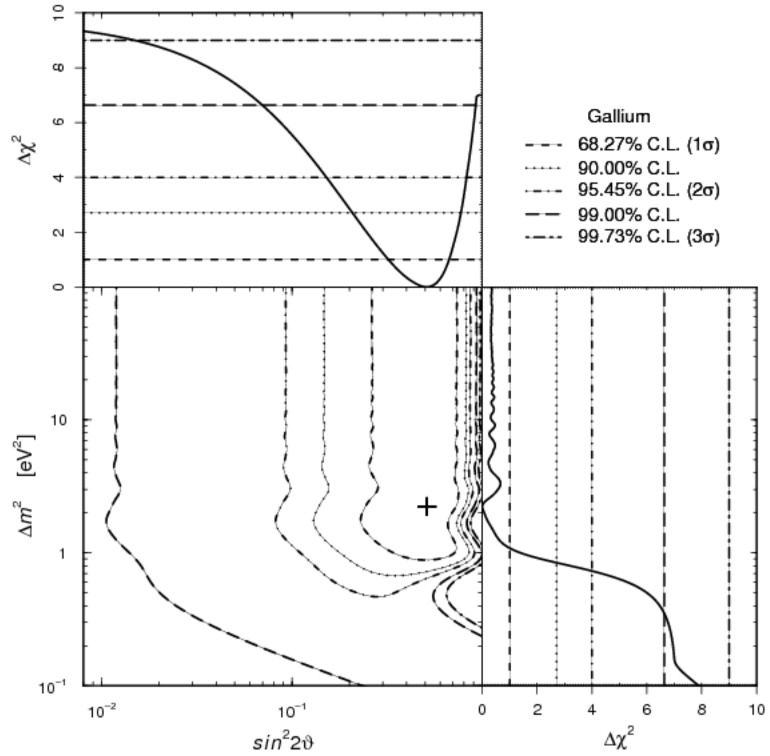

Figure 1.5: Allowed regions in the $sin^2 2\vartheta - \Delta m^2$ plane and marginal χ^2 for $sin^2 2\vartheta$ and Δm^2 obtained from the combined fit of the results of the two GALLEX ^{51}Cr radioactive source calibrations and the SAGE ^{51}Cr and ^{37}Ar radioactive source calibrations.

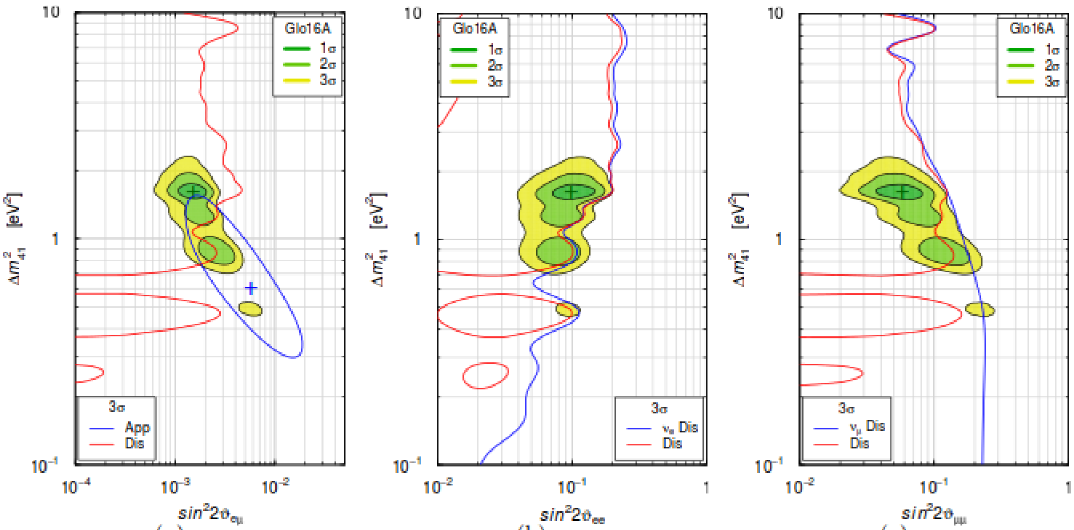

(a) (b) (c)

Figure 1.6: Allowed regions in the $sin^2 2(\vartheta e\mu) - \Delta m^2_{41}$ (a), $sin^2 2(\vartheta ee) - \Delta m^2_{41}$ (b) and $sin^2 2(\vartheta \mu\mu) - \Delta m^2_{41}$ (c) planes obtained in the 3+1 global fit "Glo16A" of the 2016 SBL data without the MINOS and IceCube data. There is a comparison with the 3σ allowed regions obtained from $\overline{\nu}_\mu \to \overline{\nu}_e$ SBL appearance data (App) and the 3σ constraints obtained from $\overline{\nu}_e$ SBL disappearance data (ν_e Dis), $\overline{\nu}_\mu$ SBL disappearance data (ν_μ Dis) and the combined $\overline{\nu}_e$ and $\overline{\nu}_\mu$ SBL disappearance data (Dis). The best-fit points of the Glo16A and App fits are indicated by crosses.

1.3.4 Global fit scenario

A possible phenomenological model with light sterile neutrinos is widely used in order to explain the anomalies in neutrino oscillation pattern described above: the so called 3+1 model. According to this model, the existing neutrino states are the three interacting lepton flavours and a fourth non-interacting *sterile* neutrino state. Global analysis of all the data relevant for the sterile neutrino hypothesis were performed [14]. The results of the $3+1$ global fit are shown in Table 1.2(a) and in Fig. 1.6. The allowed regions in the $sin^2 2(\vartheta_{e\mu}) - \Delta m^2_{41}$, $sin^2 2(\vartheta_{ee}) - \Delta m^2_{41}$ and $sin^2 2(\vartheta_{\mu\mu}) - \Delta m^2_{41}$ planes are shown, obtained with a fit, indicated as Glo16A in the picture, that does not include data from MINOS and IceCube.

1.3.5 Effects of MINOS and Ice Cube

MINOS (Main Injector Neutrino Oscillation Search) is a particle physics experiment designed to study the phenomena of neutrino oscillations [15]. Neutrinos produced by the NuMI (Neutrinos at Main Injector) beamline at Fermilab are observed by a near and far detector. The near detector is located at Fermilab, at the source of the neutrinos, while the other is located 450 miles away,

Mixing element	Global fit (a)	Global fit (b)
Δm^2_{41}	1.6	1.7
$\lvert U_{e4}\rvert^2$	0.024	0.024
$\lvert U_{\mu 4}\rvert^2$	0.011	0.0092
$sin^2(\vartheta_{e\mu})$	0.0010	0.00089
$sin^2(\vartheta_{e\mu})$	0.095	0.095
$sin^2(\vartheta_{e\mu})$	0.042	0.036

Table 1.2: Mixing parameters resulting from the global $3+1$ fits without (a) and with (b) the MINOS and IceCube data.

in northern Minnesota. Both MINOS detectors are steel-scintillator sampling calorimeters made out of alternating planes of magnetized steel and plastic scintillators. The experiment measures the difference in neutrino beam composition and energy distribution in the near and far detectors.

The IceCube Neutrino Observatory is a neutrino telescope constructed at the Amundsen–Scott South Pole Station in Antarctica [16]. Its thousands of sensors are distributed over a cubic kilometre of volume inside the Antarctic ice. The in-ice component of IceCube detector consists of more than 5000 spherical optical sensors called Digital Optical Modules (DOMs), each with a photomultiplier tube and a single board data acquisition computer. DOMs are deployed on strings of sixty modules each at depths ranging from 1.450 to 2.450 meters, into holes melted in the ice. The IceCube detector measures the incoming μ generated by the interaction of the atmospheric $\overline{\nu}_\mu$ with the surrounding earth and ice, as a function of the neutrino energy and of the zenith angle. The sterile neutrino influence on the observed flux is given by the matter effects that modify the oscillation patterns inside the Earth. In Table 1.2 (b) and Fig. 1.7 the $3+1$ global fit with the addition of the 2016 data from MINOS and IceCube is shown. Comparing Fig. 1.6(c) with Fig. 1.7(c), one can see that the addition of the MINOS and IceCube data leads to the exclusion of the high-$sin^2 2(\vartheta_{\mu\mu})$-low-$\Delta m^2_{41}$ part of the allowed region, as expected. On the other hand, the low-$sin^2 2(\vartheta_{\mu\mu})$-high-$\Delta m^2_{41}$ part of the allowed region is practically unaffected by the MINOS and IceCube constraints. As a consequence, also the high-$sin^2 2(\vartheta_{e\mu})$-low-$\Delta m^2_{41}$ part of the allowed region in Fig. 1.6(a) is excluded in Fig. 1.7(a), whereas the low-$sin^2 2(\vartheta_{e\mu})$ -high- Δm^2_{41} part of the allowed region is practically unaffected. The MINOS and IceCube data give information not only on the 3+1 mixing parameters Δm^2_{41}, $\lvert U_{e4}\rvert^2$ and $\lvert U_{\mu 4}\rvert^2$but also on $\lvert U_{\tau 4}\rvert^2$. The sensitivity to $\lvert U_{\tau 4}\rvert^2$is due in MINOS to the neutral-current event sample [17] and in IceCube to the matter effects [18] for high-energy neutrinos propagating in the Earth, which depend on all the elements of the mixing matrix.

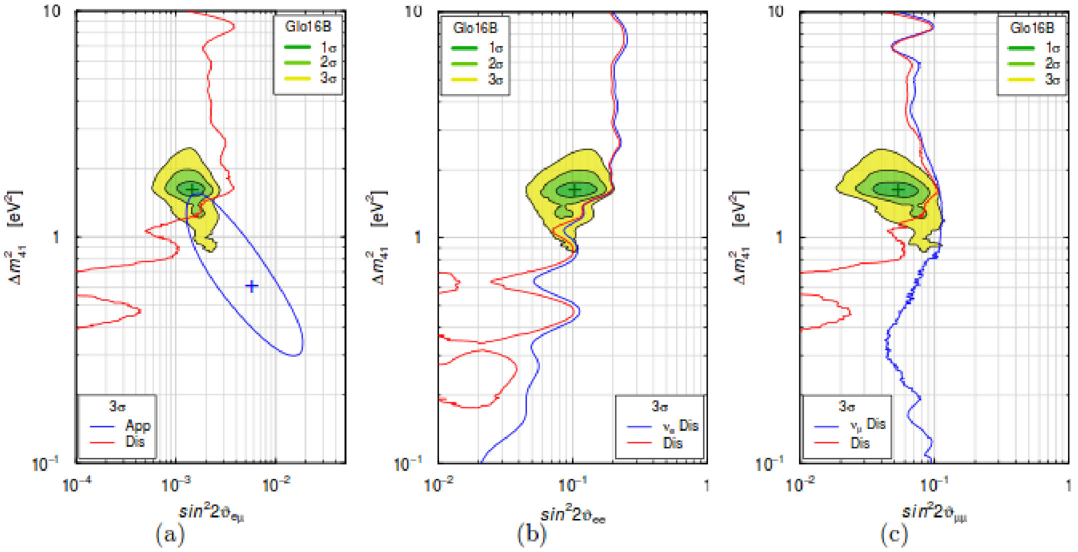

(a) (b) (c)

Figure 1.7: Allowed regions in the $sin^2 2(\vartheta_{e\mu}) - \Delta m^2_{41}$ (a), $sin^2 2(\vartheta_{ee}) - \Delta m^2_{41}$ (b) and $sin^2 2(\vartheta_{\mu\mu}) - \Delta m^2_{41}$ (c) planes obtained in the 3+1 global fit "Glo16B" of all the 2016 SBL data (MINOS and IceCube included). There is a comparison with the 3σ allowed regions obtained from $\overline{\nu}_\mu \rightarrow \overline{\nu}_e$ SBL appearance data (App) and the 3σ constraints obtained from $\overline{\nu}_e$ SBL disappearance data (ν_e Dis), $\overline{\nu}_\mu$ SBL disappearance data (ν_μ Dis) and the combined $\overline{\nu}_e$ and $\overline{\nu}_\mu$ SBL disappearance data (Dis). The best-fit points of the Glo16B and App fits are indicated by crosses.

1.4 Conclusions and future experiments

LSND and Gallium anomalies opened new questions on neutrino oscillation physics. Other regions of the parameter space of the 3+1 neutrino mixing must be explored by new experiments in order to figure out the anomalies nature. For sure, an experimental confirmation of the existence of these oscillation, and then of the sterile neutrino, would imply that new particles with properties outside the framework of the Standard Model exist and their discovery would open a prodigious window on new low-energy physics.
To proceed forward with the goal to establish or refute the existence of sterile neutrinos, numerous new experiments with different approaches are or will become operating in the next few years. Some of the most interesting projects are listened below:

- **JUNO** The Jiangmen Underground Neutrino Observatory (JUNO) is a large liquid scintillator detector located at 53 km distance from reactors [19]. The detector will be located 1800 meters of water equivalent (m.w.e.) underground and consists of a 20 kiloton liquid scintillator (based on LAB doped with PPO and bis-MSB) contained in a huge 35.4 m diameter acrylic sphere instrumented by more than 17000 20 in. and about 34000 3 in. PMTs. JUNO plans to start data taking in 2020.

- **Hyper-Kamiokande** The Hyper-Kamiokande detector (HK) is a proposed next-generation water-Cherenkov detector [20]. It will serve as far detector of a long-baseline neutrino experiment T2HK (Tokai-to-Hyper-Kamiokande) using neutrino and antineutrino beams. It will consist of two cylindrical tanks for a total fiducial mass of 0.52 Mton, making it about 10 times larger than its predecessor Super-Kamiokande. It will use 40,000 PMTs per tank to reach the same 40% photo-coverage. In case of approval, the construction of Hyper-Kamiokande can start in 2018 and data taking is expected to begin in 2026.

- **DUNE** The main scientific goals of the Deep Underground Neutrino Experiment (DUNE) [21] are the sensitive test of CP violation in the leptonic sector, the determination the neutrino mass hierarchy, and the precise measurements of neutrino oscillation parameters. The near detector baseline design is a fine-grained tracker in a magnetic field, complemented by calorimetry and muon range detector. It will be located at a distance of 574 m from the target, at a depth of 65 m.
  The far detector will consist of four cryostats instrumented with Liquid Argon Time Projection Chambers (LAr TPCs) with a fiducial mass of 40 kton. The first DUNE liquid argon module adopts a single-phase technology pioneered by ICARUS T600 detector. A prototype of the single-phase TPC will be constructed and tested at CERN.
  The second DUNE far detector module can be constructed on the basis of a dual-phase TPC if its performance will be confirmed as a result of

the WA105 project at the CERN Neutrino Platform [22]. The prototype detectors are expected to start taking beam data at CERN in 2018, whereas DUNE will begin data taking with the first 10 kton module in 2026 and the full configuration will be ready by 2029.

CHAPTER 2

THE ICARUS T600 NEW LIGHT DETECTION SYSTEM IN THE SBN PROGRAM

As seen in the previous Chapter, the experimental observations of neutrino oscillations have established a picture consistent with the mixing of three neutrino flavours ν_e, ν_μ and ν_τ with three mass eigenstates ν_1, ν_2 and ν_3 whose mass differences turn out to be relatively small, with $\Delta m^2_{21} \simeq 7.5 \times 10^{-5}\ eV^2$ and $|\Delta m^2_{32}| \simeq 2.4 \times 10^{-3}\ eV^2$. However, in recent years, several experimental anomalies have been reported which could be hinting at the presence of additional neutrino states with larger mass-squared differences participating in the mixing.

The new Short Baseline Neutrino (SBN) physics program will deliver a rich and compelling physics opportunity, including the possibility to investigate the experimental anomalies in neutrino physics and to perform the most sensitive search to data for sterile neutrinos at the eV mass-scale [23].

The SBN program includes three Liquid Argon Time Projection Chamber (LAr-TPC) detectors namely the Short-Baseline Near Detector (SBND), Micro Booster Neutrino Experiment (MicroBooNE), and Imaging Cosmic And Rare Underground Signals (ICARUS) experiments, located on-axis along the Booster Neutrino Beam (BNB) at Fermilab. The size and position of the three detectors allow to characterize the beam before oscillations in the near detector and to measure simultaneously ν_e appearance and ν_μ disappearance in the MicroBooNE and ICARUS detectors.

The SBN detectors will also record events from the off-axis flux of the NuMI neutrino beam with its higher electron neutrino content and different energy

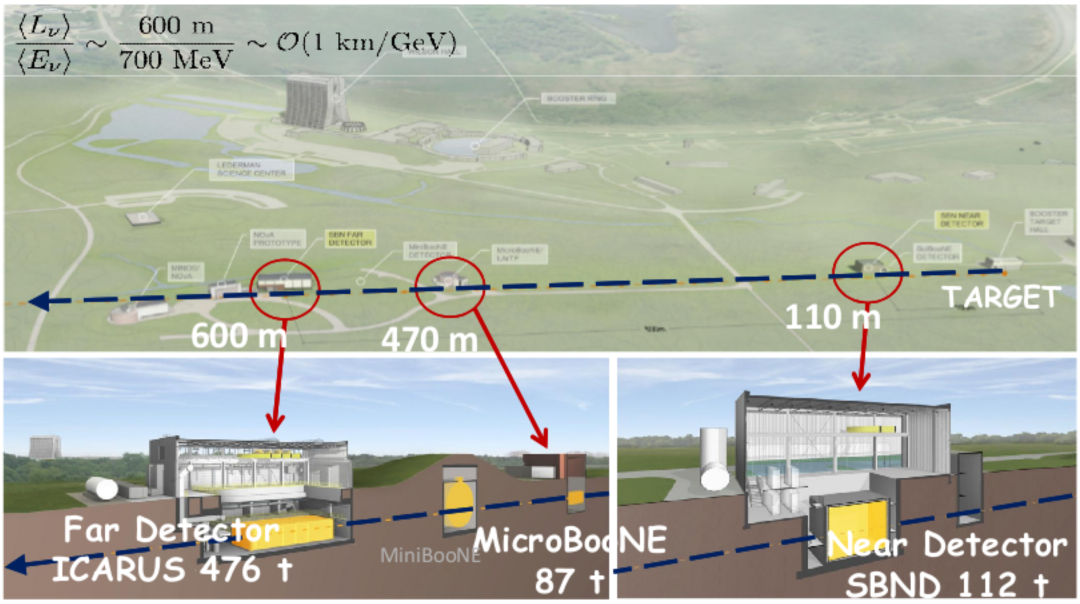

Figure 2.1: Map of the Fermilab neutrino beamline area showing the axis of the BNB (blue dashed line) and locations of the SBN detectors at 110 m, 470 m and 600 m.

spectrum.

2.1 SBN neutrino sterile search

Multiple LAr-TPC detectors at different distances along the BNB will allow a very sensitive search for high Δm^2 neutrino oscillations in multiple channels. These searches, constituting the main measurements of the SBN program, are based on a sensitive analysis on $\nu_\mu \rightarrow \nu_e$ appearance and $\nu_\mu \rightarrow \nu_x$ disappearance.
Electron neutrino event candidates include background events due to the intrinsic beam ν_e charged-current (CC) interactions as well as other beam-related (mostly ν_μ -induced) mis-identified backgrounds. The event selection criteria are given below and are applied identically to all the three detectors:

- **ν_e CC:** Charged Current interactions producing an electron with $E_e > 200\ MeV$ are accepted with an assumed 80% identification efficiency. The absolute efficiency will depend on the final event selections for example to address cosmogenic photon backgrounds;
- **NC π^0 production:** Neutral Current interactions with any number of π^0 in the final state are considered as possible background events. If more than one photon from pion decays converts within the fiducial volume, the event is not considered as background. For events where only one photon converts within the fiducial volume, the rejection rate is 94%;

- **NC γ production:** Neutral Current interactions resulting in photons in the final state (not from π^0 decays) are also considered as background if the photon converts within the fiducial volume and 6% of these events are accepted into the ν_e candidate sample;
- **ν_μ CC:** ν_μ Charged Current interactions in the presence of an identified primary e.m. shower within the fiducial volume could be mis-identified as electron neutrino interactions if the muon is not identified.

Bringing together the background predictions and uncertainty estimations [24], it is possible to construct the experimental sensitivity to a $\nu_\mu \rightarrow \nu_e$ oscillation signal.

Figure 2.2 shows the full ν_e background predictions in each detector. On the left is shown the result when using topological cuts [24] to reduce cosmic backgrounds. The analysis demonstrates the power of TPC information alone in reducing the backgrounds, rejecting more than 99% of cosmogenic photons when their parent muon is also visible in the TPC. However, as can be seen in figures, the cosmogenic backgrounds remain a large contribution to the analysis, particularly at low energies. On the right, the potential improvement when employing additional hardware solutions is shown. In particular, precise timing information can improve the TPC data by rejecting triggers in which a cosmic interaction occurs in the detector within the 1.6 μs beam spill time.

Figure 2.3 presents the experimental sensitivity of the proposed SBN program to $\nu_\mu \rightarrow \nu_e$ appearance signals in the $\Delta m^2 - sin^2 2\vartheta$ plane compared to the original LSND allowed region [4]. The sensitivity shown includes the additional 95% cosmic background rejection coming from timing information described above and illustrated on the right in Figure 2.2.

2.2 The Booster Neutrino Beam (BNB)

The SBN program will use the existing Booster Neutrino Beamline (BNB) at FNAL. The BNB is a conventional horn focused neutrino beam, fed with 8 GeV protons from Fermilab's Booster accelerator.

In the existing beamline configuration the 8 GeV protons from the booster are guided through the transport line to the target hall. The primary beamline ends with a quadrupole triplet that focuses the beam on the target. The target is embedded within the 1.8 m long horn and the target horn assembly lies just downstream of the final triplet. A 2.14 m long collimator about 3 m downstream of the target shields the entrance to the decay pipe region. The booster operates at 15 Hz repetition rate with up to 5 Hz average rate delivered to BNB. The intensity per spill is typically about 4.5×10^{12} protons. The time structure of individual beam spills is determined by the booster parameters. The harmonic number for BNB is 84 and the RF frequency is 53 MHz. This results in 1.6μs long spills composed of a train of 81, roughly 1 ns wide buckets mutually separated by ~ 19 ns.

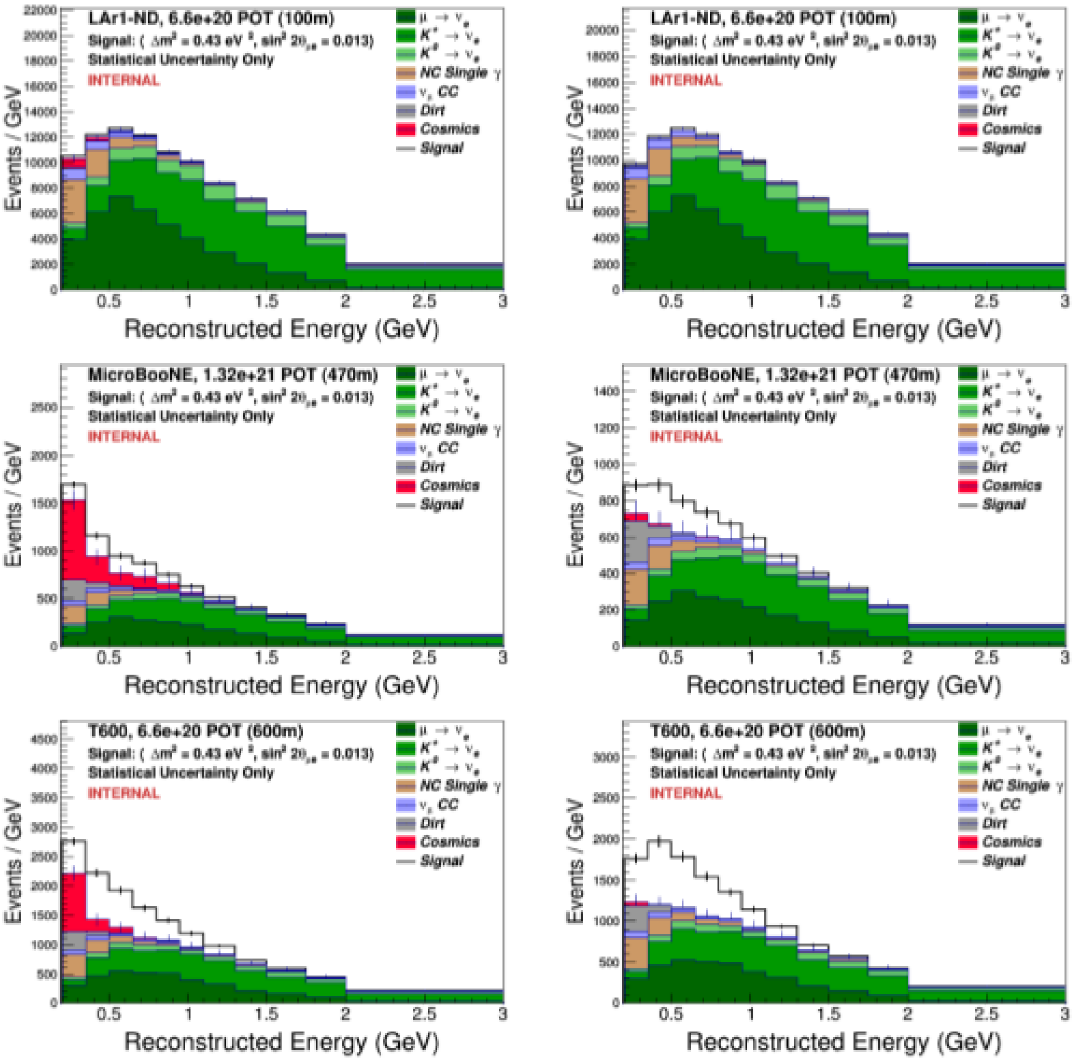

Figure 2.2: Electron neutrino Charged Current candidate distributions in LAr1-ND (top), MicroBooNE (middle), and ICARUS-T600 (bottom) as a function of reconstructed neutrino energy. All backgrounds are shown. In the left column, only muon proximity and TPC-based cuts have been used to reject cosmogenic background sources [24]. In the right column, a combination of the internal light collection systems and external cosmic tagger systems at each detector are assumed to conservatively identify 95% of the triggers with a cosmic muon in the beam spill time and those events are rejected.

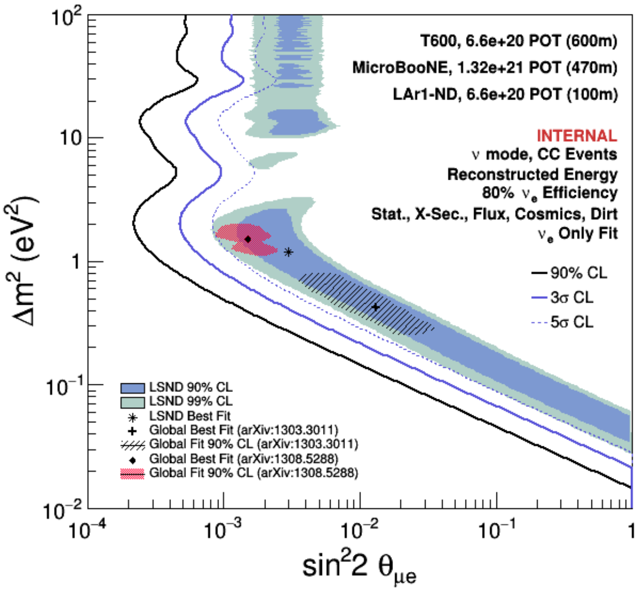

Figure 2.3: Sensitivity of the SBN program to $\nu_\mu \to \nu_e$ oscillation signals.

The composition of the flux in neutrino mode (focusing positive hadrons) is energy dependent, but is dominated by ν_μ ($\sim 93.6\%$), followed by $\overline{\nu}_\mu$ ($\sim 5.9\%$), with an intrinsic $\nu_e/\overline{\nu}_e$ contamination at the level of 0.5% at energies below 1.5 GeV (Fig. 2.4). The majority of the ν_μ flux originates from pion decay in flight ($\pi^+ \to \mu^+ + \nu_\mu$) except above $\sim 2\ GeV$ where charged kaon decay is the largest contributor. A substantial portion of the intrinsic ν_e flux, 51%, originates from the pion-muon decay chain ($\pi^+ \to \mu^+ \to e^+ + \nu_e + \nu_\mu$) with the remaining portion from K^+ and K^0 decay.

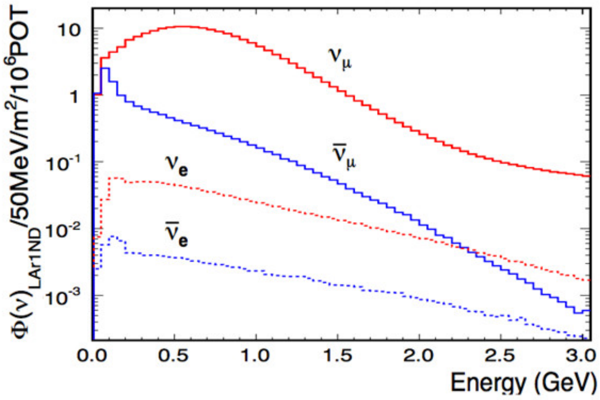

Figure 2.4: Composition of the Booster Neutrino Beam.

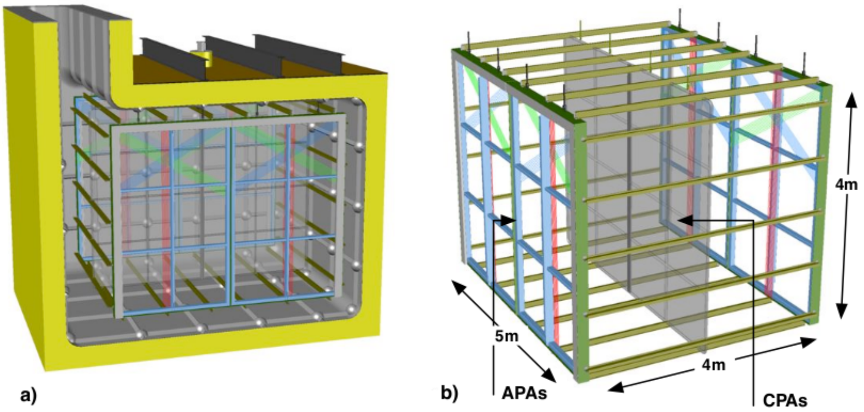

Figure 2.5: A conceptual design of the SBND (a) and a model of the TPC, showing the four bridged APAs and the central CPAs (b).

2.3 Short Baseline Near Detector (SBND)

The SBN program includes the construction of a new Short Baseline Near Detector (SBND) located at 110 *m* from the Booster neutrino source [24]. The detector is currently in the design phase and is anticipated to begin operation in 2018.
The active TPC volume will be 4.0 $m \times 4.0\ m \times 5.0\ m$, containing 112 *tons* of LAr. It will house a CPA (Cathode Plane Assembly) and four APAs (Anode Plane Assemblies) to read out ionization electron signals. The two APAs located near the beam-left and beam-right walls of the cryostat will each hold 3 planes of wires with 3 mm wire spacing. TPC signals will be read out with banks of cold electronics boards placed at the top and on the two outside edges of the frame. The total number of readout channels will be 5632 per side (11264 in the entire detector). The CPA will have the same dimensions as the APAs and it will be centred between them. It will be made of a stainless-steel framework, with an array of stainless steel sheets mounted over the frame openings. Each pair of facing CPA and APA hence will form an electron-drift region. The open sides between each APA and the CPA will be surrounded by 4 FCAs (Field Cage Assemblies), constructed from FR4 printed circuit panels with parallel copper strips, to guarantee a uniform drift field over the whole drift region. The drift distance between each APA and the CPA will be 2 *m*, such that the cathode plane will need to be biased at $-100\ kV$ to achieve the nominal 500 V/cm electric field. The SBND design will additionally include a light collection system consisting of $120 - 8$" PMTs for detecting scintillation light produced in the LAr volume. The detector will be complemented by an external cosmic ray tagging system.

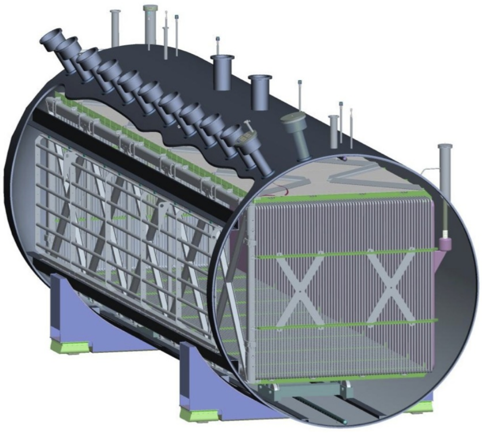

Figure 2.6: Schematic design of the MicroBooNE detector

2.4 MicroBooNE detector

The MicroBooNE detector [25] is a 170 *tons* (total volume) LAr-TPC. The TPC consists of a cathode plane on one side, a field-shaping cage around the drift perimeter and three planes of wires on the opposite end to record the signals from the drifting ionization electrons. The cathode plane is biased to a very high voltage ($\sim\ -100\ kV$) in order to create the expected electric field ($500\ V/cm$) along the TPC volume. The ionization electrons travel through this field and their signal is measured by the three wire planes. Each plane is offset by 60 degrees from the others providing the spatial reconstruction in the $y-z$ plane. If the charge arrival time is know, it is possible to determine the x component. Further timing information is provided by a 32 Photo Multiplier Tubes (PMT) array which allows to detect the prompt scintillation light produced during the excitation or ionization of argon atoms (see Par. 2.7 for details).

The MicroBooNE detector was filled with liquid argon in the summer of 2015 and it began to operate in late 2015 for an initial $\sim$ 3 years run. In 2018, MicroBooNE will continue to operate as part of the SBN program along with the other two LAr detectors.

2.5 ICARUS T600 detector

The ICARUS-T600 cryogenic detector is the biggest LAr-TPC ever realized. It consists of a large cryostat split into two identical modules and filled with about 760 *tons* of ultra-pure LAr. The pre-assembly of the ICARUS T600 detector began in 1999 in Pavia (Italy). One of its 300 *tons* modules was brought into operation in 2001. A test run lasting three months was performed with exposure to cosmic rays at sea level, allowing for the first time an extensive study of the main detector features [26]. After the test, the detector was de-

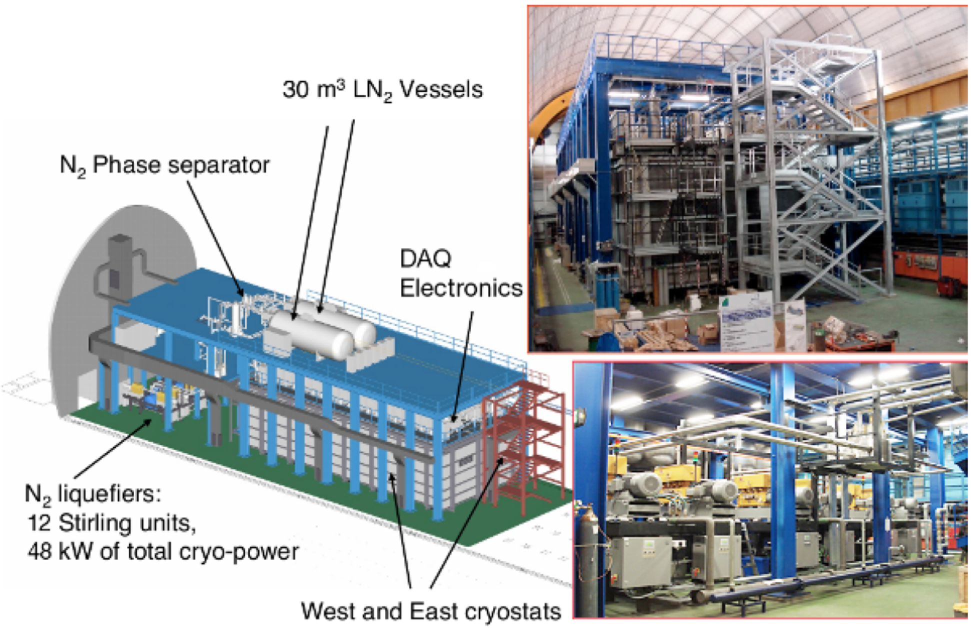

Figure 2.7: A schematic view of the whole ICARUS-T600 plant in Hall B at LNGS (left); photo of the detector installation (right-top); details of the cryo-cooler plant (right-bottom).

commissioned and, in 2004, the two cryostats housing the internal detectors were transported in the Hall B (Fig. 2.7) of the underground Gran Sasso National Laboratories (LNGS).

In the first months of 2010, the T600 finally started its operation taking data both with the CERN to Gran Sasso neutrino beam (CNGS) and cosmic rays. The ICARUS experiment has operated with a remarkable detection efficiency and it successfully completed a three years physics program being exposed to the CNGS beam from October 2010 to December 2012. Neutrino events have been collected, corresponding to 8.6×10^{19} protons on target with an efficiency exceeding 93%. Additional data were also collected with cosmic rays, to study atmospheric neutrinos.

The T600 decommissioning process started in June 2013. The two T300 modules were moved to CERN in December 2014, where a complete overhauling was done (CERN WA104 project) in view of the future shallow underground operation at FNAL.

2.5.1 T600 operation and event reconstruction

The ICARUS-T600 detector consists of two identical modules with internal dimensions $3.6 \times 3.9 \times 19.6\ m^3$ each. Each module houses two TPCs separated by a common cathode, made of punched inox sheets with 58% transparency to light. The TPC anode is made of three parallel planes of wires, 3 mm apart,

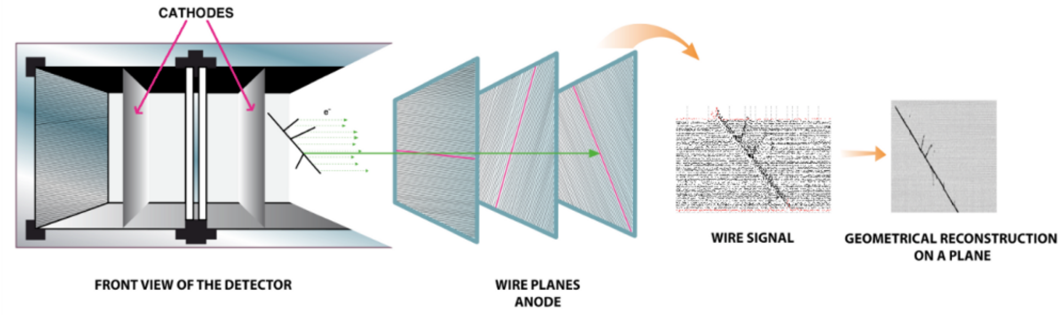

Figure 2.8: Illustration of the ICARUS-T600 operation: a charged particle ionization path in LAr and its geometrical reconstruction.

facing the 1.5 m drift path. Globally, $\sim$ 50000 wires with length up to 9 m are installed in the detector. A uniform electric field ($E_{drift} = 500\ V/cm$) perpendicular to the wire planes is established in the LAr volume of each half-module by means of a HV system in order to prevent the ion-electron recombination and to lead the drift of the ionization electrons towards the anodic wires. The HV system is completed by field-shaping electrodes to guarantee the uniformity of the field along the drift direction, and by an HV feedthrough to maintain the cathode at the required potential of 75 kV.
Charged particles, generated for example by a neutrino interaction in LAr, produce ionization along their path. Thanks to the low transverse diffusion of charge in LAr, the images of the tracks produced by ionization electron clouds are preserved and, drifting along the electric field lines, are projected onto the anodic wires (Fig. 2.8). By appropriate voltage biasing, the ionization charge induces signals in non-destructive way on the first two planes (Induction-1 and Induction-2), then it is finally collected by the last one (Collection plane).
Wires are oriented on each plane at a different angle ($0°, +60°, -60°$) with respect to the horizontal direction. Therefore, combining the wire and drift coordinates on each plane at a given drift time, a three-dimensional reconstruction of the ionizing event can be obtained. A remarkable resolution of about 1 mm^3 is uniformly achieved over the whole detector active volume.
The measurement of the absolute time of the ionizing event, combined with the electron drift velocity information ($v_{drft} \sim 1.6\ mm/\mu s$ at $E_{drift} = 500\ V/cm$), provides the absolute position of the track along the drift coordinate. The determination of the absolute time of the ionizing event is accomplished by the detection of the prompt scintillation light produced in LAr by charged particles (see Par. 2.7 for details). To this purpose, arrays of cryogenic photomultiplier tubes are installed behind the wire planes of each TPC in a dedicated sustaining structure. In the LNGS configuration, the T600 light detection system was based on the large surface Photo-Multiplier 9357FLA Electron Tube, a 12-stage dynode PMT with an hemispherical glass window 200 mm (8”) diameter, manufactured to work at cryogenic temperatures [28]. In the first T300 module only two central rows of 9 PMT were installed. Two additional PMTs

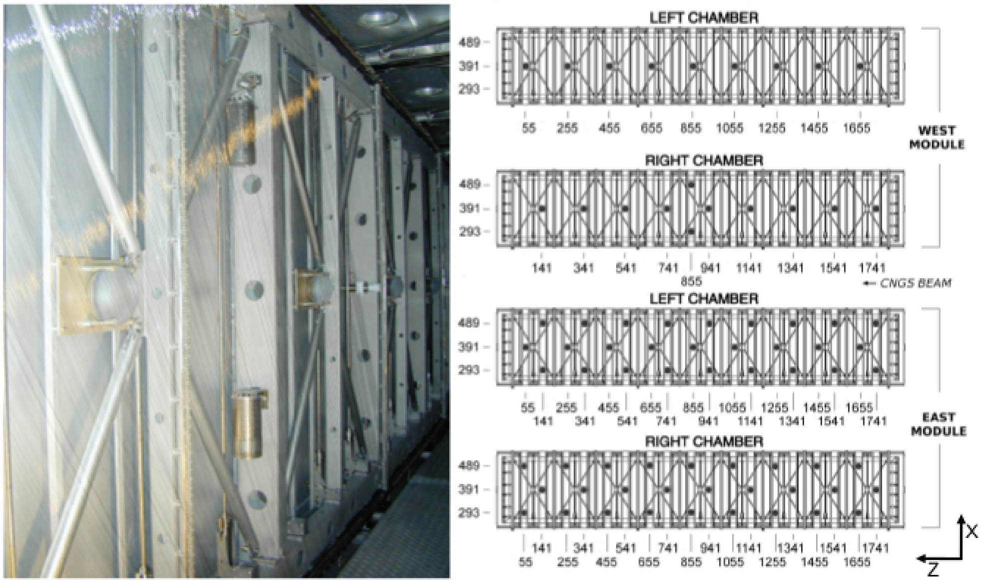

Figure 2.9: Internal view of one TPC in the LNGS configuration, with a few PMTs clearly visible together with their sustaining structure (left); PMT layout in the two ICARUS T600 modules in the LNGS configuration (right).

were placed in the top and bottom positions in the right T300 chamber at the center of the longitudinal direction, for an overall amount of 20 PMTs. In the second T300 module, three rows of 9 PMTs were installed behind each wire chamber for a total amount of 27 + 27 photomultipliers (Fig. 2.9). In the LNGS configuration, the PMT system allowed to get a 100% trigger efficiency for CNGS-induced events above 300 MeV of deposited energy, with a remarkable stability during the three years of data taking.

The electronics was designed to allow continuous read-out, digitization and independent waveform recording of signals from each wire of the TPC. The read-out chain was organized on a 32-channel modularity. A Decoupling Board was adapted to receive the signals from the chamber and to pass them onto an Analogue Board via decoupling capacitors. It was also used to provide wire biasing voltage and the distribution of the test signals. Digitization was performed by 10-bit fast ADCs, which 400 ns sampling time. The trigger was based on the detection of the scintillation light by the PMTs, which was set in coincidence with the CERN-SPS proton extraction time window for the CNGS beam, suitably delayed to take into account the propagation time of neutrinos.

2.6 The T600 refurbishment: the WA104 program

The ICARUS T600 detector was designed for the low background, deep underground conditions of LNGS laboratory (1400 meters below rock, 3800 w.e.),

where the single prompt trigger always ensured the unique timing connection to the main image of the event. However, the situation will be substantially different at FNAL, where the detector will be placed at shallow depths (a few meters deep), since several additional and uncorrelated tracks due to cosmic rays will be generally occurring continuously and at different times during the $\sim 1\ ms$ duration of the T600 readout window [26]. This fact represents a new problem to reconstruct the true neutrino-induced interaction tracks, since it is necessary to precisely associate the different timings of each element of the image to their own specific delay with respect to the trigger. The specific investigation of the oscillation anomalies in the SBN program is based on the search of a signal with the presence of a neutrino-induced, single ionizing electron (or positron). High energy cosmic muons creating secondary showers may also produce single ionizing background electrons or positrons with similar energies. At the neutrino energies of the Fermilab BNB, the intrinsic ν_e Charged Current (CC) contamination occurs at the very low rate of $\sim 500\ \nu_e(CC)/y$, while a possible LSND oscillation signal will produce a few hundred $\nu_e(CC)/y$. On the other hand, the cosmic ray background is very rich of events. Indeed, during the 1 ms duration of each readout window, ~ 11 cosmic ray tracks are expected over the full T600, according to the ICARUS measurements at surface carried out in the test run in 2001 [27].
It follows that in the LNGS configuration the T600 detector cannot perform a practical search for LSND anomalies at shallow depths, since the cosmic trigger events are too much frequent. To enables the T600 detector to operate with high-performance at shallow underground condition, the implementation of some features is required.
To this purpose, the ICARUS T600 detector was moved to CERN at the end of 2014 for a complete overhauling preserving most of the existing operational equipment while upgrading some components with an updated technology. The refurbishment, approved as *WA104* project, included the following main activities:

- the improvement of the cathodes planarity;
- the realization of new vessels for LAr containment and new thermal insulation;
- the complete review and maintenance of the cryogenics and purification systems;
- the implementation of a new readout electronics;
- the implementation of a new light collection system, to allow a more precise event localization and disentangle beam events from the background induced by cosmic rays.

The next sections will be mainly focused on this points. In particular, a full description of the studies on LAr scintillation light and conversion of VUV to visible light will be presented in the next chapters.

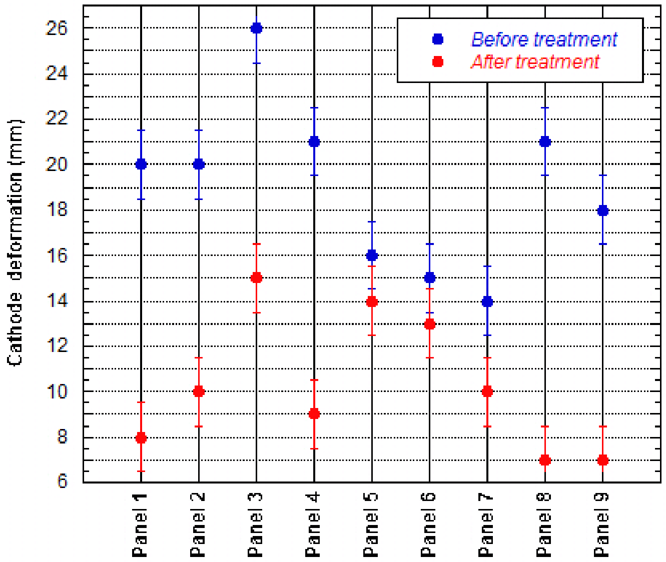

Figure 2.10: Cathode deformation for a T300 module. Deformation is shown before and after the thermal treatment for each panel.

2.6.1 Cathodes planarity

Small deviations from the uniformity of the drift field were found in LNGS data in the region close to the cathode plane on both modules. This was due to the not perfect planarity of the cathodes, owing to their pierced structure. This was confirmed by visual inspection after the first cryostat opening where displacements from planarity of the order of 25 mm were found. It was decided to restore the cathodes improving their planarity by a thermal treatment including local pressing and heating. The treatment was carried out by the CERN mechanical facility and the panels were reinstalled in the detector after a careful cleaning (electro-polished). In Fig. 2.10 is shown the cathode planarity for a T300 module measured before and after the thermal intervention. Data refer to the maximum deformation value per cathode panel (9 in total), namely the highest divergence measured between different coordinates on each panel. Results show a remarkable improvement (up to 60%) in cathode planarity proving the thermal treatment success.

2.6.2 Readout electronics

The ICARUS-T600 electronics was designed starting from an analogue low noise warm front-end amplifier (mV/pC) followed by a multiplexed (16 to 1) 10-bit AD converter and by a digital VME module that provides local storage, data compression, and trigger information. The present architecture is still efficient for the SBN search purpose. The analogue front-end amplifier, used in the T600 LNGS configuration, is perfectly adequate: the only change is the adoption of a smaller package for the BiCMOS custom dual channel amplifier.

A relevant change, in the new electronics design, concerns the adoption of serial ADCs (one per channel) in place of the multiplexed ones used at LNGS. The main advantage is the synchronous sampling time (400 ns) of all the channels of the whole detector and the compactness. A new flange (DN200CF type) has been developed for the T600 future operations. This flange allows the connection of 16 cables (512 channels), to exploit the external side of the flange as an electronics cards backplane in a special crate. The connectors on the external side allow for direct insertion of electronics boards, where both analogue and digital electronics, with a compact design, are housed. Performance, in terms of throughput of the read-out system, has been improved replacing the VME ($8-10\ MB/s$) and the sequential order single board access mode (inherent to the shared bus architecture) with a more efficient switched I/O. Such I/O transaction can be carried over low cost optical links at speed of 16 bit/s.

2.6.3 Trigger and DAQ

As mentioned above, at the nominal BNB intensity of 4.5×10^{12} pot/spill extracted in 1.6 ns time window, about one neutrino interaction every 180 spills is expected to occur in the T600 detector with vertex in the LAr-TPCs. A similar event rate, one every 210 spills, will come from beam-associated events, essentially from the muon beam halo and from interaction in the material surrounding the T600. The dominant source of events, 1 over 55 spills, is expected from cosmic rays. Globally, about 1 event every 10 s is foreseen in the T600 at the standard 5 Hz repetition rate of the BNB. According to the NuMI beam intensity of 4×10^{13} protons per pulse with 0.53 Hz repetition rate and its 8.6 ns spill duration, one trigger every 12 s is expected in the T600, mainly due to cosmic rays occurring in the coincidence gate. About one NuMI neutrino event every 150 s is also foreseen. Globally a $\sim 0.2\ Hz$ physical event rate, including the genuine neutrino interactions in LAr, beam halos and cosmic interactions inside the proton pulse time windows, is expected.

As a first stage, the trigger system of the T600 detector will exploit the coincidence of the prompt signals from the scintillation light in the TPC, recorded by the PMT system, with a beam gate window, generated in correspondence to the expected arrival time of neutrinos in the T600. At a higher level, comparison between the time information of the scintillation light signal and the Resistive Wall Monitors located along the beamline, will allow a preliminary rejection of fake triggers exploiting the fine structure of the bunched beam. Collected events can be further thinned out using the signals from a foreseen Cosmic Ray Tagger (CRT) to identify cosmic particles entering the detector. The actuation of this strategy requires a $\sim 1-2\ ns$ time resolution of the PMT and CRT systems, as well as a synchronization among all the sub-detector units at the same level.

The PMT system could also provide an initial rough event reconstruction in a second level trigger, exploiting the time-of-flight of particle between the different walls of the external CRT counters and the inner PMT system, aiming to identify the particles produced in the genuine neutrino interactions. According to the past ICARUS experience at LNGS, a second independent trigger system, based on the ionization charge deposited in the TPC, could be set starting from the recognition of a track in a TPC wire chamber. In this case, the already developed dedicated algorithm filtering the wire signals, implemented directly on the TPC read-out electronic boards, would allow to test and monitor on-line the trigger efficiency of the PMT trigger system.

2.7 The new ICARUS light collection system

2.7.1 Scintillation in Liquid Argon

Charged particles in LAr produce ionization along their path. The average number N_i of electron-ion pairs produced by a charged particle with energy E is given by the usual equation:

$$N_i = \frac{E}{W} \tag{2.1}$$

where $W = 23,6\ eV$ is obtained experimentally. Moreover, an additional effect is the production of N_e excitons. The ratio between excitons and electron-ion pairs is:

$$\frac{N_e}{N_i} \sim 0,21 \tag{2.2}$$

Therefore, the light produced by argon is composed of two different component [29]. The first one, depending on the applied electric field, is named recombination luminescence, while the second one is the so-called self-trapped exciton luminescence.
In the first case, the scintillation light is produced by the sequential process:

$$Ar^{+} + Ar \rightarrow {Ar_2}^{+}$$

$${Ar_2}^{+} + e^{-} \rightarrow Ar^{**} + Ar$$

$$Ar^{**} \rightarrow Ar^{*} + phonons$$

$$Ar^{*} + Ar \rightarrow {Ar_2}^{*} \rightarrow 2Ar + h\nu$$

when, thanks to the large cross section, the argon ions combine in a Ar_2^* *dimer* in the order of a picosecond. Instead, the exciton luminescence is produces by the process:

$$Ar^{*} + Ar \rightarrow {Ar_2}^{*}$$

$${Ar_2}^{*} \rightarrow 2Ar + h\nu$$

when the exciton and the argon combines in a dimer. For both of them, the result is the production of a photon, whose emission spectrum is peaked at $\lambda = 128\ nm$ with 5 nm of FWHM [30] [31].
Therefore, a charged particle deposits its energy in liquid argon mainly by excitation and ionization of Ar atoms, leading to scintillation light emission and free electron production, respectively. An additional scintillation light comes from the recombination of electron-ion pairs, which is inversely proportional to the strength of the electric field applied to the detector active volume. As a consequence, free-electron yield rises with the field value while photon yield decreases. In both cases saturation occurs, for minimum ionizing particles, at $E_{drift} > 10\ kV/cm$. At the nominal drift field applied in the T600, approximately the same amount of photons ($\sim 4000\ \gamma/mm$) and free electrons ($\sim$ 5000 ion-electron pairs per mm) are produced for minimum ionizing particles, according to the Birks' law:

$$\frac{dL}{dx} = S\frac{\frac{dE}{dx}}{1 + k_B\frac{dE}{dx}} \tag{2.3}$$

where L is the light yield, S is the scintillation efficiency, dE/dx is the energy loss of the particle per path length, and k_B is Birks' constant, which depends on the material.
Both of the light components, from recombination (L_r) and excitation (L_{ex}), are characterized by a double emission time scale: measurements at different field conditions show that both excitation and recombination luminescence have two different components, one *fast* component with a decay time $\tau_f \sim 6\ ns$, and a *slow* component with $\tau_s \sim 1.5\ \mu s$ [32]. This two-components light yield, which are common to many other scintillating materials, is probably due to excited molecular dimer Ar_2^* which, before decaying to the fundamental dissociate state ${}^1\Sigma_g^+$, can exist in three different states, namely two singlets (${}^1\Sigma_u^+$ and ${}^1\Sigma_u^-$) and one triplet (${}^3\Sigma_u^+$) state. The singlet state ${}^1\Sigma_u^-$ cannot decay radiatively due to parity conservation. Instead, radiative decay is possible for the remaining two states although the triplet-to-ground state transition should be in principle forbidden by the selection rule $\Delta S = 0$. This results in two different decay time, a fast component related to the singlet state decay and a slow component related to the triple states decay. This quite large difference is unique in argon among other noble gases. The relative intensity of the two fast (c_f) and slow (c_s) components depends on the energy loss density of the ionizing particle, ranging from $c_f/c_s \sim 1/3$ for a m.i.p. up to $c_f/c_s \sim 3$ for high ionizing particles such as α particles, allowing particle discrimination in some particular cases.

2.7.2 Light collection system

As already seen in the previous sections, the future operation of the ICARUS T600 at shallow depth at FNAL requires an improvement of some components of the detector with an updated technology. In particular, the improvement of the light collection system is needed to detect with full efficiency the prompt scintillation light from events with energy depositions down to $\sim 100\ MeV$ or even below.
The detection process in the LAr TPC is initialized by the trigger signal. It opens a long imaging readout window, in which particle tracks are recorded in a time sequence, collected serially by the readout planes, while the electrons uniformly move towards the end of the drift path. The full image of the event is therefore progressively generated combining the signal of all the readout wires as a function of the time. The scintillation light signal must be set in coincidence with the $1.6\ \mu s$ beam trigger gate, giving the huge rate of $\sim 0.83 \times 10^6$ coincidence per year. Moreover, during each readout window, there will be on average 44 cosmic ray-induced scintillation light signals spread over the whole T600. This number corresponds to $2 + 2$ times the number of the cosmic tracks (11 tracks) collected in a drift time according to the first ICARUS test run in 2001 [27]. The first $\times 2$ factor depends to the fact that the time interval during which a light signal can be linked to a charge deposition is twice the maximum drift time, while the second $\times 2$ factor is due to the cathode transparency that allows to collect the scintillation light produced in a TPC by the PMT of the other one. The new light collection system has to be able to localize the track associated with every light pulse along the $20\ m$ of the longitudinal detector direction, with an accuracy better than $1\ m$, which is smaller than the expected average spacing between cosmic muons in each TPC image. In this way, the light collection system would be able to provide unambiguously the absolute timing for each track and to identify the event in coincidence with the neutrino beam spill among the several tracks in the TPC. The time accuracy of the incoming event with the new light collection system is expected to be at $1\ ns$ level, allowing the exploitation of the bunched beam structure, lasting $1.15\ ns$ ($FWHM \sim 2\ ns$) every $19\ ns$, to reject cosmic events out of bunch [33]. An overall time resolution of $1.3\ ns$ would then allow a background reduction of a factor ~ 4 by rejecting cosmic events occurring outside the RF buckets with a 2σ accuracy.

2.7.3 PMT layout and selection

As seen above, to detect the scintillation light produced by argon, arrays of photomultiplier are installed behind each TPC collection wires plane. As first step, a dedicated Monte Carlo simulation was realized [34] in order to identify the best light collection system layout for the refurbished T600 detector. This simulation permitted to study the performances for different PMT con-

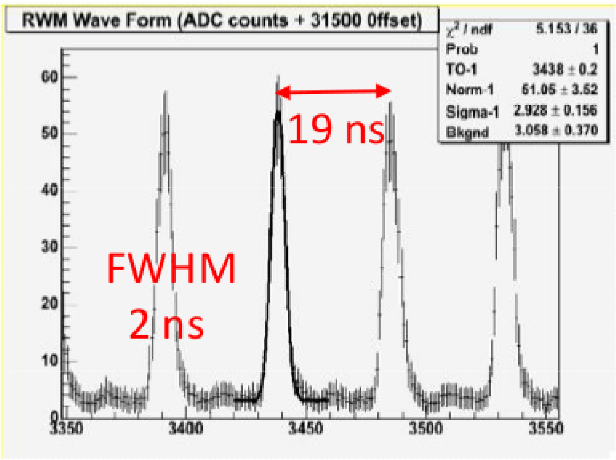

Figure 2.11: The BNB bunched beam structure.

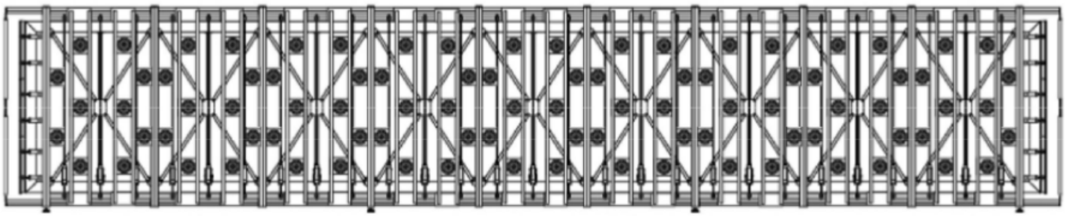

Figure 2.12: Scheme of the PMTs disposition on each T600 TPC.

figurations, in order to select the most suited for the experiment purposes. However, the different PMT dispositions were based on the already existing mechanical structure of the T600. In fact, the basic idea was to exploit the free space available in the mechanical structure without change it. Moreover, two different diameters for the PMTs window (5 *in* and 8 *in*) were considered. Simulation results showed the highest precise position reconstruction in geometries with higher numbers of PMTs. Moreover, better results in localization capability were obtained considering a 90×8 *in* PMTs configuration instead of a 210×5 *in*. Thus, the layout with 90×8 *in* PMTs for each TPC, involving a total of 360 PMTs (Fig. 2.12) turned out to be the most suitable. However, to obtain the light detection performances described above, PMTs should present good properties in terms of cathode response uniformity, signal linearity and temporal response. To this purpose, a set of tests were carried out [35] in order to choose the most suitable PMT model among the three large area PMT models available. Given the results of the tests, the Hamamatsu R5912-MOD PMT model was chosen. It is a 10 dynode-stage photomultiplier with an 8 *in* hemispherical Bialkali photocathode and it presents the following characteristics:

- a window of 8 *in* diameter and a length fitting the ICARUS mechanical structure;

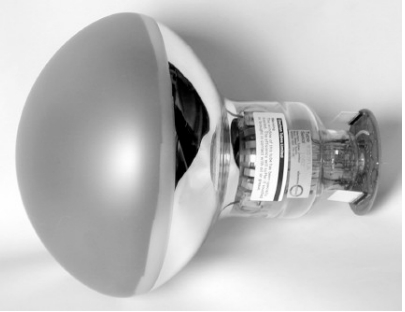

Figure 2.13: Picture of a Hamamatsu R5912-MOD photomultiplier.

- a Quantum Efficiency (QE) peak of 17% at 420 nm;
- a photocathode uniformity within 10% till 10 cm from the centre of the window;
- a gain of 10^7 with $\sim 1500\ V$ applied voltage at $T = 300\ K$;
- a Single Electron Response (SER) peak clearly visible (peak-to-valley ratio > 2) both in charge and in voltage measurements;
- a response linearity up to $\sim 300\ phe$;
- a typical dark count rate lower than 4 kHz (after 15 hours storage in darkness);
- a global Transit Time Spread (TTS) $< 2.4\ ns$.

Moreover, the Bialkali photocathode is deposited on a Pt under-layer in order to extend the range of the operating temperature down to about $-200°C$. Each PMT was provided with a proper voltage-divider circuit. This supplies the high voltage for the grids, dynodes, and anode, and allows the signal to be picked up directly from the anode. The voltage divider chain is entirely passive, and is fabricated with SMD resistors and capacitors, which were all previously tested at cryogenic temperature. The circuits were directly welded on the PMT flying leads. Since a negative power supply is adopted, two independent coaxial cables are used to provide the PMT with the high voltage and to read out the anode signal.

2.7.4 PMTs characterization

A set of tests were done at CERN laboratories in order to evaluate the performance of the PMTs (400 PMTs were purchased and sent to CERN) and their conformity to the requested feature before mounting them in the TPC [36]. Measurements at room temperature were carried out on all the PMTs. Additionally, most of the measures were repeated on 60 of them at cryogenic temperature in order to evaluate any parameter variation which could affect the scintillation light detection.

A dark-room was arranged to test simultaneously up to 16 PMTs at warm condition. A laser diode was used to produce fast light pulses at 405 nm and ~ 1 kHz repetition rate. The light intensity was set through calibrated optical filters mounted on dedicated supports, allowing different attenuation factors (ranging from $1 \div 1000$). The light was issued on the PMT windows by means of 100 μm multimode optical fibers.

The characterization at warm temperature was performed using a standard electronics set-up in which the PMT output was integrated over 50 μs by means of a CANBERRA 2005 charge preamplifier and shaped (> 500 ns) by means of an ORTEC 570 amplifier. The output signal was then recorded by a CAEN multichannel analyzer.

Tests at cryogenic temperature were performed in a different facility. In order to obtain experimental conditions similar to those in the real apparatus, PMTs were directly immersed in liquid argon inside a big dewar (1 m $diameter$ $\times$ 1.5 m $height$), allowing the simultaneous bath of 10 PMTs. The internal illumination was achieved by means of a single 100 μm multimode optical fiber. The same set-up and acquisition system described previously was used, with the fiber and the cables allowed to enter by a proper feed-through, used to preserve darkness conditions and thermal insulation.

Single Electron Response (SER) and gain

Shapes of the PMT anode pulses under single photoelectron illumination were recorded by connecting directly the anode output to the 50 Ω input of a 1 GHz bandwidth oscilloscope. Measurements were carried out both at room and at cryogenic temperature, and setting the photomultiplier gain at $G \approx 10^7$. No significant variation were observed between room and cryogenic temperature. The resulting mean values are: a leading edge of 3.9 ± 1.1 ns, a FWHM of 5.6 ± 1.1 ns and a trailing edge of 10.3 ± 1.6 ns.

The SER, namely the charge distribution of the PMT pulses integrated over the whole signal pulse shape, is directly related to the PMT multiplication processes and can be affected by the operating temperature. SER studies were performed by measuring the charge distribution of the PMT pulses induced by single-electron excitation at different power supply voltages. The charge distributions (Fig. 2.14) are characterized by peak profiles which features a good charge resolution. Data were fitted by means of an analytical expression. It consists in the sum of an exponential distribution, which takes into account the PMT dark-counts and the electronic noise, and few Gaussian functions which consider the response of the PMT to different photoelectrons.

The parameter constraints:

$$X_n = nX_1; \qquad \sigma_n = \sigma_1\sqrt{n}; \qquad A_n = \frac{\mu}{n}\, A_{n-1}$$

were used, where X_n is the mean of the n^{th} Gaussian curve with width σ_n and

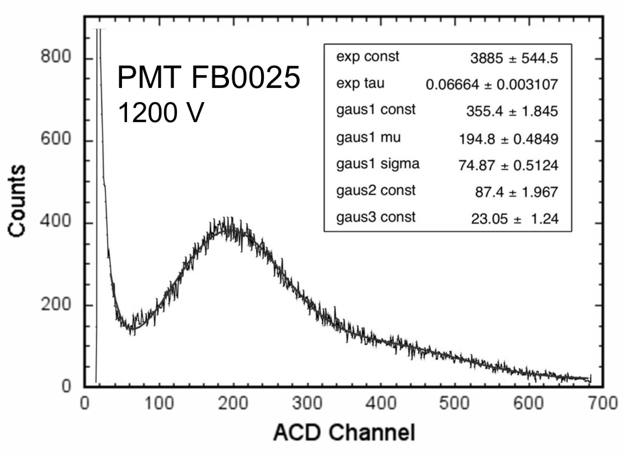

Figure 2.14: Example of charge distribution for anode signals under single-photon illumination (SER). The result of the fit, using the analytical expression described in the text, is also shown.

amplitude A_n. The value of the μ parameter, resulting from the fit, represents the mean number of detected photoelectrons. The position X_1 of the first peak allows the evaluation of the gain G. The gain dependence on the power supply applied to the PMT were measured by changing the HV setting in a range $G = 10^6 \div 5 \times 10^7$.

The PMT nominal voltage was defined as the power supply value to attain a nominal gain $G = 10^7$. The nominal voltage distribution for the whole set of 400 units operating at room temperature is shown in Fig. 2.15. The distribution is characterized by a quite narrow spread with mean value set at $V = 1390\ V$ and $\sigma = 103\ V$.

In Fig. 2.16 the results obtained at room and at cryogenic temperatures, using the same PMT, are showed. The signal amplitude is well fitted by a power law distribution as a function of the anode voltage for both temperatures.

The distribution of the relative gain variation between room and cryogenic temperature, for the whole set of 60 devices tested in both conditions, is plotted in Fig. 2.17. It may be noted that almost all the tested PMTs suffered a gain reduction at cryogenic temperature. Considering a nominal gain $G = 10^7$ at room temperature, the PMTs showed wide variations of gain losses at cryogenic temperature, down to 10%.

The distribution of the voltages to attain a gain $G = 10^7$ is shown in Fig. 2.18 for both temperatures. An increase of about 150 V of the anode voltage was always enough to recover the original gain factor.

The resolution of the SER peak, or relative variance to the peak is defined as the ratio $\sqrt{s_1} = \sigma_1/X_1$. The mean results obtained with the PMTs under test operating at a multiplier gain $G = 10^7$ are:

$$\sqrt{s}_1 = 0.35 \pm 0.03 \qquad T = 300\ K$$

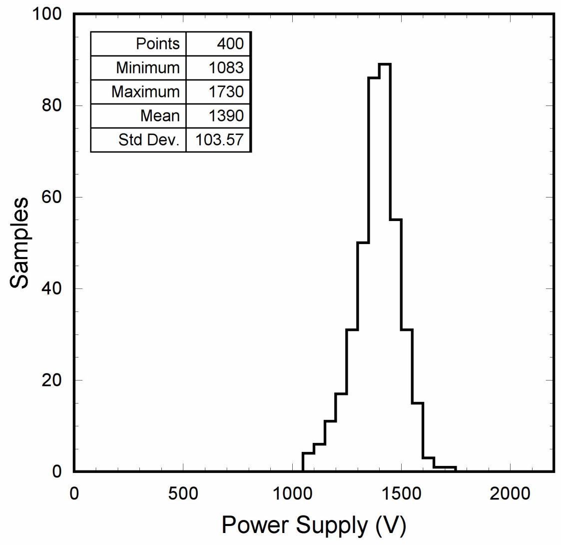

Figure 2.15: Distribution of voltages to attain a nominal gain $G = 10^7$ for the whole set of 400 PMTs operating at room temperature.

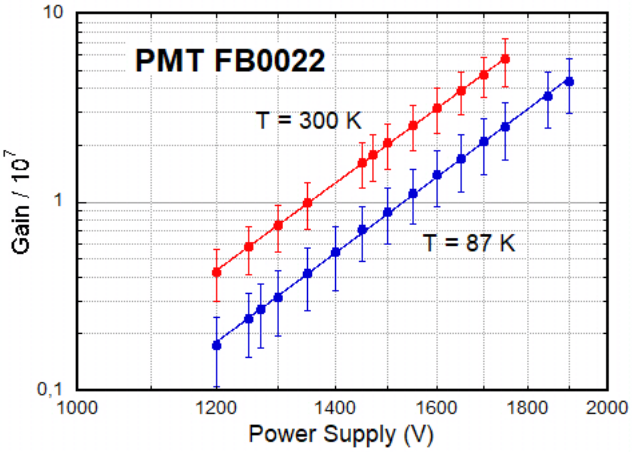

Figure 2.16: Signal amplitude (Gain) as a function of the anode voltage at room and at cryogenic temperature. For each measurement the peak position (dots) and the SER distribution width (vertical bars) coming from the fit are shown.

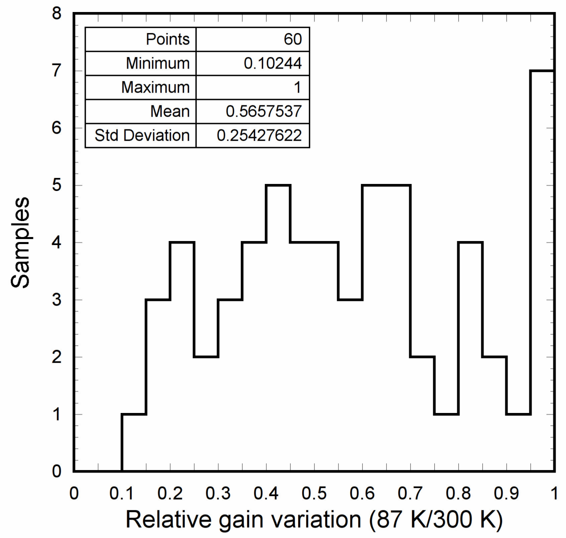

Figure 2.17: Relative gain variation between room and cryogenic temperature of the 60 tested PMTs. Results are referred to a power supply consistent with a gain $G = 10^7$ at room temperature

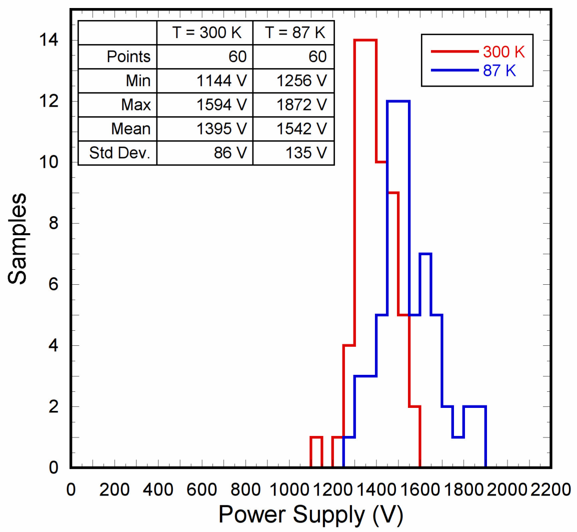

Figure 2.18: Peak-to-valley ratio (P/V) distributions at room and at cryogenic temperature of the 60 tested PMTs.

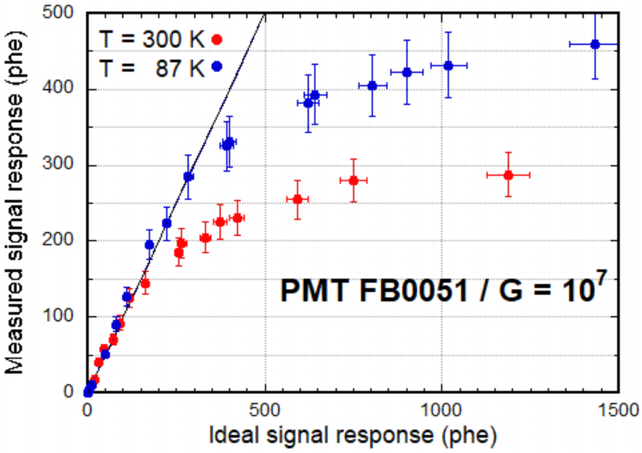

Figure 2.19: Measured PMT signal as a function of the ideal one at room and at cryogenic temperature. The horizontal and vertical bars represent the measurement error induced by the spread of the light source and by the attenuation factor uncertainty.

$$\sqrt{s_1} = 0.46 \pm 0.11 \qquad T = 87\ K$$

These values demonstrate the good performance in term of SER charge resolution at both temperatures, with a slight worsening at 87 K.

Response linearity and saturation

The response linearity was estimated in pulse mode by using a set of neutral density filters mounted in a rotating support located between the light source and the optical fiber light guides. Taking into account the attenuation factor of the filters, it was possible to vary the light intensity on the photocathode by three orders of magnitude. The gain of the PMT under test was set to $G = 10^7$ at both room and cryogenic temperature. As a first step, the output charge distribution were measured using the maximum feasible attenuation factor. The output charge distribution was then acquired increasing the light intensity. The corresponding mean number of detected photoelectrons was evaluated for each filter. This quantity, the so-called *measured signal response*, was plotted as a function of the number of injected photoelectrons (*ideal signal response*) according to the filters light attenuation factor (Fig. 2.19). The test was performed on the same PMT under test at warm and cryogenic temperature. The results demonstrate a good response linearity up to 300 photoelectrons both at warm and cryogenic temperature.

Dark counts

The dark counts are defined as the response of a PMT in absence of light. The dark rate was evaluated at warm and cryogenic temperature by measuring the rate of the PMT pulses, operating in darkness condition, above the

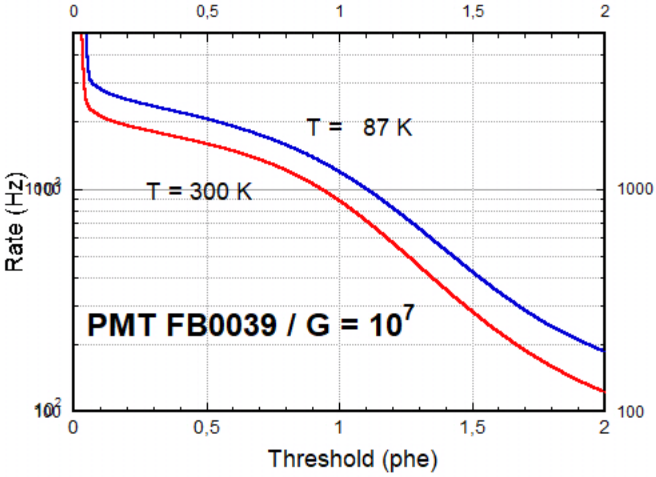

Figure 2.20: PMT dark count rate as a function of the discrimination threshold at room and at cryogenic temperature. The threshold valued is normalized to fraction of photoelectron (phe).

minimum value on the left of the SER peak. The increase of dark rate at low temperatures is a well known effect, even if not yet completely clarified, referred as Non-Thermal Dark Rate [37]. To avoid Cherenkov emission and liquid argon radiation, the precise evaluation of the dark count rate at cryogenic temperature was done on few PMTs only. The device under test was inserted into a stainless steel vacuum chamber which was set in a liquid argon bath during the cryogenic measurement. An example of count rates, as a function of the discrimination threshold and for the two different operating temperatures is shown in Fig. 2.20. The curves were acquired at a multiplier gain $G \approx 10^7$. The spectrum structure is characterized by a clear bump profile centered around the first photoelectron region, mainly due to the cathode dark noise. An increase of the counting rate at cryogenic temperature, up to a factor 1.5, was observed for all the tested PMTs.

Photocathode uniformity

The evaluation of the photocathode uniformity, which includes the photocathodic sensitivity and the focusing stage efficiency, required a dedicated experimental set-up and it was carried out at room temperature for few PMT samples only. The PMTs were operated as photodiodes. To do that, all the dynodes and the anode were tied together as a single electrode collecting the photoelectrons emitted by the cathode, which was kept at a negative voltage of $\sim 300\ V$. The PMT under test was illuminated by means of an optical fiber. A proper support was used to maintain the fiber in a fixed orientation, normal to the PMT window, allowing in the meantime to move the fiber in various positions on the window. The position was coded by the angle along the window surface with respect to the center of curvature. A laser, generating photons

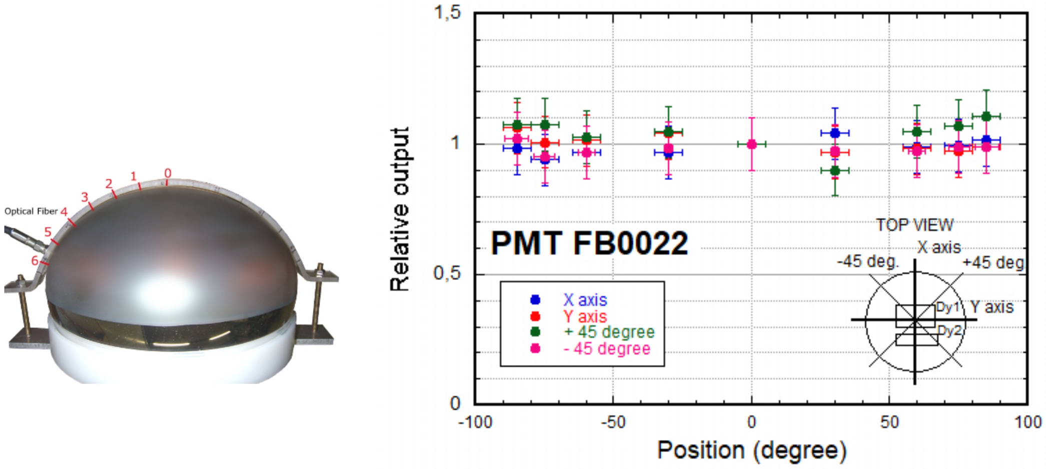

Figure 2.21: Schematic design of the dedicated fiber support (left). Response distribution for illumination of different positions on the photocathode. Values are normalized to the central position (right).

at $\lambda = 532\ nm$, was used as continuous light source. In order to monitor the illumination intensity and its stability, the light was split in two branches, one of which was sent to a photometer used as reference. The cathodic current, of the order of $10\ \mu A$, was directly measured by a picoammeter. All the tested PMTs show a good uniformity, within 10%, all over the measured surface. An example of this measure is shown in Fig. 2.21.

Transit time and spread

The measure of the PMT transit time also required a dedicated experimental set-up, so it was measured at room temperature, only. The timing spread, due to the different position of photon arrival on the cathode surface and the effects of the Earth magnetic field, was also evaluated. A pulsed laser diode ($\lambda = 405\ nm$) was used as the light source. The light pulse width ($120\ ps$ FWHM) and the repetition rate ($1\ kHz$) were regulated by a pulse generator. The light produced by the laser was split toward a fast calibrated photodiode and the PMT under test. Two optical fibers allowed the light focusing on the two devices. The light intensity was set at the PMT single-photon illumination conditions. Signals, coming from both the PMT and the photodiode, were acquired, in common trigger mode, by a $10\ GS/s$ oscilloscope (LeCroy WaveRunner 104MXI). The transit time of the PMT was evaluated as the difference between the reference times of the two signals, taking into account the delay due to the cables.
The optical fiber was positioned in a fixed orientation, normal to the PMT window, by using the same dedicated support described for the photocathode uniformity. Measurements were performed by repositioning the fiber on the window. The position was coded by the angle along the window surface with

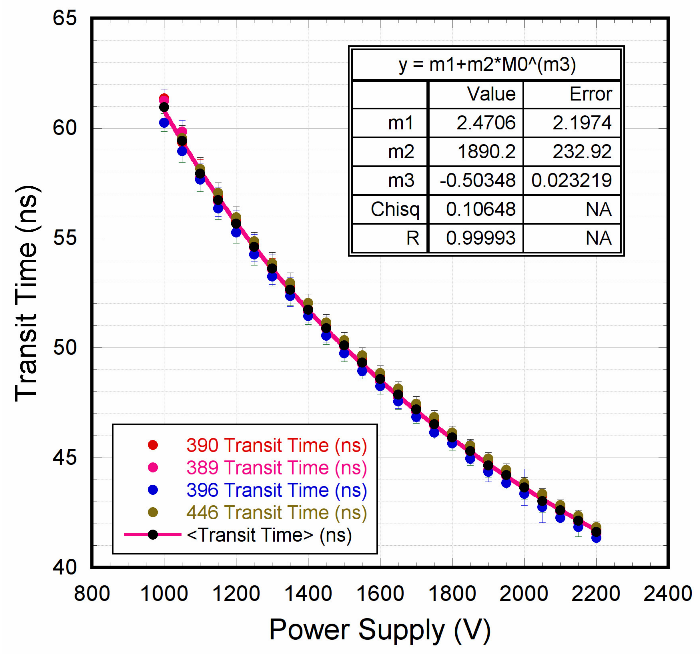

y = m1+m2*M0^(m3)

	Value	Error
m1	2.4706	2.1974
m2	1890.2	232.92
m3	-0.50348	0.023219
Chisq	0.10648	NA
R	0.99993	NA

Figure 2.22: Dependence of the transit time mean value as a function of the power supply for few PMT samples.

respect to the center of curvature. The effect due to the Earth magnetic field was also evaluated varying the PMT orientation.
In Fig. 2.22 is shown an example of distribution of the absolute transit time and the mean value as a function of the supply voltage, for some PMT units. Results are consistent with the assumption that the transit time improves in inverse proportion to the square root of the supply voltage. Differences among the various samples are between ±0.5 ns. No noticeable effect was observed varying the PMT orientation with respect to the Earth magnetic field.

2.8 Conclusions

All the 400 Hamamatsu R5912-MOD PMTs were tested at room temperature, 60 of them were also tested at cryogenic temperature. The main results can be summarized as:

- the SER parameters are in good agreement with the producer nominal values, both at room and at cryogenic temperature, with a gain decrease down to 20% in liquid argon;
- the response linearity is good all over the photocathode surface;
- the response linearity and saturation are good both at room and at cryogenic temperature;

- the transit time and the transit time spread are in good agreement with the manufacturer nominal values;
- the dark count rate is in agreement with the producer values, with an increase until a factor 2 at cryogenic temperature.

All the tested PMTs were then rated as compliant with the requirements for installation in the T600.

CHAPTER 3

THE WAVELENGTH SHIFTERS AND THE EVAPORATION PROCESS

As seen before, the ICARUS light collection system, such as in most LAr detectors, is essential for generating a light-based trigger signal and identifying the time of occurrence of each interaction particle with high temporal precision. To this purpose, photomultiplier tube model and placement have been selected in order to satisfy the main light collection system requirement as a high detection coverage, granularity and fast response. However, a further requirement was not yet considered. The PMT photocathode is sensitive to visible light with a peak at $\lambda = 400 - 420\ nm$ wavelength, whereas the LAr scintillation light is emitted at $\lambda = 128\ nm$. The most efficient way to detect the scintillation light is to shift photons to the longer wavelengths where the PMT photocatode is sensitive. *Tetra-Phenyl-Butadiene* (TPB) is the most common wavelength shifter used in LAr experiments. It is an organic fluorescent chemical compound which emits blue light with an emission spectrum peaked at 430 nm wavelength. Generally, a thin layer of TPB is deposited on the external surfaces of the light detectors (such as PMT or SiPM) or some inner surfaces of the whole detector.

3.1 Wavelength shifters

Wavelength shifters (WLS) are largely used in physics experiments in which scintillator detectors are involved, as in particle and dark matter research. Indeed, the most important parameter limiting the sensitivity in these detectors

is the light collection efficiency, which determines the achievable energy threshold and the discriminatory power. Since in most detectors the scintillation light is in the UV region, several problems can arise in achieving a good collection efficiency due to the low UV sensitivity of some light detection devices.
Some aromatic organic compounds emits fluorescence light when their Π-orbital electrons are excited, either by ionizing particles or UV radiation [38]. Electrons excited to the vibrational states of the first excited state (S_1) relax within few picoseconds to the lowest lying level of S_1, before decaying to the ground state with the radiation of a photon at the compound characteristic emission wavelength. In plastic scintillators, the binder in which the WLS is dissolved, must also have a Π-electron structure, and absorbs the incident energy. If the concentration of the wavelength shifting solute is high enough, this energy is transferred by non-radiative dipole-dipole interactions to its excited levels producing fluorescence. The transfer is efficient if there is good overlap between the binder emission spectrum and the absorption spectrum of the solute. Energy transfer to further solutes is possible, allowing the final light to be shifted to even longer wavelengths. Traditionally the WLS can be applied directly to crystal faces, target vessel walls or the front face of light-guides or photomultiplier tubes. It is possible to set the final emission wavelength of the shifter corresponding to the detector optimum sensitivity either by selecting a single suitable compound or by adding a secondary shifter to further increase the final wavelength of the light.

TetraPhenyl-Butadiene

1,1,4,4-Tetraphenyl-1,3-butadiene (TPB) is an organic chemical compound generally used as wavelength shifter in many experiments, in particular involving LAr detectors, due to its extremely high efficiency to convert VUV into visible photons. TPB chemical formula is $(C_6H_5)_2C = CHCH = C(C_6H_5)_2$ and it looks composed of white to yellow-white needles. TPB absorbs light across a broad wavelength range, from the high UV to its emission peak, which lies at approximately $425 \pm 50\ nm$. Scintillation-grade TPB, which is used in LAr experiments, has an assay of $> 99\%$ purity. As seen, the most common method to use TPB is to cover some section of the detector on the base of the scintillation light collection features and operation. To obtain TPB layers, different procedures can be used. Evaporation and sputtering are the most common ways to obtain thin film deposition. Evaporation may be done by using a resistive heater or an electron beam heater.
In ICARUS at LNGS, the TPB layer was obtained by spraying a solution of TPB and toluene (C_7H_8 on the surface of each PMT [39]. The result was a non-uniform coated surface where some spots, corresponding to the material release point, were visible. However, the coating was good enough for the experiment purposes.
In the SBN program, an improvement of this technique is needed, both for the complexity in using the toluene (it is extremely harmful to health) and for ob-

taining a more uniform wavelength shifting on all the PMTs surfaces. For that reason, the spray technique was replaced by the *evaporation process*, which allows to easier act on the coating parameter as the thickness, the quality and the uniformity of the layer.

3.2 The evaporation process

Evaporation is a non-equilibrium process in which there is a net transport of liquid molecules across a liquid−vapour interface into the vapour phase. In chemistry, the evaporation rate is described by the Hertz–Knudsen equation:

$$\frac{1}{A}\frac{dN}{dt} = \frac{\alpha(P^* - P)}{\sqrt{2\pi m k_B T}} \tag{3.1}$$

where A is the area of the evaporating surface, N is the number of gas molecules, α is the sticking coefficient of the gas molecules onto the surface $(0 \leq \alpha \leq 1)$, P^* is the partial pressure of the gas in equilibrium with its condensed phase at a given temperature, P is the ambient hydrostatic pressure acting upon the evaporant in the condensed phase, m is the molecular mass, k_B is the Boltzmann constant and T is the temperature [40]. A first formulation were done by Hertz which found experimentally that the evaporation rate was proportional to $(P^* - P)$. This is consistent with the kinetic theory in which the impingement rates are proportional to pressure. Hertz also found that the evaporation rate could not be increased by supplying more heat unless the equilibrium vapour pressure was also increased by this action. Hereafter, Knudsen postulated that the evaporant vapour molecules impinging upon the condensed phase surface may be reflected back, adding the α coefficient to the Hertz equation. However in 1909, Knudsen invented a technique to force α to 1. He built a so-called *Knudsen cell* (K-cell) or effusion cell. It is composed by an orifice containing a crucible surrounded by an heating filament. K-cell utilises the principle of molecular effusion (also demonstrated by Knudsen in 1909). Material to be deposited is heated to a suitable vapour pressure in a isothermal enclosure with an aperture in its wall. Molecular effusion occurs when the mean free path is large compared with the dimensions of the aperture. This gives rise to a cosine intensity distribution which can be collimated to form a beam of electrically neutral material. In this case, the orifice acts like an evaporating surface of area A at P^* but it cannot reflect incident vapour molecules, so $\alpha = 1$. Then, using a K-cell, the only two variables of the evaporation process are the pressure P and the temperature T.

The basic idea then, is to place the PMT in front of a K-cell filled with the TPB. In that way, TPB vapour coming out from the cell lid aperture hits the cooler PMT surface condensating in a thin uniform film. The evaporation system was set-up restoring a pre-existent thermal evaporator, consisting in a vacuum chamber housing two K-cells. However, this system was used for different PMT models with different size. An additional study on the evaporation

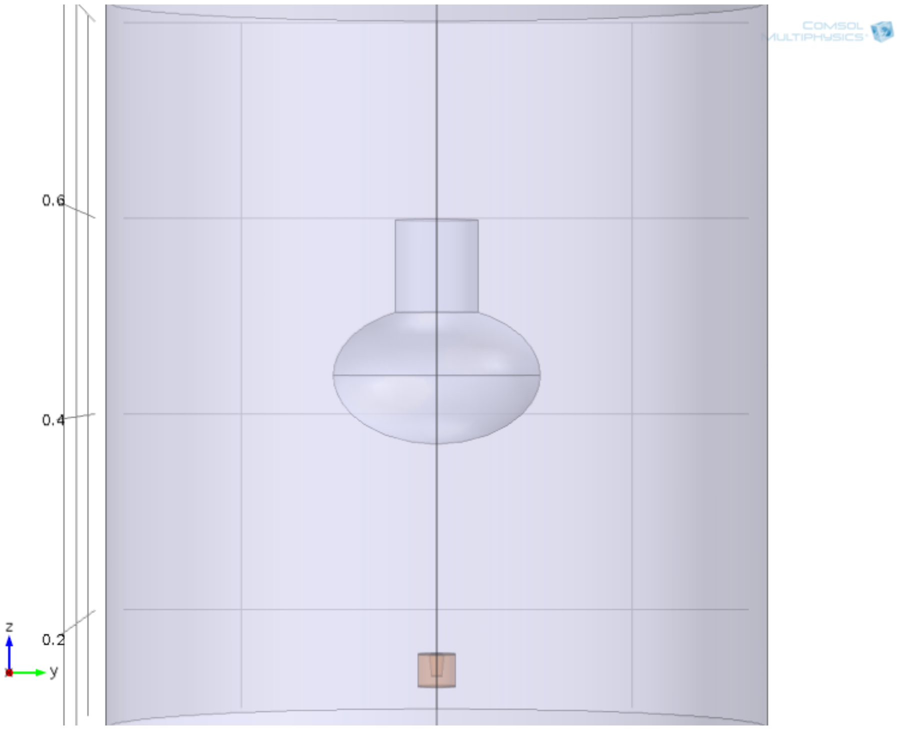

Figure 3.1: Design of the internal structure of the evaporation chamber simulated by COMSOL®.

geometry with the 8 in. PMTs was then required.

3.3 System geometry and simulation

Before starting the assembly of the thermal evaporator, some geometrical studies were done by using the software platform *COMSOL multiphysics*®[41]. It is a cross-platform finite element analysis simulation software, based on advanced numerical methods for modelling and simulating physics-based problems. With COMSOL® it was possible to develop a possible internal structure of the evaporator in order to obtain some basic informations correlated to the geometry of the evaporation process.

The designed evaporator internal structure is shown in Fig. 3.1. The PMT is placed above the the K-cell at 30 *cm* distance. This distance between the K-cell and the PMT is determined by the vacuum chamber size which is in turn related to the vacuum system (see the next section for details).

To simulate the evaporation process, the pre-defined COMSOL® *particle tracing* time-dependent model has been used. Particles, having mass and dimension of the TPB molecules, were isotropically generated within a semisphere from the bottom of the crucible (assumed to be the TPB source) placed inside the K-cell. The internal walls of the crucible were defined with the *bouncing* property. In this way, it was possible to reproduce the rebound of the

PMT orientation angle	Fraction of deposited TPB
0°	$(42.6 \pm 0.2)\ 10^{-3}$
10°	$(44.4 \pm 0.2)\ 10^{-3}$
20°	$(45.5 \pm 0.2)\ 10^{-3}$
30°	$(51.1 \pm 0.2)\ 10^{-3}$
40°	$(50.7 \pm 0.2)\ 10^{-3}$

Table 3.1: Ratio of the deposited TPB on the PMT surface at different orientation angles.

warm TPB molecules inside the crucible until their trajectories matches with the direction of the lid hole. The particle tracing outside the K-cell has been simplified by considering no interaction between particles after they leave the crucible. The PMT sensitive surface were defined by using the *freeze* option, in order to make available the whole kinematics of each particle impinging on this surface. This allows to determine the ratio between the number of TPB particles hitting the PMT surfaces and the total number of particles emitted by the K-cell.

From previous measurements [39], it was possible to assume an average TPB density value of $\sim 0.2\ mg/cm^2$ as enough to have a sufficient VUV photons conversion. A first evaluation was then to estimate if the designed internal geometry of the evaporation system is suitable to achieve this average density value. This estimation was done at different angles of inclination of the PMT with respect to the evaporator axis. In Tab. 3.1, the ratio of the deposited TPB on the PMT surface to the total evaporated quantity is reported for different orientation angles.

The quantity of deposited TPB slightly increase with the PMT inclination, probably due to geometrical effect.

The PMT sensitive surface is:

$$S = \pi r^2 = 320\ cm^2$$

Considering for examples the 40° degrees orientation angle, the quantity of the TPB needed to achieve the $\sim 0.2\ mg/cm^2$ reference density is given by:

$$\frac{0.2\ mg/cm^2 \times S}{Ratio_{40^\circ}} = 1.26\ g_{TPB}$$

which is sufficiently comparable with other experimental tests [42]. This type of internal configuration then, seems to be fine from the point of view of the quantity of TPB deposited on the PMT.

A further geometrical consideration regards the uniformity of the deposited layer, which mainly depends on the orientation of the PMT. In principle, the best PMT orientation would be at 0° angle, namely with the PMT axis aligned to the evaporator axis. In this configuration, the TPB would cover the whole center of the PMT window with a good uniformity. However, in this configuration, only a small fraction of TPB would reach the edge of the PMT sensitive window, which results totally uncovered far away from the center, as showed in Fig. 3.2 a). Another possible arrangement is with the PMT inclined at a certain angle with respect to the evaporator axis. In this configuration, the TPB would cover with a good uniformity the portion of the PMT sensitive window which look at the K-cell, leaving however the rest of the window almost totally uncoated, as showed in Fig. 3.2 b). For example, the resulting TPB density distribution for the PMT oriented at 40° angle is displayed in Fig. 3.3 (*left*), showing the almost total absence of TPB in most of the PMT window.

This issue can be solved by slowly rotating the PMT on its own axis during the evaporation process. In this way, the TPB coating should be well distributed all over the sensitive window. The effect of the PMT rotation on the evaporation process has been simulated by integrating the COMSOL® analysis with a user-written code which allows to rotate the coordinates of the TPB particle hitting the PMT window in the x-y plane.

In Fig. 3.3 (*right*), the resulting TPB particles distribution on the PMT window is shown for the PMT oriented at 40° taking into account the rotation on its own axis. TPB particles result well distributed all over the PMT window with a good regularity, confirming this last configuration as a good solution in terms of coating uniformity. This possible arrangement has been examined by comparing the TPB distribution for different PMT orientation angles in order to find the optimized configuration. To this purpose, the TPB particle distribution has been studied as a function of the radial distance from the PMT window center for the PMT oriented from 0° to 50° angles with a 10° step. In Fig. 3.4, the resulting distribution of the TPB particles is shown. As suggested above, in the 0° configuration (black curve), the TPB is well distributed around the center of the PMT sensitive window but it sharply drops to zero far away from the center. Moving towards the 40° orientation, the TPB density in the window center decreases but the TPB tends to be uniformly distributed all over the PMT window. At 50° orientation, TPB starts to be deposited more on the border than on the center of the sensitive window (blue curve).

The 40° PMT configuration then, seems to be finally the best solution from the point of view of the uniformity of the TPB coating. For this reason, the evaporation system was set-up by fixing the PMT inclined of 40° angle, on the basis of this result.

3.4 Evaporation system specification

To perform TPB evaporation on the PMTs, a thermal evaporator, consisting of a cylindrical vacuum chamber of 68 *cm* high and 64 *cm* diameter, was set up restoring a pre-existent thermal evaporation. As seen above, the basic idea is to place the PMT in front of a K-cell filled with the TPB. In that way,

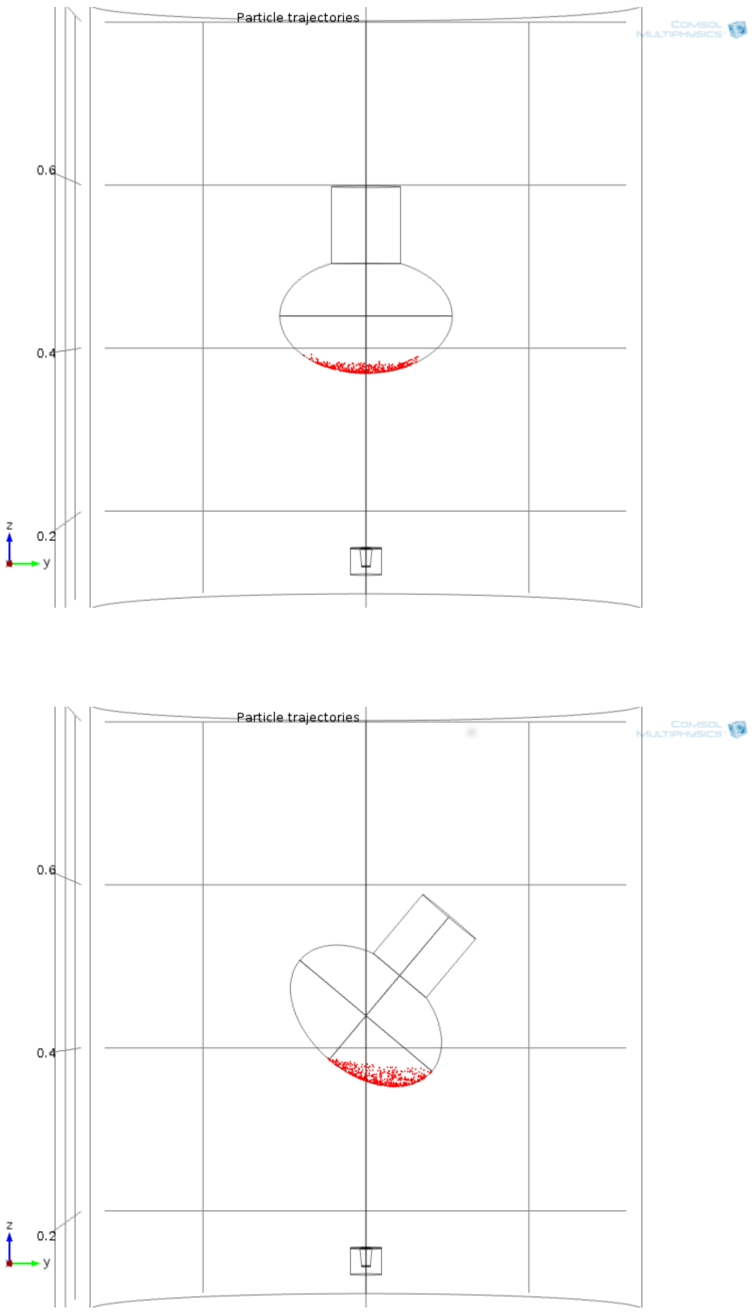

a)

b)

Figure 3.2: Graphical view of the results obtained from the COMSOL® particle tracing simulation. Figure shows the TPB particles distribution on the PMT sensitive window for the PMT at 0° orientation angle a) and for the PMT at 40° orientation angle b).

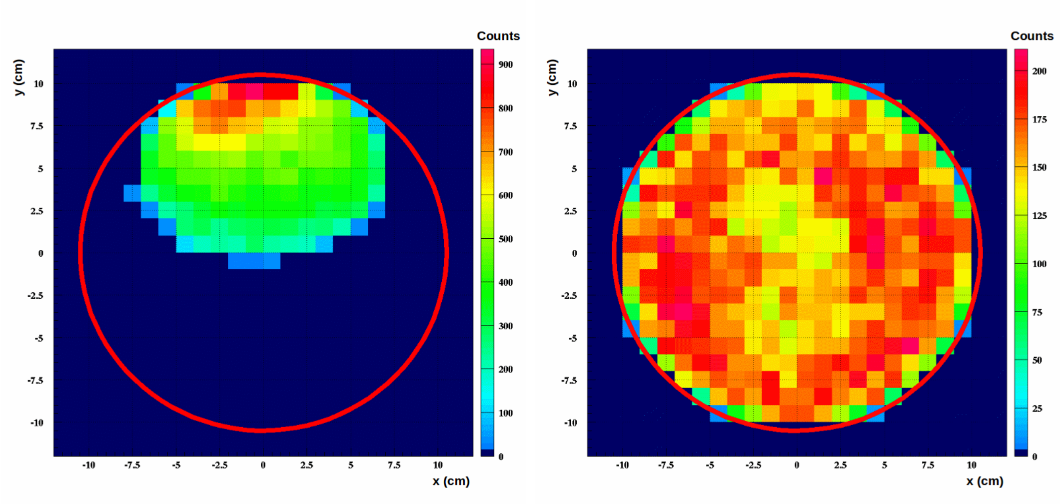

Figure 3.3: Graphical plots of the TPB particle distribution on the PMT sensitive windows as resulting from the integration of the COMSOL® simulation and user-written code. Distributiona are shown for the PMT oriented at 40° without (*right*) and with (*left*) the rotation on its own axis.

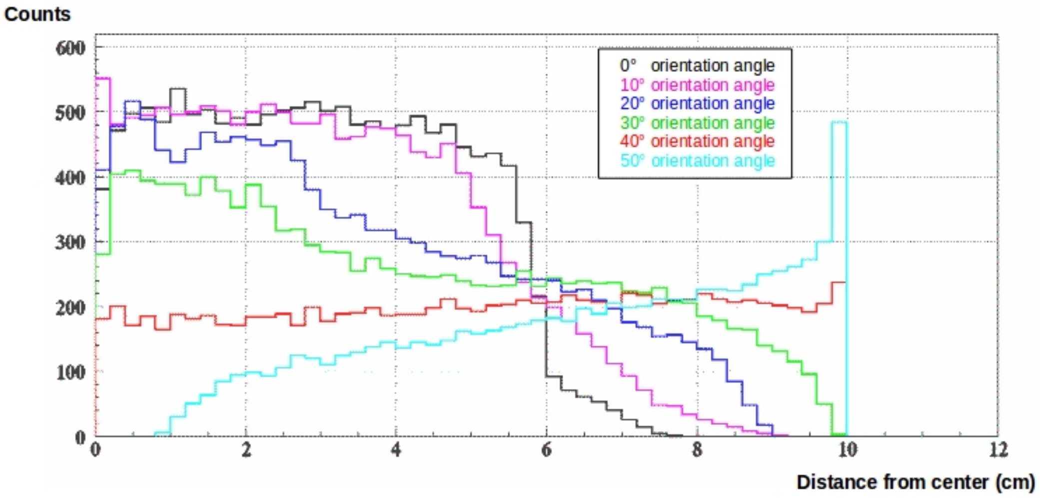

Figure 3.4: Plot of the TPB particle distribution as a function of the radial distance from the PMT window center as resulting from the integration of the COMSOL® simulation and user-written code. Curves are shown for the PMT oriented at 0°, 10°, 20°, 30°, 40° and 50° angle with respect to its own axis.

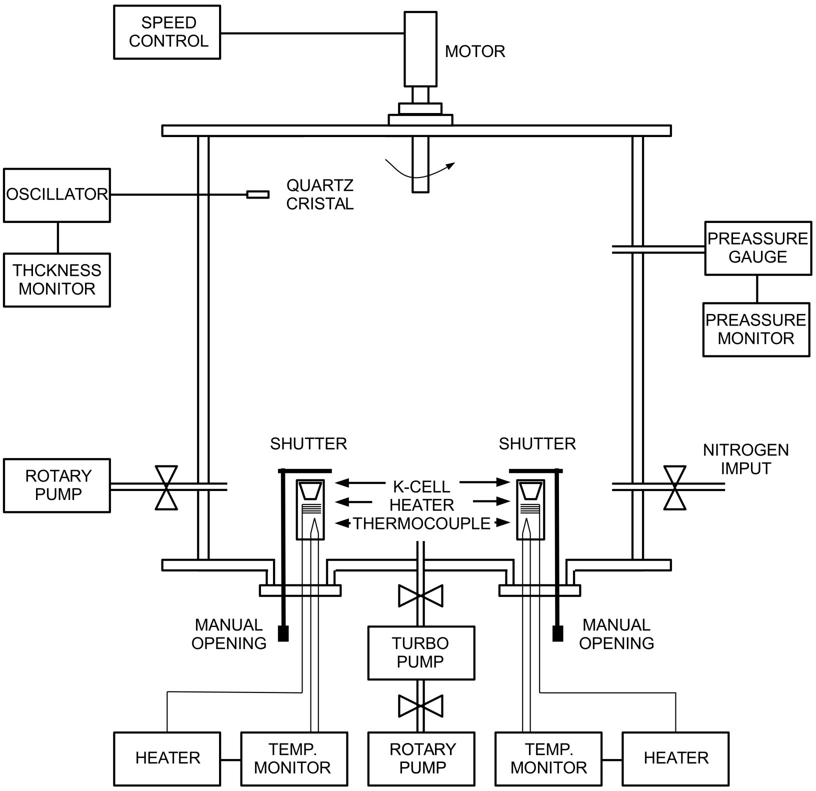

Figure 3.5: Block diagram of the overall evaporation system.

TPB vapour coming out from the cell lid aperture hits the cooler PMT surface condensating in a thin uniform film. The overall evaporation system is shown in Fig. 3.5 while its components are specifically described afterwards. A running water cooling system is also present. It consists of a pipe system, surrounding the K-cell feedthroughs and the quartz crystal feedthrough, connected to the plumbing of the building.

The Knudsen cells

The chamber houses two copper Knudsen-cells (K-cells) respectively connected to two feedthroughs at the bottom (Fig. 3.6). A thermocouple is located inside each K-cell. The position of the thermocouple has been selected to follow the internal furnace temperature as accurately as possible. The cell temperature is set by a *Temperature Controller Ero Electronics LFS* 1/16 *DIN*. It allows to increase the cell temperature by an external heater. Temperature is displayed on the monitor which is directly connected to the thermocouple. An external manual feedthrough control allows to turn an internal shutter (also shown in Figure) in order to screen the aperture of the crucible during the evaporation process, whenever is necessary.

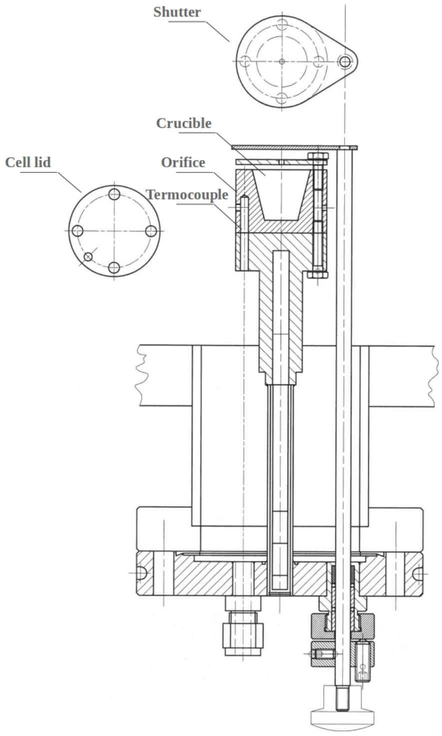

Figure 3.6: Schematic design of the copper Knudsen cell.

The vacuum system

The vacuum chamber is connected to two different vacuum system, a first one to perform a starting rough pumping, and a second one to reach the high vacuum regime.
The first pumping system is made of a single dry scroll pump (Varian TriScroll 600), which allows to reach pressure of $\sim 10^{-2}$ *mbar*. The second one is made of a rotary pump *Edwards RV12* connected to a turbo-molecular pump *Alchatel ATH 300C*, which is in turn connected to the chamber by a pneumatic valve. When pressure is low enough (about 10^{-1} *mbar*) an automatic system allows the valve to open connecting the second pumping system to the vacuum chamber. Pressure values are read by a *Compact Full Range Gauge PKR251* and they are displayed on a *Pfeiffer vacuum gauge controller*.

The PMT holding system

The PMT is fixed to a specific rotating support, below the vacuum chamber lid looking downwards with respect to the vertical direction (Fig. 3.7). The rotating structure is connected to an external stepper motor by a *Kenosistec* ferrofluid-based feedthrough allowing to keep the vacuum level during the PMT rotation. On the inside, the PMT is connected to the holding structure by a dedicated plastic collar realized with a 3D printer. It also allows to grab the

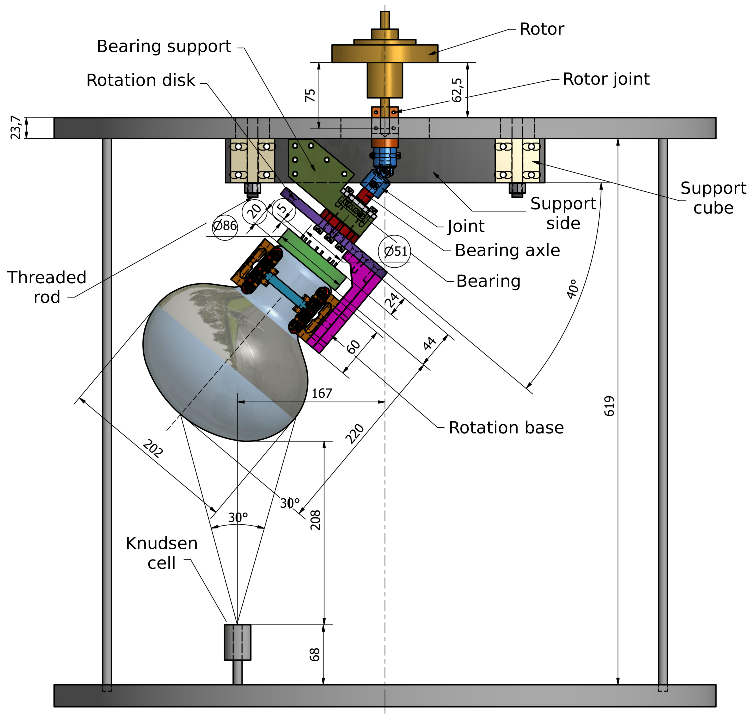

Figure 3.7: Schematic design of the rotating PMT support.

PMT after the evaporation process without touching the coated surface.

The thickness monitor

During the evaporation, a *Sycon STM-100/MF Thickness/Rate monitor* allows to monitor the process. It is connected to a quartz crystal located inside the chamber. The crystal is in turn connected to an external *Sycon OSC-100A Oscillator*. The monitor sets as zero the starting quartz oscillation frequency and measures the quantity (thickness) of material deposited on the crystal surface as a function of the variation of the quartz oscillation frequency. The monitor displays the coated thickness value both per time unit ($\text{Å}/s$) and integrated on the whole process.

3.4.1 The evaporation process

Before starting the evaporation process, the sample surface shall be cleaned in order to avoid any kind of contamination. The cleaning was done by using at first acetone (C_3H_6O), in order to remove any residual grease from the sample surface, and then by using isopropyl alcohol (C_3H_8O) in order to remove any trace of water.

After cleaning, the sample is placed inside the vacuum chamber and pumping may start. At vacuum level lower than 10^{-1} $mbar$ the first pumping system is switched off and only the second system stays on during the whole operation.

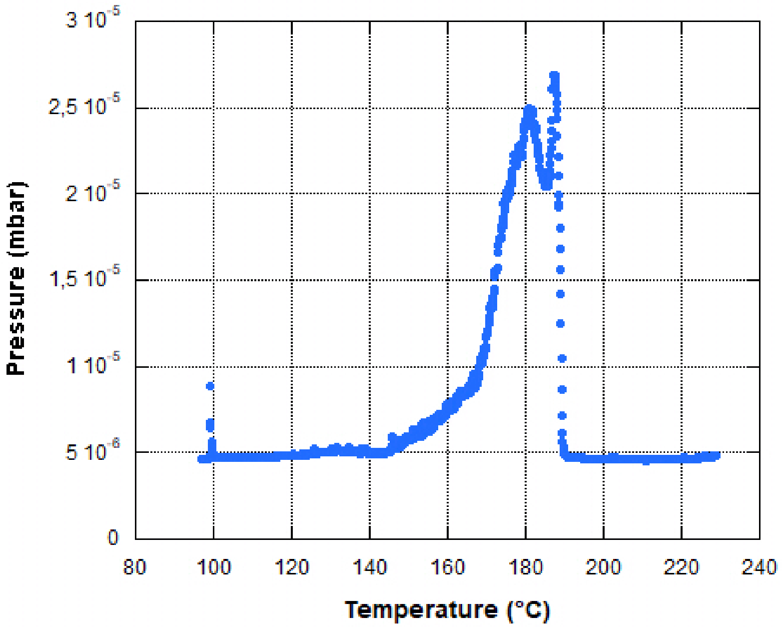

Figure 3.8: Pressure value during the whole evaporation process. It is possible to observe a first peak (water evaporation), a second one (TPB boiling point) and a last peak (shutter opening).

When the vacuum level reaches $\sim 10^{-5}$ $mbar$, evaporation process is started. The temperature is increased up to 220°C and the PMT rotation in switched on. At 100°C it is possible to see some small peaks of pressure due to the evaporation of water and other impurities condensed on the cell (Fig. 3.8). At $\sim$ 185°C TPB reaches its boiling point and it is possible to observe a second peak of pressure. Until this moment the shutter stays closed in order to avoid that water and other impurities reach the surface of the PMT. When pressure is dropping back, the shutter can be open and the real evaporation process starts. At this moment, pressure has a last peak before dropping down again and stabilise at few 10^{-6} $mbar$ over the duration of the process.
The process can be checked by the thickness monitor. In particular, it is possible to observe an increase of the thickness rate value ($\mathring{A}/s$) corresponding to the quantity of material reaching the crystal. The rate increases until reaching a plateau which means that the quantity of evaporating TPB is constant in time. When all the material contained in the cell is gone, the process is concluded and the thickness rate drops to zero. Before opening the chamber, the system shall be leave at vacuum condition for $\sim$ 20 min in order to allow the stabilization of the TPB condensate layer on the PMT surface.

Figure 3.9: Picture of the PMT mockup fixed on the evaporator lid. The mylar samples used for density measurements are also visible (transparent sqares).

3.5 Measurement of the TPB density

The first step was to verify the effectiveness of the rotating support system. In particular, it was important to check the coating uniformity on the PMT sensitive window, namely the material thickness per surface unit. This type of measuring is not so trivial. The PMT window is curved and sandblasted. These traits made impossible to measure directly the thickness on the PMT surface by using any kind of mechanical or optical thickness meter. The adopted solution was the realization of a PMT mockup allowing to measure the local density in different position on the PMT surface. It consists of two metallic strips, curved according to the PMT curvature radius and welded together. To perform local density measurements, some mylar samples were fixed on the mockup in different positions. Five samples per evaporation were used: one in the center, corresponding to the welding point, three halfway on the strips and the last one on the external edge (Fig. 3.9).

The samples weight was measured before and after the evaporation process by using a balance accurate to 10^{-4} g in order to know the precise quantity of TPB deposited quantity on each sample. Fig. 3.10 shows uniformity test results carried out with different quantities of TPB.

In Fig. 3.10 the resulting densities for the five samples are shown. The TPB density of the external sample results much smaller than the other. This is due to the system geometry. The external sample was located on the border of the evaporation cone resulting with only half of its surface subject to the evaporation process. However the position of the external sample corresponds to the PMT sensitive window border where few photons are expected. In Fig. 3.11 the resulting densities as a function of the position on the PMT surface

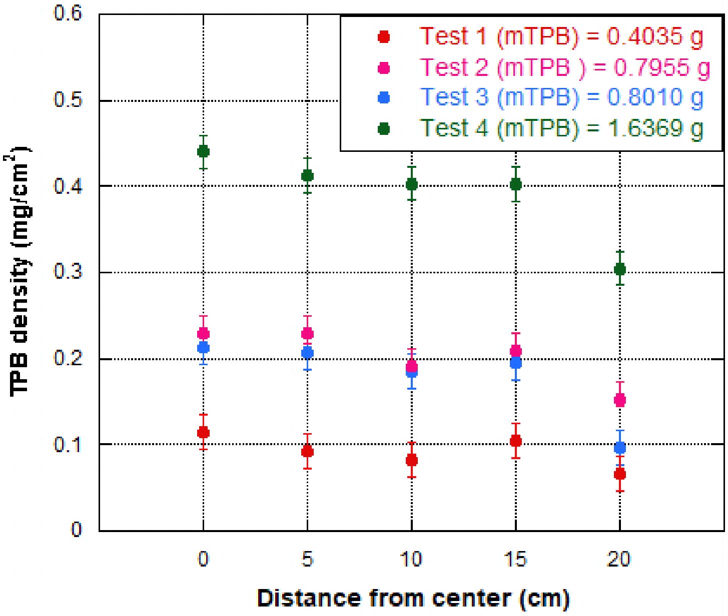

Figure 3.10: Resulting coating densities for the five samples fixed on the mockup in different positions.

are shown. Values are normalized to the higher-density sample that turned out to be the central one in each test. The obtained coating densities result to be uniform within the 10% demonstrating the good reliability of the adopted PMT holding support and system geometry.
The next step was to verify its consistency also in terms of light conversion. Moreover, it was also necessary to observe how the light conversion is related to the the resulting TPB thickness in order to define the TPB quantity to be used per evaporation. This and further test were done by using an optical device (see next chapter for details) which allows to measure the overall photomultiplier and TPB Quantum Efficiency. However, mylar samples are not suitable for this type of measure due to few mechanical issues related to the optical device (mylar is too flexible). For this reason, a new type of samples support was realised allowing to coat some round slides, which also allowed a better-localized studies of the density uniformity.

3.6 Density measurements on slides

The new support was designed with AutoCAD and realised by using a 3D printer (Fig. 3.12). It allows to simultaneously coat 17 slides of 1” diameter located on two orthogonal axis having the same PMT curvature radius, as the previous support. In this way, it was possible to perform a new more-localized densities study with more samples having smaller surfaces. Slides were fastened in designed flared areas to avoid shadow effects on the TPB thickness (Fig. 3.13).

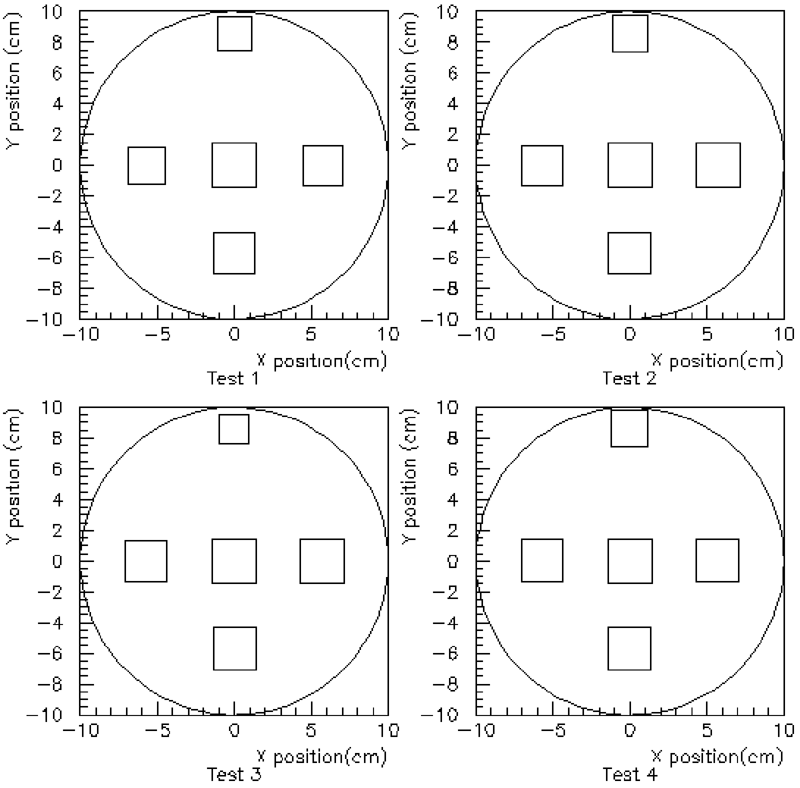

Figure 3.11: Resulting coating densities displayed in their position on the mock-up. The dimension of the squares is normalized as a function of the higher-density sample.

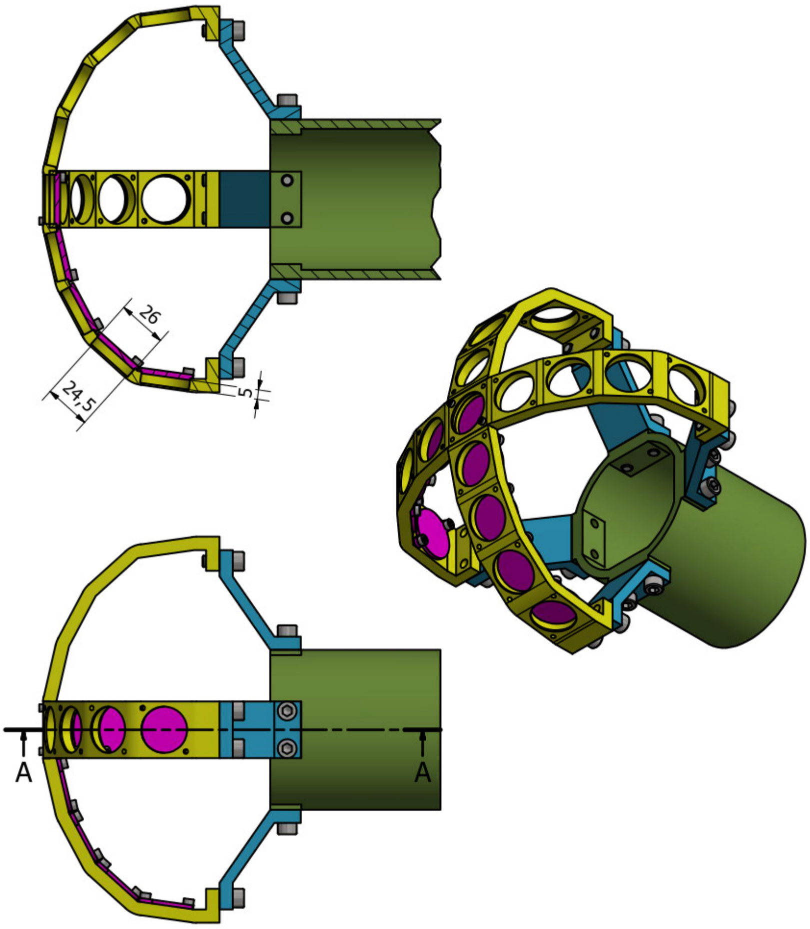

Figure 3.12: Design of the new 3D-printed support which allows to perform density test by using round slides.

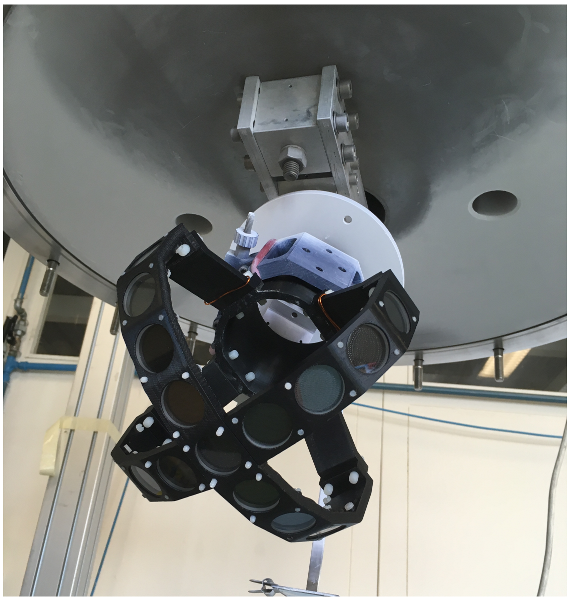

Figure 3.13: Picture of the 3D-printed PMT mockup fixed on the evaporator lid. Slides are also well visible in their locations.

Slides weights were again measured before and after the evaporation process by using a balance accurate to 10^{-4} g. Evaporation was done with 0.8 g of TPB and starting from a pressure values of 3×10^{-6} $mbar$. Resulting densities are shown in Fig. 3.14.

Results show an excellent uniformity between the center and the slides located in the first 2 position on the 4 arms (see also Fig. 3.15). On the border, the TPB density drops by more than 60%. Even in this case, this is probably due to the system geometry. The external sample was located on the border of the evaporation cone resulting only half-covered. The percentage of TPB deposited per slide is also showed.

This last density test finally shows the good performance of the system geometry and evaporation process in terms of coating thickness uniformity. The later step was to verify the reliability of the evaporation device and process also in terms of light yield conversion. To this purpose, a new set of tests was performed by using an optical device which allow to measure the overall TPB coating and photomultiplier Quantum Efficiency. These measurements are described in the next chapter.

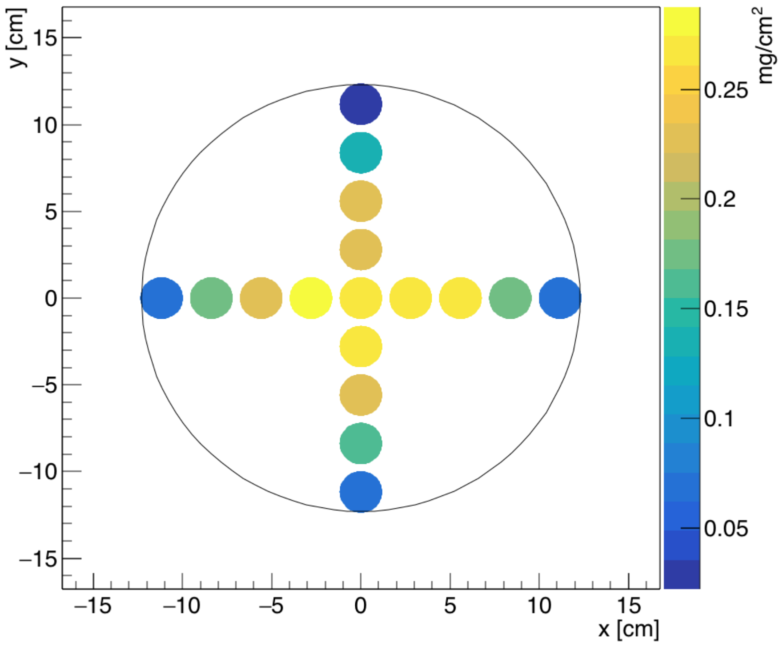

Figure 3.14: Resulting coating densities as a function of the positioning of slides on the 3D-printed support.

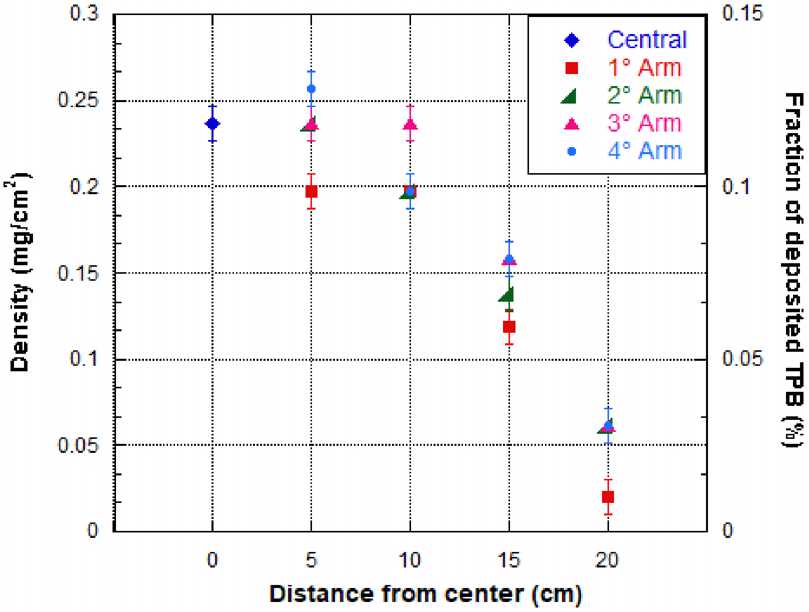

Figure 3.15: Resulting densities for all the 17 slides as resulting as a function of the distance from the center. The percentage of the whole used TPB deposited per slide is also shown.

CHAPTER 4

QUANTUM EFFICIENCY MEASUREMENTS AND DETERMINATION OF THE EVAPORATION PARAMETERS

In the previous chapter, some tests verifying the reliability of the evaporation device and process were shown. In particular, these tests were based on density measurements in order to determine the best thickness uniformity achievable with the evaporation system. However, what really matters for the experiment purpose is the TPB coating uniformity in terms of light conversion. For this reason, an optical device was set up allowing to measure the overall photomultiplier and TPB Quantum Efficiency (QE), namely the ratio of the number of photoelectrons released by the photocathode to the number of photons absorbed by the wavelength shifter. In the following , the procedure on which Quantum Efficiency measurements are based is described [43].

4.1 Introduction

Considering a photomultiplier struck by photons of wavelength λ, the anodic current produced by the photomultiplier is given by:

$$I_A(\lambda) = N_\gamma(\lambda) \cdot QE_K(\lambda) \cdot \varepsilon \cdot G \cdot e$$

where N_γ is the number of incident photons per time unit, QE_K is the photocathode Quantum Efficiency, G is the dynode chain gain, ε is a constant value which considers the collection efficiency of the PMT focusing stage and e is the electron charge. Beside, the cathodic current produced by photoelectrons is given by:

$$I_K(\lambda) = N_\gamma(\lambda) \cdot QE_K(\lambda) \cdot e$$

Then, the photocathode Quantum Efficiency $QE_K(\lambda)$ can be written as:

$$QE_K(\lambda) = \frac{I_K(\lambda)}{N_\gamma(\lambda) \cdot e}$$

The cathodic current can be measured by short-circuiting the PMT dynodes and grids and by applying a potential difference between cathode and first dynode. The number of photons $N_\gamma(\lambda)$ can be measured by means of a *calibrated photodiode*, namely a characterised diode whose Quantum Efficiency QE_D as a function of the incident wavelength is well know and is given by tabulated values. Its value is then given by:

$$N_\gamma(\lambda) = \frac{I_D(\lambda)}{QE_D(\lambda) \cdot e}$$

where I_D is the photodiode current. It is then possible to measure the PMT Quantum Efficiency by comparing the photomultiplier cathodic current to the calibrated photodiode current:

$$QE_K(\lambda) = QE_D(\lambda) \times \frac{I_K(\lambda)}{I_D(\lambda)} \tag{4.1}$$

This type of measurement can be realised by focusing a monochromatic VUV source on the calibrated photodiode at first, and then on the photomultiplier window. The process shall be performed at vacuum condition in order to avoid the UV light absorption by air molecules.

4.2 Set-up of the optical device

The optical device used for the Quantum Efficiency measurements is shown in Fig. 4.1. It consists of:

- **Deuterium lamp McPherson mod.632** [44] which features a front Magnesium Fluoride window of 1 *mm* diameter. The emission spectrum has two peaks at 121 *nm* and 161 *nm*. Other technical specifications are set out in Table 4.1. The emission spectrum is shown in Fig. 4.2.

- **Focusing system** which allows to focus the lamp light to the monochromator. Focusing is realized by an UV reflecting mirror. In this way, chromatic aberration effects are removed.

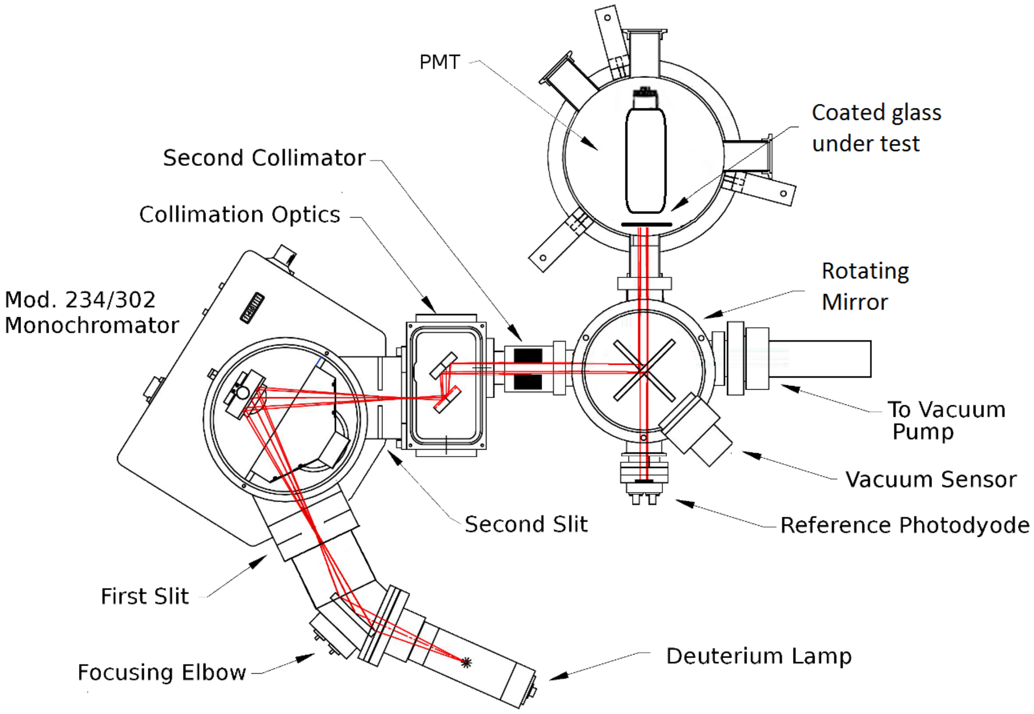

Figure 4.1: Schematic design of the optical device used for Quantum Efficiency measurements on TPB coated samples.

Lamp Type	Deuterium
Wavelength Range	115 to 380 nm
Power	30 Watts
Plasma Size	1 mm diameter
Windows Material	Magnesium Fluoride
Lifetime	1000 hours

Table 4.1: Technical specifications of the Deuterium lamp McPherson model 632.

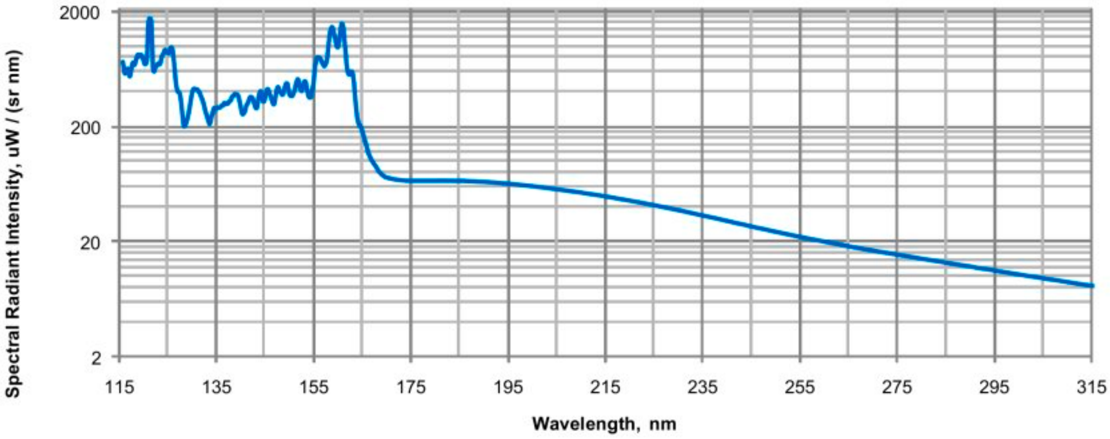

Figure 4.2: Spectral radiant intensity of the Deuterium lamp McPherson model 632 [44].

Focal length	200 + 200 mm
f/number	4.5
Resolution	0.05 nm
Dispersion	1.8 nm/mm
Accuracy	0.1 nm
Base vacuum	1×10^{-6} torr

Table 4.2: Technical specifications of the Monochromator McPherson 234/302.

- **Monochromator McPherson 234/302** [45]. Light from the lamp gets into the monochromator through a first slit, which allows to calibrate its intensity. A diffraction grating (120 $ridges/mm$) and a second slit permit to select the light wavelength and to regulate its range amplitude. Monochromator technical specifications are set out in Table 4.2.

- **Scan controller McPherson 789A-3** [46] which allows to control the monochromator by a computer in order to select the outgoing wavelength.

- **A first reflector collimator** which stabilises the light beam dimension and reduces its divergence.

- **A second collimator** composed by an hollow black cylinder (41 mm external diameter, 6 mm inner diameter, 30 mm length).

- **Rotating mirror ACTON 1200-FS-2D** placed in a cylindrical vacuum chamber. The mirror allows to select the delivering of the light beam towards one of the two contiguous chamber, containing the sample under test and the reference photodiode respectively. The mirror is

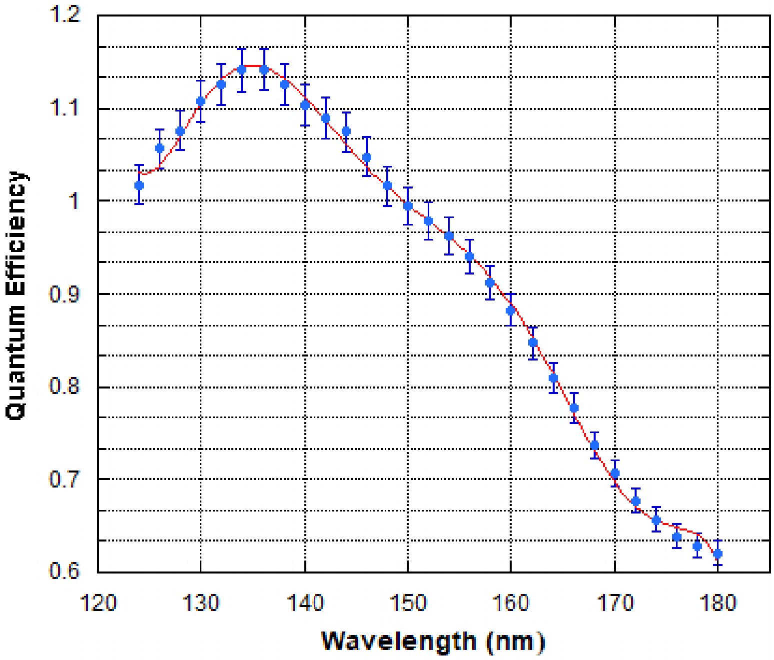

Figure 4.3: Calibration curve of the photodiode AXUV-100G as a function of the wavelength of the incident light.

Active Area	100 mm^2
Responsivity	0.08 A/W
Shunt Resistance	20 $M\Omega$
Reverse Breakdown Voltage	10 V
Capacitance	10 nF
Rise Time	10 μs

Table 4.3: Technical specification of the photodiode AXUV-100G

coated with $Al + MgF_2$ and its reflectivity is $78 - 83\%$ at 121.6 nm. The optical path of the light towards both the diode and the PMT is the same so the final result can't be affected by any error on reflectivity.

- **Calibrated photodiode RID AXUV-100G.** This is a semiconductor device that converts light from a wide wavelength range ($\sim 110 \div 300$ nm) into electrical current. The photodiode has been calibrated by the National Institute of Standard and Technology (NIST), so its own light yield efficiency is given by tabulated values. The light yield efficiency for this photodiode is shown in Fig. 4.3 as a function of the incident light wavelength. Quantum Efficiency at 128 nm has been interpolated from the tabulated values by fitting a polynomial curve and its values is $QE_D(\lambda = 128\ nm) = 1.0758$. Photodiode technical specification are shown in Table 4.3.

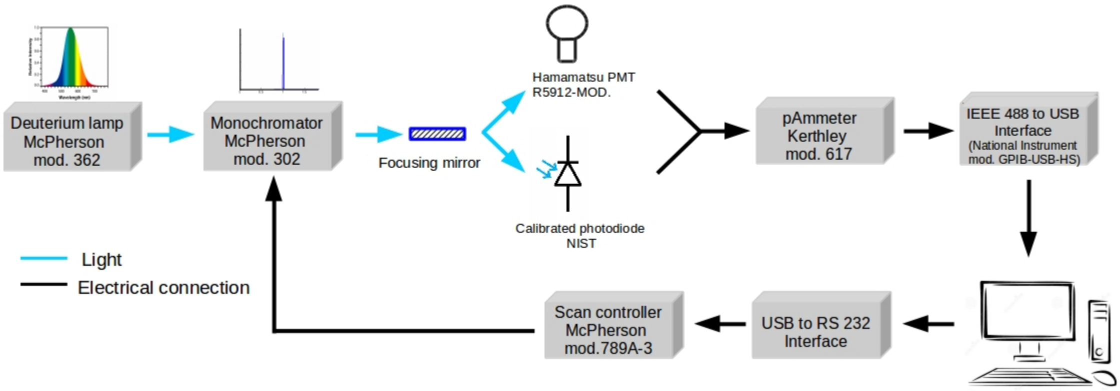

Figure 4.4: Block diagram of the acquisition chain developed to carry out the Qunatum Efficiency measurements.

- **Measuring chamber** in which it is possible to place the sample under test in front of a 1.5" photomultiplier tube. The chamber is kept at vacuum and dark condition and the internal walls are covered by an opaque material in order to avoid photons diffusion. A second chamber permits to place an 8" PMT in front of the light beam, as described in Section 4.4.

- **Vacuum system** is composed by a primary pump *VARIAN SH0-100* connected to a turbo molecular pump *VARIAN Turbo V-70 LP*. Vacuum level is measured by a *EDWARDS Active Gauge AIM-S-NW25*.

The block diagram displaying the acquisition system is shown in Fig. 4.4. The McPherson controller scan is connected to the lab computer by the standard interface *RS-232*. In that way, it is possible to control the scan by using a dedicated LabVIEW program which allows to select a specific wavelength or to scan all the wavelength lamp spectrum with a settable pitch. The resulting current from both the cathode photomultiplier and the photodiode is alternately measured by a pico-ammeter *Kerthley mod.617*. The device is in turn connected to the computer by the National Instrument standard IEEE488-USB interface *GPIB-USB-HS*.
The PMT power supply is provided by an High Voltage power supply *BERTAN series 230*.

4.3 Quantum Efficiency measurements on slides

As first step, measurements of the relative Quantum Efficiency were done on slides. Slides were evaporated at different condition (i.e. TPB quantities and evaporation rate) by using the 3D-printed support described in Section 3.6 in order to find, if exists, a correlation between the evaporation parameters and

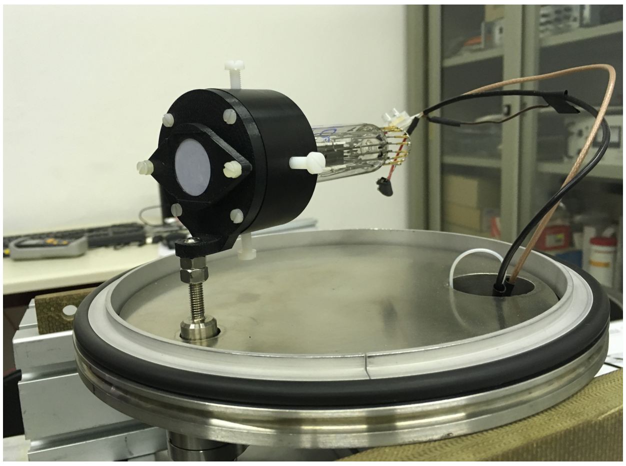

Figure 4.5: Picture of the slides measuring system. Slides were placed in front of the 1.5" photomultiplier by means of the black plastic support shown in picture.

the light yield conversion of the TPB. All the following measurements were realized at ultra high vacuum regime (few 10^{-5} $mbar$). Slides were placed in front of a 1.5" photomultiplier *ETL D830* by means of a specific plastic support showed in Fig. 4.5. Measurements were performed by setting the monochromator entrance slit at 3 mm aperture, while the output entrance slit was set at 1 mm aperture. The resulting wavelength resolution of the outgoing light is of the order of 4 nm. The PMT power supply was set at 200 V. In all the following measurements, a systematic error on the QE value of the 5% has been considered. This error is obtain by adding the systematic error of the optical instrumentation.

4.3.1 Quantum Efficiency vs TPB density

Quantum Efficiency was evaluated as a function of the TPB coating density. Slides were coated by evaporation with different quantities of TPB. Every process was performed starting from a vacuum regime of 3×10^{-5} $mbar$. To reach high density values, some slides were coated with consecutive processes. For this reason, a further measurement was done in order to point out any difference, in terms of light yield conversion, between single and consecutive evaporations on equal densities. In Fig. 4.6, the overall QE response is shown for two slides having the same TPB covering densities and coated respectively by a single and two consecutive evaporations. QE response was evaluated all over the significant deuterium lamp spectrum, ranging from 120 nm to 170 nm. Over 170 nm, the photodiode cathodic current results too low and QE value tends to infinity.

Results show a small difference in QE response between the two glass samples. However, the difference is within the systematic error. Therefore, it can be reasonably assumed that there is no significant difference in QE response be-

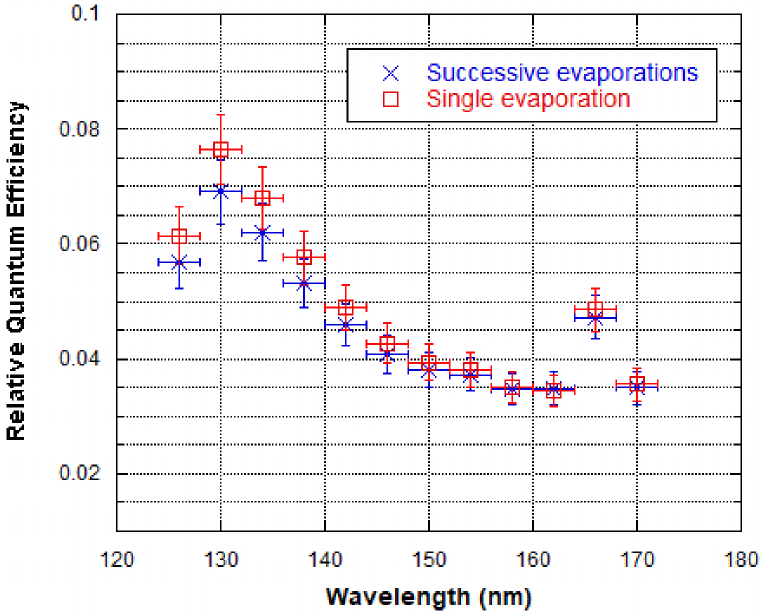

Figure 4.6: Relative Quantum Efficiency for two slide coated with 0.8 g of TPB by a single and two consecutive evaporations respectively.

tween samples coated by single and consecutive evaporation processes of equal densities.

By a single evaporation starting with 0.8 g of TPB, coating densities from 0.03 to 0.23 mg/cm^2 were obtained. Some of this slides were coated again in order to obtain densities up to 0.45 mg/cm^2. Thereafter, slides QE as a function of the coating densities was measured by means of the optical device. Measurements were done by setting the monochromator at $\lambda = 160\ nm$, where the deuterium lamp emission has a peak. Results are shown in Fig. 4.7.

TPB is transparent to its own emitted photons. What's ideally expected is a QE response curve which at some point, reaches its maximum level and remains constant with increasing the coating density. However, during the evaporation process (or during the samples storage) it is possible that TPB layer being contaminated by water molecules and other impurities present in air or on the PMT surface. What one really expects is then a QE response curve which slowly drops with increasing the coating density. Results of the optical tests, shown in the above figure, are in good agreement with the expected results.

From this test, it is reasonable to assume $\sim 0.23\ mg/cm^2$ as final layer density for the series production of PMTs, which correspond to an initial TPB quantity of 0.81 g. In fact, at this coating density, QE has already reached its maximum value and the TPB thickness layer is thin enough to avoid any kind of problem at cryogenic condition [47]. For this reason, the following tests were done by using an initial TPB quantity of 0.81 g, considered optimal.

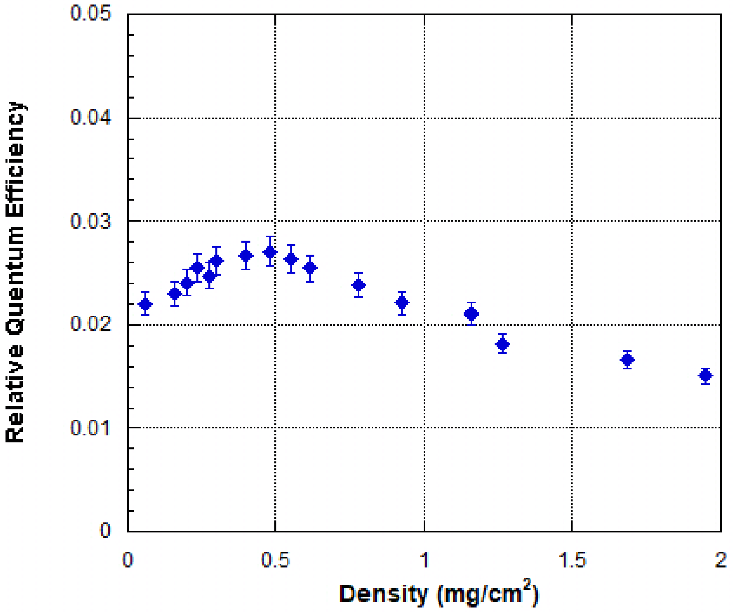

Figure 4.7: Quantum Efficiency distribution as a function of the TPB coating density.

4.3.2 Quantum Efficiency vs slide position

A second test consists in measuring the coating uniformity on the PMT surface from the point of view of the light conversion yield. For this reason, 17 slides were coated by evaporation by using the 3D-printed support already shown in Section 3.6. Evaporation was performed with 0.81 g of TPB and starting from a vacuum regime of 3×10^{-5} $mbar$.

After the evaporation, slides were placed in front of the photomultiplier in the measuring chamber. Measurements were done by setting the monochromator at $\lambda = 160$ nm, where the deuterium lamp emission has a peak. The resulting relative overall QE is shown in Fig. 4.8.

Results show a good light conversion yield uniformity, according to the previous results obtained in the density uniformity test (see Section 3.6). The resulting QE also shows an excellent uniformity between the center and the 8 slides placed in the next two position on the 4 arms. In the last position, the QE is reduced only by the 1%. This last result demonstrates the success of the adopted technique for the TPB deposit both in terms of geometrical study and realisation of the thermal evaporation. Moreover, the PMT holding system and the setting of the evaporation process result adequate also for what concerns the light conversion uniformity.

4.3.3 Quantum Efficiency vs evaporation rate

The thickness monitor installed on the evaporation system (see Par. 3.4) allows to monitor the growth of the deposition. In particular, the device displays

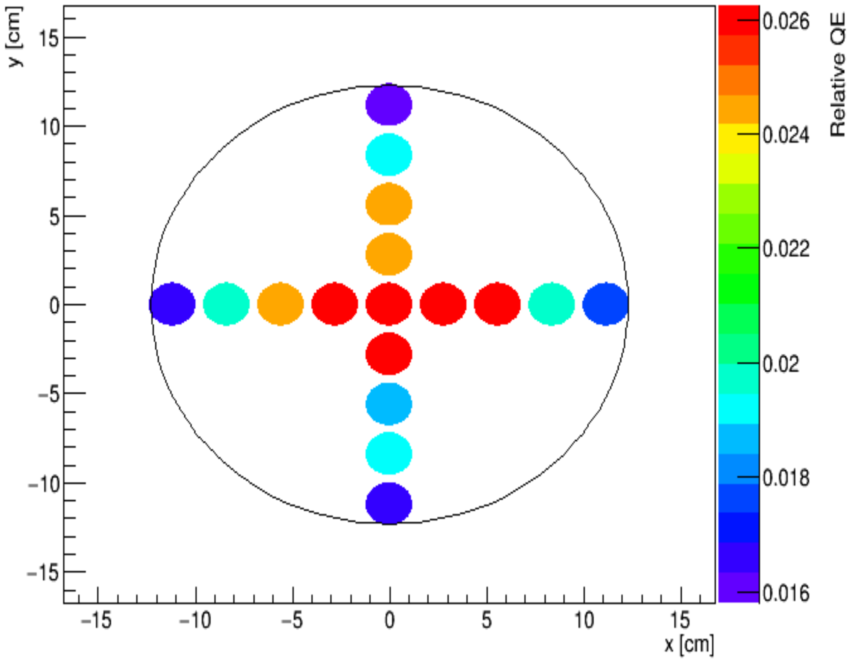

Figure 4.8: Relative Quantum Efficiency for the 17 slides as a function of their location on the 3D-printed support.

the total layer thickness deposited on the crystal (measured in $k\text{Å}$) and the evaporation rate, namely the coating thickness per time unit (measured in $\text{Å}/s$). This last parameter depends on the temperature set during the process. A set of test were performed in order to verify if a correlation exists between the evaporation rate and the QE. In the first test, 5 slides were placed in the 3D-printed support, one in central position, 3 in random position on the first two concentric circles and a last one in the third circle. Slides were coated with 0.81 g of TPB and starting from a vacuum regime of 3×10^{-5} $mbar$. During the process, the heater temperature was increased up to $200°C$ and left at this value for all the duration of the process, which took about 25 min. The displayed average rate was around $2 - 3$ $\text{Å}/s$. Hereafter, other 5 slides were placed in the 3D-printed support in the same positions and coated at the same environmental condition (0.81 g of TPB and 3×10^{-5} $mbar$ vacuum regime). In this case, the heater temperature was increased up to $220°C$. The evaporation process took ~ 15 min and the displayed average rate was around $8 - 9$ $\text{Å}/s$. Lastly, a third evaporation was done by increasing the heater temperature up to $230°C$. The evaporation process lasts few minutes and the displayed average rate was around $15 - 16$ $\text{Å}/s$. The evaporation rate was registered by using a National Instrument interface to connect the Sycon device to the computer. A specific LabVIEW program allows to measure the rate value at given time interval. The rate was registered for each type of evaporation procedure described above. The resulting curves are shown in Fig. 4.9.

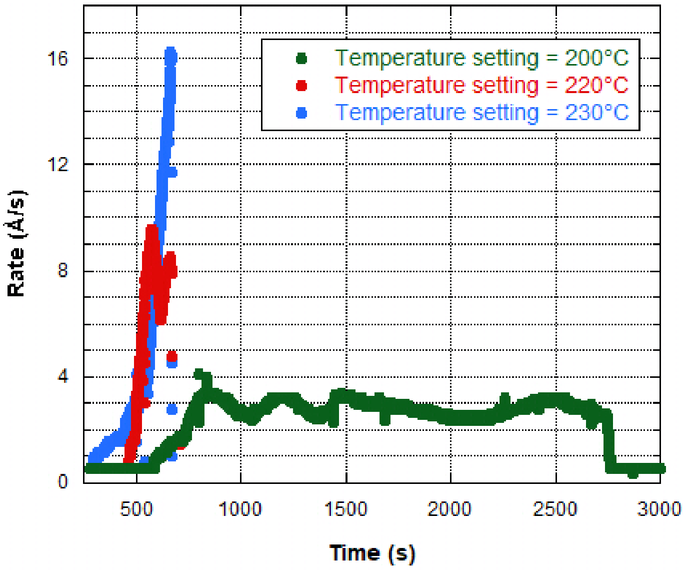

Figure 4.9: Evaporation rate for three different evaporation procedures.

The three obtained sets of slides were then tested by the optical system. Measurements were done by setting the monochromator at $\lambda = 160\ nm$, where the deuterium lamp emission has a peak, and starting from a vacuum regime of $5 \times 10^{-5}\ mbar$. In Fig. 4.10, the QE response as a function of the TPB coating density for the three sets of slides, corresponding to different values of evaporation rate, is shown. From the obtained curves, it is possible to note a correlation between the QE and the evaporation rate. In particular, the resulting QE seems to increase with the rate value kept during the coating process. This is probably due to the lower quantity of impurities involved in a faster evaporation process. For this reason, the best choice for what concerns the evaporation procedure is to perform the evaporation as fast as possible. Therefore, this means to keep an evaporation rate of around $15 - 16\ \AA/s$, as obtained in the last set of evaporation described above with the heater temperature set at $230°C$. However, as shown in Fig. 4.9, this type of process is extremely difficult to control, due to its short duration (only few minutes). Moreover, such a fast evaporation on a rotative target could compromise the TPB coating in terms of uniformity. For this reasons, the more suitable evaporation procedure shall be obtained by keeping the evaporation rate at the average values of $8 - 9\ \AA/s$. Next tests were done by following the procedure described above in order to keep this average rate value during all the processes.

4.4 Quantum Efficiency measurements on PMTs

After measuring the overall QE on slides, measurements were done directly on some PMT samples. For this reason, the set-up of the optical system has

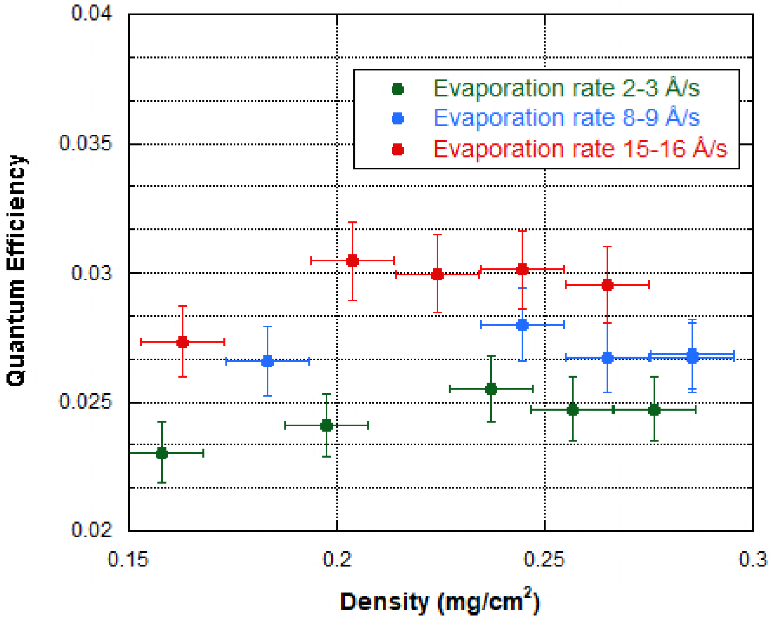

Figure 4.10: Quantum Efficiency response as a function of the coating density as resulting for three sets of slides caoted at different evaporation rate values.

been modified. In particular, the measuring chamber was replaced by a wider one that allows to contain the 8 *in* PMT under test. The PMT can be fixed on the chamber lid by means of a supporting ring connected to a rotating feedthrough (Fig. 4.11). In that way, it is possible to turn acting from outside the chamber the PMT under test perpendicularly to its own axis, in order to map its sensitive window in different positions along a circle (see Par. 4.4.3). In this configuration, the p-ammeter was directly connected to the photomultiplier under test. The internal walls of the new measuring chamber were also covered by an opaque material in order to avoid photons diffusion. All the PMT measurements were performed at ultra high vacuum regime (few 10^{-5} $mbar$). The monochromator entrance slit was set at 3 mm aperture, while the output entrance slit was set at 1 mm aperture. The resulting wavelength resolution of the outgoing light was of the order of 4 nm. The PMT power supply was set at 200 V. In all the following measurements, a systematic error on the QE value of the 5% has been considered. This error is obtained by adding the systematic error of the optical instrumentation.

4.4.1 PMT response to the incident light

At first, the PMT response to the incident wavelength light spectrum has been evaluated. The evaluation was carried out all over the effective deuterium lamp spectrum, ranging from 120 nm to 220 nm, by means of the LabVIEW program which allows to remotely control the monochromator scan controller. In particular, the program allows to automatically scan the lamp spectrum

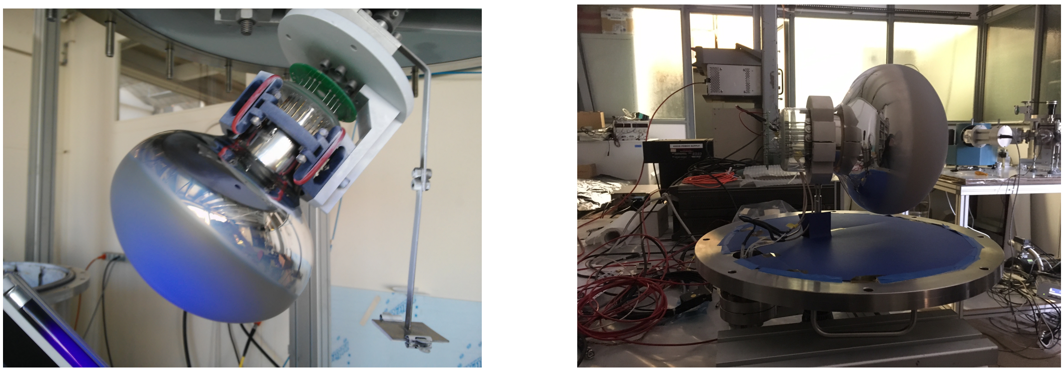

Figure 4.11: Pictures of an evaporated PMT *(left)* and of the rotative support used to measure the Quantum Efficiency directly on the PMTs *(right)*.

with a defined wavelength step. At the same time, the resulting cathodic current from the p-ammeter is recorded. Measurement was done at a vacuum regime of $5 \times 10^{-5}\ mbar$. In Fig. 4.12 the resulting response for a PMT sample is shown. At 128 nm the resulting QE is $\sim 11\%$. At 165 nm, which might be interesting for Xenon experiments, it is $\sim 10\%$.

4.4.2 PMT response distribution at $\lambda = 128\ nm$

PMT response has been evaluated at $\lambda = 128\ nm$ for few PMT samples. Measurements at $\lambda = 128\ nm$ were done by comparing the photodiode cathodic current to the resulting cathodic current produced by the PMT under test illuminated in the center of its sensitive window. All the PMTs were coated by evaporation under the same optimized conditions, namely by using 0.8 g of TPB, an evaporation rate of $\sim 7 - 8$Å$/s$ and at a vacuum regime of $5 \times 10^{-5}\ mbar$. All measurements with the optical device were done at a vacuum regime of $5 \times 10^{-5}\ mbar$. The resulting distribution is shown in Fig. 4.13. As can be seen in the distribution, all the PMT, but one, present QE values ranging from 11% to 15%. This result shows the good repeatability of the evaporation process in terms of utilised technique and facilities response.

4.4.3 QE uniformity on the PMT surface

In this test, the coating uniformity on the PMT sensitive window in terms of light yield conversion was evaluated. To this purpose, the PMT was fixed inside the measuring chamber by means of the previously desribed support ring. At first, the response at $\lambda = 128\ nm$ on the PMT sensitive window center was measured.

An example of QE variation as a function of the radial distance from the center is shown in Figure 4.14, where data are compared to the radial dependence variation for visible light of the cathode in the absence of coating obtained with a laser at 405 nm [39]. Results obtained with the TPB coating fairly re-

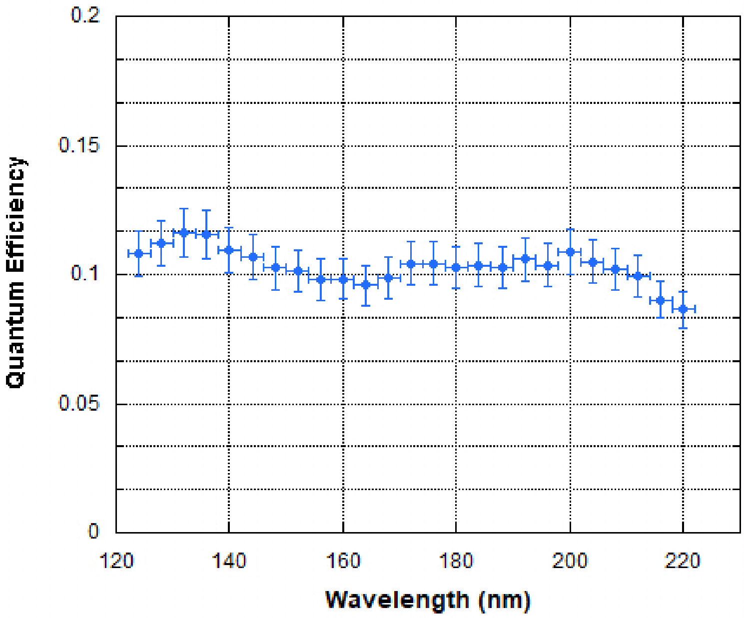

Figure 4.12: Example of PMT response to the incident wavelength light spectrum. The light wavelength ranges from 120 nm to 220 nm.

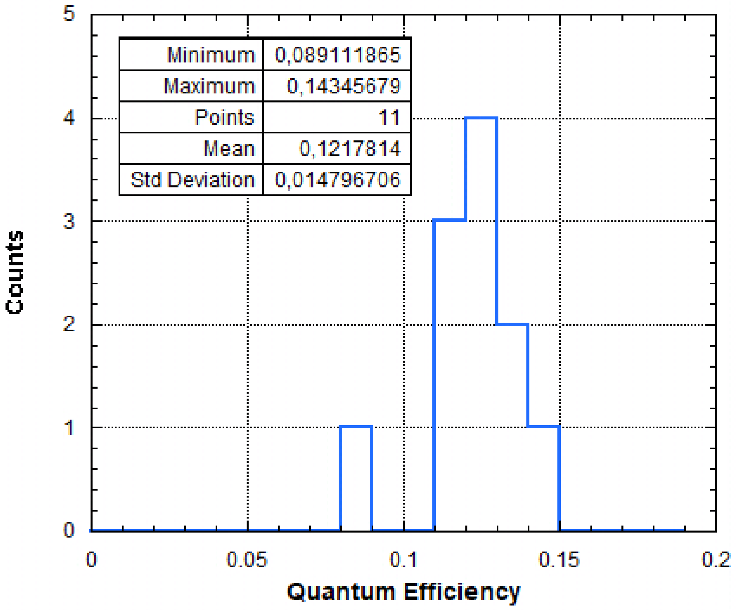

Minimum	0,089111865
Maximum	0,14345679
Points	11
Mean	0,1217814
Std Deviation	0,014796706

Figure 4.13: Distribution of the Quantum Efficiency response as resulting from measurements of 11 PMTs at $\lambda = 128$ nm.

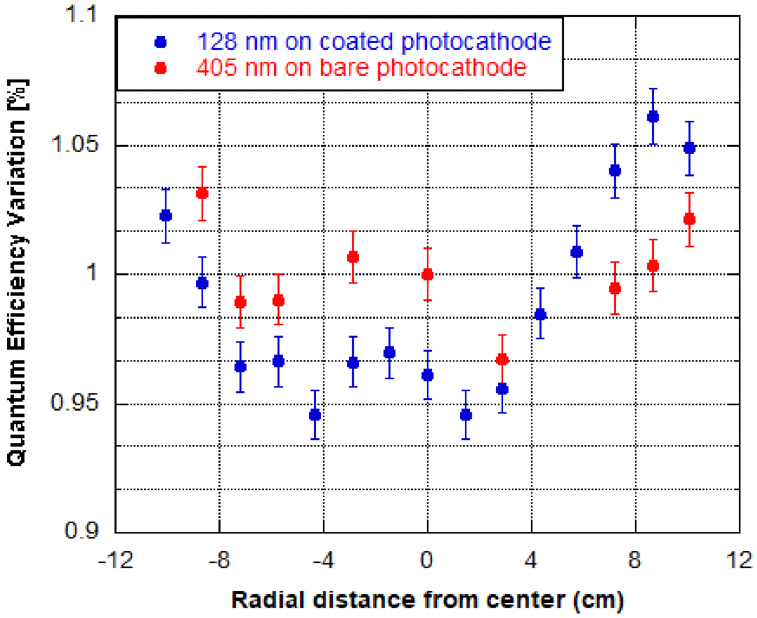

Figure 4.14: Uniformity of the quantum efficiency as function of the radial distance from the cathode center. Data measured with 128 *nm* light on the coated photocathode (blue dots) are compared to the radial dependence variation of the bare photocathode for visible light (red dots), demonstrating the good uniformity of the TPB deposit in terms of light yield conversion.

produce the photocathode behaviour for visible light, demonstrating the good uniformity of the TPB deposit in terms of light yield conversion.
After the first radial measurement, PMT was rotated perpendicularly to its own axis, along both side with 5° of pitch. In that way, the PMT response was measured along an arc of the photomultiplier window. This measure was repeated by turning the PMT on its own axis respectively of 90°, 45° and $-45°$. Results are shown in Fig. 4.15.
Test results shown a mainly flat Quantum Efficiency response all over the PMT sensitive window. This resulting distribution demonstrates the good reliability of the adopted evaporation technique, which allows to obtain the best uniformity in terms of coating thickness and light conversion yield. Test was repeated by comparing the QE response of other PMT samples along one circle, only. Results, showing again a mainly flat response, are presented in Fig. 4.16.

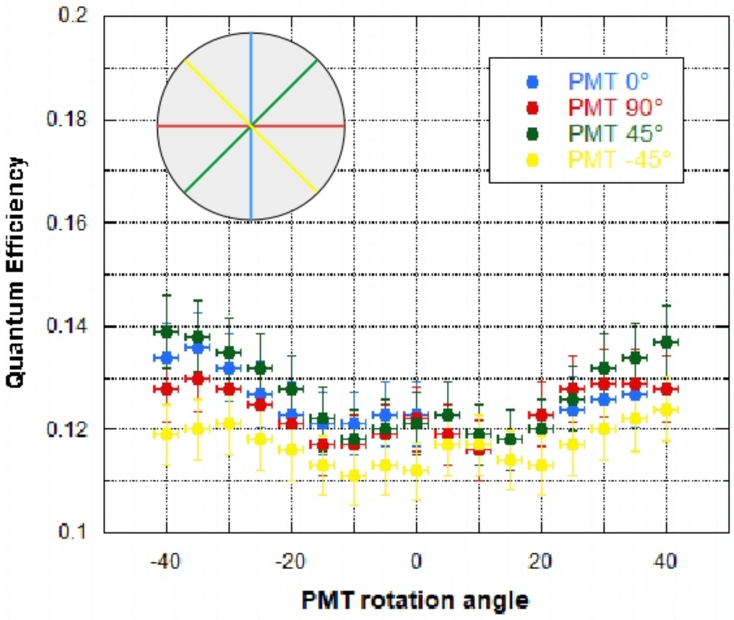

Figure 4.15: Example of the uniformity test on a PMT. The resulting Quantum Efficiency is shown along 4 different axis on the PMT window.

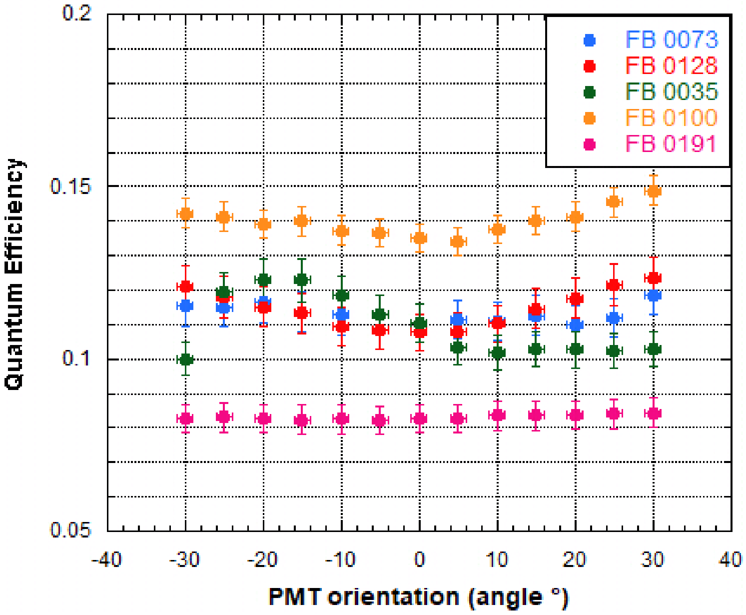

Figure 4.16: Comparison of the Quantum Efficiency uniformity test on different PMTs.

CONCLUSIONS

The presence or absence of a fourth *sterile* neutrino state is one of the main open question in the field of neutrino mixing and oscillations. In next years, a new generation of neutrino experiment is going to start, with the specific purpose to solve this puzzle.
ICARUS T600 will be part of this research as far detector of the Short-Baseline Neutrino (SBN) physics program, which includes three Liquid Argon Time Projection Chamber (LAr-TPC) detectors located along the Booster Neutrino Beam (BNB) at Fermilab (FNAL). In particular, the program goal is to perform sensitive searches for sterile neutrinos at the eV mass-scale through both appearance and disappearance oscillation channels.
The ICARUS T600 detector was moved at CERN at the end of 2014 for a complete overhauling. Various renovations were indeed required due to the experimental conditions at FNAL, where the detector will operate at shallow depths rather than deep underground as in its previous run at Gran Sasso National Laboratories (LNGS).
This Ph.D. thesis is particularly focused on the refurbishment operated on the T600 light collection system, consisting of an array of cryogenic photomultiplier tubes (PMT) installed behind the wire planes of each TPC in a dedicated sustaining structure. Refurbishment was done in order to detect with full efficiency the prompt scintillation light, produced by an ionizing event, despite the higher cosmic muons rate background at shallow depths. However, the PMT photocathode is sensitive to visible light, whereas the scintillation light produced in LAr by a ionizing event is emitted at VUV wavelength. For this reason, a study on a specific wavelength shifter, Tetra-Phenyl-Butadiene (TPB), has been performed.
TPB is an organic fluorescent chemical compound generally used as wavelength shifter in many experiments, in particular involving LAr detectors, due to its extremely high efficiency to convert VUV into visible photons. The most common method to use TPB is to deposit a thin layer on the external surfaces of the light detectors (such as PMT or SiPM) or on some inner surfaces of the whole apparatus. To obtain such TPB layers, different procedures can be

used.
In this thesis, the results of a careful study on the evaporation technique are presented. The technique consists in evaporating TPB by using a specific type of crucible, a *Knudsen cell* which allows to strictly control the process. The cell was placed inside a thermal evaporator, were a specific PMT rotating support was also installed. A preliminary study on the TPB evaporation was performed by using a PMT mock-up on which some mylar samples were fixed in different positions. In this was, it was possible to study the TPB coating density distribution as a function of the position on the PMT sensitive window.

This test was then repeated by using a 3D-printed PMT mock-up in order to perform a more-localized densities study with more samples having smaller surfaces. Density tests demonstrated the good performance of the system geometry and evaporation process in terms of coating thickness uniformity.

The later step was to verify the reliability of the evaporation device and process also in terms of light yield conversion. To this purpose, a further set of tests was performed by using an optical device which allow to measure the overall TPB coating and photomultiplier Quantum Efficiency (QE). At first, the relative QE of slides previously coated for the density test was measured, showing an excellent coating uniformity also in terms of light yield conversion. Moreover, further slides were evaporated at different condition (i.e. TPB quantities and evaporation rate) in order to find, if exists, a correlation between the evaporation parameters and the light yield conversion of the TPB. In this way, it was possible to fix the evaporation parameters which have been later applied to coat some PMT samples.

Lastly, the optical device was modify in order to measure directly the QE response of a coated PMT. Results of this test have shown a mainly flat QE response all over the PMT sensitive window in all the tested PMTs. This resulting distribution demonstrated the good reliability of the adopted evaporation technique, which allows to obtain the best uniformity in terms of coating thickness and light yield conversion.

The obtained evaporation technique was used to coat with the TPB all the 360 PMTs constituting the new ICARUS T600 light collection system. In every PMT evaporation run, a mylar sample was fixed inside the vacuum chamber in a dedicated support in order to check the coating density as in the preliminary phase. The resulting distribution of the coating densities related to all the PMTs of the series production is shown in Figure 4.17.

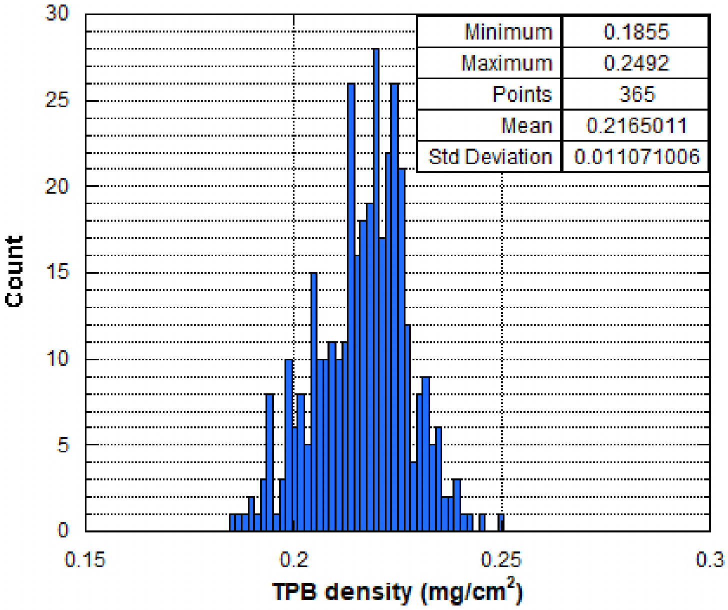

Figure 4.17: Resulting distribution of the coating densities of the mylar samples. Each sample is related to a PMT evaporation run of the series production. In addition, 5 more PMTs were coated as spare.

BIBLIOGRAPHY

[1] C. Giunti, C.W. Kim, *Fundamentals of neutrino physics and astrophysics*, (2007).

[2] B. Pontecorvo, Sov. Phys. JETP 6-429, Sov. Phys JETP 7-172 (1958).

[3] C. Patrignani et al.(Particle Data Group), *Review of particle physics*, Chin. Phys. **C40**, 100001 (2016).

[4] A. Aguilar et al. [LSND Collab.], *Evidence for neutrino oscillations from the observation of anti-neutrino(electron) appearance in a anti-neutrino(muon) beam*, Phys. Rev. **D64**, 112007 (2001).

[5] A.A. Aguilar-Arevalo et al. [MiniBooNE Collab.], Phys. Rev. Lett. **105**, 181801 (2010); Phys. Rev. Lett. **110**, 181802 (2009).

[6] A.A. Aguilar-Arevalo et al. [MiniBooNE Collab.], Phys. Rev. Lett. **98**, 231801 (2007); Phys. Rev. Lett. **102**, 181802 (2009).

[7] G. Mention et al., Phys. Rev. **D83**, 073006 (2011).

[8] P. Anselmann et al. [GALLEX Collab.], Phys. Lett. **B342**, 440 (1995); W. Hampel et al. [GALLEX Collab.], Phys. Lett. **B420**, 114 (1998)

[9] J.N. Abdurashitov et al. [SAGE Collab.], Phys. Rev. Lett. **77**, 4708 (1996); Phys. Rev. Lett. **C59**, 2246 (1999).

[10] C. Athanassopoulos et al., NUCL. Instum. Methods **A388**, 149 (1997)

[11] C. Mariani, *Review of Reactor Neutrino Oscillation Experiments*, Modern Physics Letters A **Vol.27**, No. 8 (2012).

[12] Th.A. Mueller, D. Lhuillier et al., arXiv:1101.2663; Th.A. Mueller, PhD Thesis, Paris-Sud XI University, (2010).

[13] C. Giunti, M. Laveder, *Statistical significance of the gallium anomaly*, Phy. Rev. **C83**, 065504 (2011).

[14] S. Gariazzo et al., *Updated Global 3+1 Analysis of Short-BaseLine Neutrino Oscillations*, arXiv:1703.00860 (2017).

[15] G. Tzanankos et al. [MINOS Collab.], *A Proposal to FNAL to run MINOS with the medium energy NuMI beam*, FERMILAB-PROPOSAL-1016 (2011).

[16] R. Abbasi et al. [IceCube Collab.], *Calibration and Characterization of the IceCube Photomultiplier Tube*, Nucl. Instr. Meth. **A618**, arXiv:1002.2442 (2010).

[17] P. Adamson et al. [MINOS Collab.], *A search for sterile neutrinos mixing with muon neutrinos in MINOS*, Phys. Rev. Lett. **117**, 151803 (2016).

[18] S. Razzaque, A.Y. Smirnov, *Searches for sterile neutrinos with IceCube DeepCore*, Phys. Rev. **D85**, 093010 (2012).

[19] F. An et al., *Neutrino Physics with JUNO*, J. Phys. **G43**, 030401 (2016).

[20] K. Abe et al., *Physics potential of a long-baseline neutrino oscillation experiment using a J-PARC neutrino beam and Hyper-Kamiokande*, PTEP 2015, 053C02 (2015).

[21] B. Abi et al., R. Acciarri et al., *Long-Baseline Neutrino Facility (LBNF) and Deep Underground Neutrino Experiment (DUNE), Volume 2: The Physics Program for DUNE at LBNF*, arXiv:1512.06148 (2016).

[22] CERN Neutrino Platform, http://cenf.web.cern.ch/

[23] M. Bass, *The Short Baseline Neutrino Oscillation Program at Fermilab*, arXiv:1702.00990 (2017).

[24] R. Acciarri et al. [SBND Collab., MicroBooNE Collab. and ICARUS/WA104 Collab.], *A Proposal for a Three Detector Short-Baseline Neutrino Oscillation Program in the Fermilab Booster Neutrino Beam*, arXiv:1503.01520 (2015).

[25] R. Acciarri et al. [MicroBooNE Collab.], *Design and Construction of the MicroBooNE Detector*, arXiv:1612.05824 (2017).

[26] C. Rubbia, *Searching for short baseline anomalies with the LAr-TPC detector at shallow depths*, arXiv:1408.6431 (2014).

[27] S. Amerio et al. [ICARUS Collab.], *Design, construction and tests of the ICARUS T600 detector*, Nucl. Instr. Meth. **A527**, 329–410 (2004).

[28] A. Ankowski et al., *Characterization of ETL 9357FLA photomultiplier tubes for cryogenic temperature applications*, Nucl. Instr. Meth. **A556**, 146 – 157 (2006).

[29] S. Kubota et al., *Recombination luminescence in liquid argon and in liquid xenon*, Phys. Rev. **B17**, 2762 (1978).

[30] W.R. Leo, *Techniques for Nuclear and Particle Physics experiments*, Springer-Verlag Berlin Heidelberg (1987).

[31] T. Doke et al., *Estimation of absolute photon yields in liquid argon and xenon for relativistic (1 MeV) electrons*, Nucl. Instr. and Meth. **A291**, 617 (1990).

[32] S. Kubota et al., *Dynamical behavior of free electrons in the recombination process in liquid argon, krypton, and xenon*, Phys. Rev. **B20**, 3486 (1979).

[33] C. Rubbia [ICARUS Collab.], *Using the beam bunch-structure with the T600 detector*, internal SBN report (2014).

[34] A. Falcone, *Studies and tests for the new light collection system of the ICARUS T600 detector*, PhD Thesis, University of Pavia (2016).

[35] A. Falcone et al., *Comparison between large area photo-multiplier tubes at cryogenic temperature for neutrino and rare event physics experiments*, Nucl. Instr. and Meth. **A787**, 55-58 (2015).

[36] G.L. Raselli et al., *Test and characterization of 20 pre-series Hamamatsu R5916-MOD photomultiplier tubes for the ICARUS T600 detector*, IEEE/MIC conference (2016).

[37] H.O. Meyer, *Dark Rate of a Photomultiplier at Cryogenic Temperature*, arXiv:0805.0771v1.

[38] X. Berlman, *Handbook of Fluorescence Spectra of Aromatic Molecules*, Academic Press, New York (1965).

[39] P. Benetti et al., *Detection of the VUV liquid argon scintillation light by means of glass-window photomultiplier tubes*, Nucl. Instr. and Meth. in Physics Research **A505**, 89–92 (2003).

[40] R.B. Darling, EE-527: *Micro Fabrication Photolithography*, pp 1-31.

[41] https://www.comsol.com/comsol-multiphysics

[42] W.M. Burton, B.A. Powell, *Fluorescence of Tetraphenyl-Butadiene in the Vacuum Ultraviolet*, APPLIED OPTICS Vol. 12, No. 1 (1973).

[43] P. Agnes, Master's degree thesis, University of Pavia (2012).

[44] McPHERSON Model 632 Vacuum Ultraviolet Deuterium Light Source.
http://mcphersoninc.com/lightsources/model632.html

[45] McPHERSON Model 234302 Aberration Corrected Vacuum Monochromator.
https://mcphersoninc.com/spectrometers/vuvuvvis/model234302.html

[46] McPHERSON Model 789A-3 Stepper Drive Scan Controller.
http://people.physics.anu.edu.au/ jnh112/mcpherson/spectrometers /model789a3.htm

[47] ICARUS Collaboration, private communication.

LIST OF PUBLICATIONS

R. Acciarri *et al.*, **A Proposal for a Three Detector Short-Baseline Neutrino Oscillation Program in the Fermilab Booster Neutrino Beam**, arXiv:1503.01520 (2015).

A. Falcone *et al.*, **Comparison between large area PMTs at cryogenic temperature for neutrino and rare event physics experiments**, Nuclear Inst. and Methods in Physics Research, Section A, Volume 787, p. 55-58 (2015).

A. Falcone *et al.*, **VUV and UV scintillation light detection by means of SiPM at cryogenic temperature**, Nuclear Inst. and Methods in Physics Research, Section A, Volume 787, p. 1-398 (2015).

G. Raselli *et al.*,**Test and characterization of 20 pre-series hamamatsu R5916-MOD photomultiplier tubes for the ICARUS T600 detector**, Nuclear Science Symposium, Medical Imaging Conference and Room-Temperature Semiconductor Detector Workshop (2016).

A. Falcone *et al.*, **Performance of large area PMTs at cryogenic temperatures for neutrino and rare event physics experiments**, PoS PhotoDet2015 019 (2016).

M. Antonello *et al.*, **Muon momentum measurement in ICARUS-T600 LAr-TPC via multiple scattering in few-GeV range**, *JINST* 12 P04010 (2017).

M. Spanu *on behalf of ICARUS/WA104 collaborations*, **TPB thickness and Quantum Efficiency measurements for the new ICARUS T600 light detection system in the SBN program**, J.Phys.Conf.Ser. 888 no.1, 012092 (2017).

B.Abi *et al.*, **The Single-Phase ProtoDUNE Technical Design Report**, arXiv:1706.07081 (2017).

M. Bonesini *et al.*, **Realization of a high vacuum evaporation system for wave-length shifter deposition on photo-detector windows**, Journal of Vacuum Science & Technology B, Nanotechnology and Microelectronics: Materials, Processing, Measurement, and Phenomena 36, 01A101 (2018).

M. Spanu *et al.*, **Study on TPB as wavelength shifter for the new ICARUS T600 light collection system in the SBN program**, J.Phys.Conf.Ser. (2018).

RINGRAZIAMENTI

Dopo avervi annoiato con la mia tesi, vorrei aggiungere ancora qualche riga per ringraziare le persone che mi hanno accompagnato in questi tre anni.
Un primo ringraziamento va ai miei tutor di dottorato, Gian Luca e Alessandro, per avermi seguito con pazienza in questo percorso.
Un enorme grazie ai miei due referee, Alessandra Tonazzo e Luca Grandi, per le vostre correzioni ed i vostri consigli con i quali ho potuto migliorare il mio lavoro di tesi.
Ringrazio poi le persone con cui ho collaborato al CERN, Claudio, Andrea, Francesco e Will, per avermi aiutato nella mia crescita professionale condividendo con me le loro esperienze e conoscenze.
Ringrazio Filippo e Samuel per i loro insegnamenti sulla meccanica e, non meno importante, per la loro compagnia negli interminabili viaggi dal Cern a Pavia.
Un grazie a Manrico per la sua allegria e per avermi fatto assaggiare la vera cucina romana, sei stato un faro di speranza nelle giornate più nere!
Ringrazio ancora una volta Andrea Rappoldi per la sua minuziosa correzione della mia tesi di dottorato che lo ha, suo malgrado, accompagnato in ogni viaggio di questi ultimi mesi.
Vorrei infine ringraziare il mio fidanzato Daniel, i miei genitori e tutti i miei amici, che ancora una volta sono stati così bravi nel compito più difficile: sostenermi ed incoraggiarmi in questo percorso, non sempre facile da seguire.
E soprattutto, grazie a tutti voi per esservi sorbiti la mia ennesima discussione!
Giuro che questa volta è davvero l'ultima!